

Microfabrication of glass by a short-pulse CO₂ laser with tunable laser parameters

September 2023

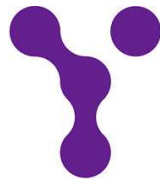
Md. Ekhlashur Rahaman

DOCTORAL THESIS

Microfabrication of glass by a short-pulse
CO₂ laser with tunable laser parameters

A DISSERTATION

Presented to the Integrated Graduate School of Medicine,
Engineering, and Agricultural Sciences,
University of Yamanashi, Japan.



UNIVERSITY
OF
YAMANASHI

September 2023

Md. Ekhlalur Rahaman

Microfabrication of glass by a short-pulse CO₂ laser with tunable laser parameters

By

Md. Ekhlalur Rahaman

Supervised by: **Assoc. Prof. Dr. Kazuyuki Uno**

Acknowledgement

Firstly, I would like to express my deepest gratitude to my advisor, **Assoc. Prof. Dr. Kazuyuki Uno**, who gave me the opportunity to conduct my Ph.D. research in his research group. I owe a heartfelt thanks to Dr. Kazuyuki Uno for his unwavering support of my Ph.D. study and related research, and for his patience, motivation, immense knowledge, and dynamic guidance. His guidance was valuable throughout the course of my research and the writing of this thesis. I also extend my thanks to Prof. Dr. Masanori Hanawa and Prof. Dr. Md. Shamim Ahsan for their valuable support during my Ph.D. journey. Additionally, I am grateful to my lab mates who supported me in various circumstances.

I would also like to extend my thanks to the "MEXT Program" supported by the Ministry of Education, Culture, Sports, Science and Technology, Japan, for providing me the financial support. My thanks also go to the international support center of the University of Yamanashi for their numerous supports during my study in Japan.

I am eternally grateful to my parents, family members, relatives and friends who supported me during challenging times. I also extend my gratitude to all those who supported me directly or indirectly to complete this thesis. I would like to dedicate my Ph.D. thesis to my late grandfather, Doctor Md. Belayet Hossian.

Abstract

Microfabrication of glass such as drilling, piercing, grooving and cutting is required in many industrial applications including optical communication, sensor manufacturing, electronic packaging, micro-lens array, display technology, optoelectronics and etc. In microfabrication of glass, a CO₂ laser has become popular due to numerous benefits such as a simple construction, a cost-effectiveness, and an efficient absorption of glass. CO₂ laser processing of glass is a thermal process because a commercial CO₂ laser has a pulse width of about ten nanoseconds at the shortest. The thermal process gives a thermal damage such as cracks, HAZ (Heat affected zone) and debris. In CO₂ laser processing of glass, laser parameters such as a laser pulse waveform, a beam profile and a repetition rate and sample properties such as a thermal expansion coefficient (CTE) and a melting point (MP) are important. In a commercial glass, a CTE is 5.5×10^{-7} /K to 94×10^{-7} /K and a high CTE may be attributed to produce cracks. An MP is 724°C to 1600°C and a low MP may be attributed to produce HAZ. Therefore, to eliminate cracks and HAZ, a selectable laser parameter or an extra treatment such as pre-heating, liquid assistance or gas assistance is required. This thesis presents microfabrication of glass, that is a hole drilling, in a crown glass with a high CTE of 94×10^{-7} /K and a low MP of 724°C by a short-pulse CO₂ laser with tunable laser parameters. Crack-free holes without an extra treatment in a short-pulse CO₂ laser with a pulse tail were realized and the dependence of drilling characteristics were investigated.

Firstly, to investigate the required laser parameters that will produce crack-free holes in a crown glass without an extra treatment and to investigate the influence of a laser pulse waveform, short laser pulses with a spike pulse width of 250 ns, a pulse tail length of 31.4 μs to 135 μs, an energy ratio of a spike pulse to a pulse tail of 1:7.1 to 1:92 and a fluence per single pulse of 6.01 J/cm² to 38.1 J/cm² were irradiated on a sample at a repetition rate of 1 Hz to 400 Hz. The short laser pulses were irradiated by a focusing lens with a focal length of 38.1 mm at a focus offset of 0.00 mm. The Rayleigh length was 116 μm to 146 μm. The short laser pulses produced crack-free holes regardless of the energy of the pulse tail at a repetition rate of 150 Hz to 400 Hz. The short laser pulse irradiation was realized a high drilling efficiency of 1.56 μm/J/cm² by a laser pulse waveform with an energy ratio of a spike pulse to a pulse tail of 1:25, a

fluence per single pulse of 11.9 J/cm^2 , a total irradiation fluence of 937 J/cm^2 and a repetition rate of 200 Hz.

Secondly, a cylindrical hole drilling in the crown glass using a short-pulse CO_2 laser with a flat-top beam was investigated. The short laser pulse consisted of a spike pulse with a pulse width of 276 ns and a pulse tail with a length of $56.9 \mu\text{s}$ at a repetition rate of 200 Hz. The laser beam had a flat-top profile with a beam quality factor M^2 of 13.5. The flat-top beam was focused by a focusing lens with a focal length of 12.7 mm on the glass surface at a focus offset of -0.20 mm to +0.40 mm. The Rayleigh length was $188 \mu\text{m}$. The flat-top beam produced conical holes at the focus offsets of -0.20 mm to 0.00 mm and produced cylindrical holes at the focus offsets of +0.20 mm to +0.40 mm. In the cylindrical holes, the hole depth was $109 \mu\text{m}$ to $434 \mu\text{m}$, the surface hole diameter was $152 \mu\text{m}$ to $366 \mu\text{m}$, and the aspect ratio, defined as the ratio of the hole depth to the surface hole diameter, was 0.30 to 2.89.

Lastly, the drilling characteristics of a crown glass with a high CTE of $94 \times 10^{-7} /\text{K}$ and a low MP of 724°C by a short-pulse CO_2 laser with a central-peak-intensity beam and a flat-top beam were investigated. The CO_2 laser produced a short pulse with a spike pulse width of 276 ns, a pulse tail length of $56.9 \mu\text{s}$, an energy ratio of a spike pulse to a pulse tail of 1:20 and a central-peak-intensity beam or a flat-top beam at a repetition rate of 200 Hz. In the central-peak-intensity beam and the flat-top beam, a beam quality factor M^2 was 7.6 and 13.5, respectively. The laser beam was focused by a focusing lens with a focal length of 12.7 mm on the glass surface at a focus offset of -0.20 mm to +0.20 mm. The central-peak-intensity beam produced a conical hole at the focus offsets of -0.20 mm to -0.10 mm and produced a biconical hole with a wide waist diameter at the focus offsets of 0.00 mm to +0.20 mm. The flat-top beam produced a conical hole at the focus offsets of -0.20 mm to +0.10 mm and produced a cylindrical hole at a focus offset of +0.20 mm.

Therefore, this thesis gives crack-free holes in a glass with a high CTE of $94 \times 10^{-7} /\text{K}$ and a low MP of 724°C by irradiation of a short-pulse CO_2 laser without an extra treatment. A high drilling efficiency and various types of hole shapes such as a conical hole, a cylindrical hole and a biconical hole was reported that will be useful in industrial applications.

Contents

CHAPTER 1	2
INTRODUCTION	2
1.1 <i>Introduction</i>	2
1.2 <i>Problem statement</i>	5
1.3 <i>Research objectives</i>	6
1.3.1 CO ₂ laser parameters for crack-free holes in crown glass	6
1.3.2 Cylindrical hole drilling in glass by a short-pulse CO ₂ laser with a flat-top beam	7
1.3.3 Comparison of glass drilling characteristics in a short-pulse CO ₂ laser with two different beam profiles.....	8
1.4 <i>Organization of the thesis</i>	8
CHAPTER 2	11
CO₂ LASER MICROFABRICATION OF GLASS	11
2.1 <i>Introduction</i>	11
2.2 <i>CO₂ laser drilling of glass</i>	18
2.2.1 Heat generation and propagation	18
2.2.2 Processing mechanism.....	23
2.2.3 Importance of laser pulse shape in processing.....	26
2.2.4 Importance of laser beam profile in processing	30
2.2.5 Laser beam polarization.....	41
2.2.6 Crack and HAZ formation mechanisms.....	43
2.2.7 Thermal expansion coefficient and melting point of glass	44
2.2.8 CO ₂ laser drilling of glass with an extra treatment	45
2.2.9 CO ₂ laser drilling of glass without an extra treatment.....	48
2.3 <i>Optimization in CO₂ laser microfabrication of glass</i>	50
CHAPTER 3	61
METHODOLOGY	61
3.1 <i>Introduction</i>	61
3.2 <i>Laser device</i>	61
3.2.1 Longitudinally excited CO ₂ laser	61
3.2.2 High-voltage pulsed-power-supply system.....	62
3.2.3 Gas supply system	63
3.3 <i>Laser parameters</i>	64
3.3.1 Laser pulse waveform.....	64
3.3.2 Laser beam profile	65
3.3.3 Spot diameter, fluence per single pulse and total irradiation fluence.....	66
3.4 <i>Material properties</i>	68

3.5	<i>Result analysis methodologies</i>	68
3.5.1	Crack and crack-free hole	71
3.5.2	Shape of hole	71
3.5.3	Surface hole diameter and ratio of surface hole diameter to irradiation diameter	72
3.5.4	Surface HAZ diameter and ratio of surface HAZ diameter to irradiation diameter	72
3.5.5	Hole depth and hole volume	73
3.5.6	Drilling efficiency	73
3.5.7	Taper angle	73
3.5.8	Aspect ratio	74
3.5.9	Waist diameter and ratio of waist diameter to surface hole diameter	74
3.5.10	Waist depth and ratio of waist depth to hole depth	75
CHAPTER 4		77
RESULT AND DISCUSSIONS		77
4.1	<i>CO₂ laser parameters for crack-free holes in crown glass</i>	77
4.1.1	Introduction	77
4.1.2	Experimental set-up	77
4.1.3	Results and discussions	79
4.1.3.1	Investigation of crack-free hole drilling condition	79
4.1.3.1.1	Drilling with laser pulses at a repetition rate of 1 Hz	80
4.1.3.1.2	Drilling with laser pulses at a repetition rate of 50 Hz	80
4.1.3.1.3	Drilling with laser pulses at a repetition rate of 100 Hz	81
4.1.3.1.4	Drilling with laser pulses at a repetition rate of 150 Hz	82
4.1.3.1.5	Drilling with laser pulses at a repetition rate of 200 Hz	83
4.1.3.1.6	Drilling with laser pulses at a repetition rate of 400 Hz	84
4.1.3.1.7	Summary of crack and crack-free condition	85
4.1.3.2	Investigation of the dependence of drilling characteristics on laser parameters	87
4.1.3.2.1	Hole depth, hole volume and drilling efficiency	87
4.1.3.2.2	Surface hole diameter and ratio of a surface hole diameter to an irradiation diameter	90
4.1.3.2.3	Surface HAZ diameter and ratio of a surface HAZ diameter to an irradiation diameter	93
4.1.4	Summary	96
4.2	<i>Cylindrical hole drilling in crown glass by a short-pulse CO₂ laser with a flat-top beam</i>	97
4.2.1	Introduction	97
4.2.2	Experimental set-up	97
4.2.3	Results and discussions	99
4.2.3.1	Investigation of cylindrical hole drilling	99
4.2.3.2	Investigation of the dependence of drilling characteristics on irradiation parameters	100
4.2.3.2.1	Hole depth and hole volume	100
4.2.3.2.2	Surface hole diameter and ratio of surface hole diameter to irradiation diameter	103
4.2.3.2.3	Taper angle	104
4.2.3.2.4	Aspect ratio and surface hole diameter relation with hole depth in cylindrical hole	105
4.2.3.2.5	Surface HAZ diameter and ratio of surface HAZ diameter to irradiation diameter	106

4.2.4 Summary.....	107
4.3 Comparison of a crown glass drilling characteristics in a short-pulse CO₂ laser with two different beam profiles.....	109
4.3.1 Introduction.....	109
4.3.2 Experimental set-up.....	109
4.3.3 Results and discussions.....	111
4.3.3.1 Investigation of a hole shape.....	111
4.3.3.2 Comparison of the dependence of drilling characteristics.....	113
4.3.3.2.1 Hole depth and hole volume.....	113
4.3.3.2.2 Surface hole diameter and ratio of surface hole diameter to irradiation diameter	116
4.3.3.2.3 Ratio of a waist diameter to surface hole diameter and ratio of a waist depth to hole depth in biconical hole.....	118
4.3.3.2.4 Surface HAZ diameter and ratio of surface HAZ diameter to irradiation diameter	120
4.3.4 Summary.....	122
CHAPTER 5.....	124
CONCLUSION	124
<i>5.1 Conclusion</i>	<i>124</i>
<i>List of publications:.....</i>	<i>129</i>
<i>List of Abbreviations:.....</i>	<i>130</i>
REFERENCES	131

List of figures:

Fig. 1.4-1 Flow chart of the thesis.9

Fig. 2.1-1 Various methods of glass drilling. 11

Fig. 2.1-2 Absorption coefficient of a fused silica glass [61,62]..... 13

Fig. 2.1-3 Transmission rate of various glasses such as a fused silica glass, a borosilicate glass, a soda lime glass with the thickness of 2 mm [63]. 13

Fig. 2.1-4 Various drilling methods. (a) Single-pulse drilling. (b) Percussion drilling. (c) Trepanning drilling. (d) Helical drilling. 14

Fig. 2.2-1 Schematic model of heat generation and propagation in laser processing. 18

Fig. 2.2-2 Heat transfer model in a glass by a laser irradiation. 19

Fig. 2.2-3 Schematic of temperature at 1.0 mm from the irradiation spot.20

Fig. 2.2-4 Temperature distribution from the center of laser irradiation to the x-direction in glass. The calculation is based on the Fig. 2.2.3. (a) Fused silica glass with a thermal conductivity of 1.38 W/mK, a density of 2201 kg/m³ and a heat capacity of 1273 J/kgK. (b) Crown glass with a thermal conductivity of 1.38 W/mK, a density of 2560 kg/m³ and a heat capacity of 800 J/kgK. The MATLAB code for the calculation is presented in APPENDIX 2.I.21

Fig. 2.2-5 Time-dependent temperature changes during the pulse operation time into z direction in a fused silica glass at a pulse width of 4.0 ms, a fluence per single pulse of 108 J/cm² and a repetition rate of 50 Hz [94].22

Fig. 2.2-6 Process map in terms of laser power density as a function of interaction time for different examples of laser material processing [86,96,97].23

Fig. 2.2-7 Various process and phase change in the glass during the CO₂ laser irradiation.24

Fig. 2.2-8 Approximate timescales of various process involved in a nanosecond (for example 100 ns) laser irradiation [98].25

Fig. 2.2-9 Schematic of various pulse shapes in a CO₂ laser. (a) Short pulse without a pulse tail. (b) Short pulse with a spike pulse and a pulse tail. (c) Long pulse.26

Fig. 2.2-10 Example of short pulses without a pulse tail in a pulsed CO₂ laser. (a) Short pulse with a pulse width of 45 ns by a TEA CO₂ laser [107]. (b) Short pulse with a pulse width of 170 ns by a TEA CO₂ laser [70]. (c) Short pulse with a pulse width of 110 ns by a longitudinally excited CO₂ laser [29].27

Fig. 2.2-11 Examples of short pulses with a pulse tail in a pulsed CO₂ laser. (a) Short pulse with a spike pulse width of 50 ns and a pulse tail length of about 5.0 μs by a TEA

CO₂ laser [104]. (b) Short pulse with a spike pulse width of 120 ns and a pulse tail length of about 200 μs by a longitudinally CO₂ laser [108]. (c) Overall and (d) magnified time scale waveform of the short pulse with a spike pulse width of 200 ns and a pulse tail length of about 60 μs by a longitudinally excited CO₂ laser [26].....28

Fig. 2.2-12 Examples of long pulses in a pulsed CO₂ laser. (a) Long pulse with a pulse width of 20 μs by a TE CO₂ laser using a special spiker-sustainer circuit [113]. (b) Long pulse with a pulse width of 40 μs by a longitudinally excited CO₂ laser [26]. (c) Long pulse with a pulse width of 250 μs to 1000 μs by a longitudinally excited CO₂ laser using multiple discharge circuits [112].29

Fig. 2.2-13 Schematic of various laser beam profiles. (a) Gaussian beam. (b) Doughnut beam. (c) Flat-top beam.30

Fig. 2.2-14 Schematic of a laser beam focusing.31

Fig. 2.2-15 Beam propagation along the z-axis.31

Fig. 2.2-16 Relation of the spot diameter with the f/D and the M².32

Fig. 2.2-17 Schematic of a gaussian beam profile at the focusing lens entrance and at the focal plane.33

Fig. 2.2-18 Schematic of a doughnut beam profile at the focusing lens entrance and at the focal plane.34

Fig. 2.2-19 Schematic of a flat-top beam profile at the focusing lens entrance and at the focal plane.35

Fig. 2.2-20 Comparison of the various laser beams before focusing. Blue, orange and yellow colors represent a gaussian laser beam, a doughnut laser beam and a flat-top laser beam respectively. (a) Laser beam profiles with a diameter of 22 mm before focusing by a focusing lens with a focal length of 38.1 mm with normalized peak intensity of 1. (b) Peak intensities in various laser beam profiles, maximum value of a gaussian laser beam is normalized as 1. The MATLAB code for beam plotting is presented in APPENDIX 2.II.36

Fig. 2.2-21 Comparison of the various laser beams after focusing. Blue, orange and yellow colors represent a gaussian laser beam, a doughnut laser beam and a flat-top laser beam respectively. (a) Laser beam profiles with different M² at the focal plane of the lens with peak intensity normalized with the peak intensity of the gaussian laser beam profile. (b) Laser beam profiles with different M² at the focal plane of the lens with normalized peak intensity of 1. (c) Laser beam profiles with the same M² of 5.0 at the focal plane of

the lens with normalized peak intensity of 1. The MATLAB code for beam plotting is presented in APPENDIX 2.III.	37
Fig. 2.2-22 Schematic of an airy beam profile at the focusing lens entrance and a flat-top beam profile at the focal plane.....	38
Fig. 2.2-23 Schematic of a flat-top beam at the focusing lens entrance and generation of a flat-top beam profile at the out-of-focus.....	39
Fig. 2.2-24 Various damages in laser drilling of glass.	43
Fig. 2.2-25 CO ₂ laser drilling of a borosilicate glass (Schott D263Teco) with a pre-heating treatment [33].....	45
Fig. 2.2-26 CO ₂ laser drilling of a borosilicate glass (Pyrex 7740) with a during-heating treatment [135].....	46
Fig. 2.2-27 CO ₂ laser drilling of a borosilicate glass (Pyrex 7740) with an underwater treatment [35].....	47
Fig. 2.2-28 Schematic set-up of CO ₂ laser drilling of glass without an extra treatment [6].	48
Fig. 2.2-29 CO ₂ laser drilling of various glasses without an extra treatment [6]. The processing method was single-pulse drilling. The pulse width was 1000 μs and an irradiation diameter was 130 μm. (a) Fused silica glass. (b) Borosilicate (Pyrex 7740) glass. (c) Soda lime glass.....	48
Fig. 3.2-1 Schematic set-up of the longitudinally excited CO ₂ laser.....	62
Fig. 3.2-2 Photograph of the longitudinally excited CO ₂ laser with various components.	62
Fig. 3.2-3 Block diagram of the high-voltage pulsed-power-supply system.....	63
Fig. 3.3-1 Example of a laser pulse waveform. (a) Overall waveform. (b) Magnified timescale of spike pulse.	64
Fig. 3.3-2 Laser pulse waveforms by adjusting a gas medium. Green, red and blue lines represent the laser pulse waveform at an optical cavity length of 125 cm, a gas pressure of 2.0 kPa, 2.4 kPa and 2.6 kPa in a 1:1:2 mixture of CO ₂ /N ₂ /He and a repetition rate of 200 Hz. (a) Overall waveform. (b) Magnified timescale of spike pulse.	64
Fig. 3.3-3 Schematic diagram of a knife-edge method.....	65
Fig. 3.3-4 Example of a laser beam profile measured by a knife-edge method. The gas pressure was 3.2 kPa in a 1:2 mixture of CO ₂ /N ₂ and a repetition rate was 200 Hz. (a) Central-peak-intensity beam with a beam quality factor M ² of 7.0 at an optical cavity	

length of 150 cm. (b) Flat-top beam with a beam quality factor M^2 of 13.5 at an optical cavity length of 60 cm.	66
Fig. 3.3-5 Example of a spot diameter and a fluence per single pulse at the various focus offsets of a focusing lens with a focal length of 12.7 mm. 0.00 mm is the focal plane. A negative offset is the in-focus position, and a positive offset is the out-focus position. The gas pressure was 3.2 kPa in a 1:2 mixture of CO_2/N_2 and a repetition rate was 200 Hz. Red color symbol represents a central-peak-intensity beam with a beam quality factor M^2 of 7.0 at an optical cavity length of 150 cm. Black color symbol represents a flat-top beam with a beam quality factor M^2 of 13.5 at an optical cavity length of 60 cm. (a) Spot diameter. (b) Fluence per single pulse.	67
Fig. 3.3-6 Schematic of a percussion drilling method.	68
Fig. 3.5-1 Considered system parameters, process parameters and material properties. .	69
Fig. 3.5-2 Sample hole images. (a) Hole with crack. (b) Crack-free hole.	71
Fig. 3.5-3 Sample hole shape images. (a) Conical hole. (b) Cylindrical hole. (c) Biconical hole.	71
Fig. 3.5-4 Image of a surface hole diameter.	72
Fig. 3.5-5 Image of a surface HAZ diameter.	72
Fig. 3.5-6 Image of a conical hole depth.	73
Fig. 3.5-7 Image of a taper angle in a conical hole.	74
Fig. 3.5-8 Image of a surface hole diameter and hole depth in a cylindrical hole.	74
Fig. 3.5-9 Image of a waist diameter and a surface hole diameter.	75
Fig. 3.5-10 Image of a waist depth and a hole depth in a biconical hole.	75
Fig. 4.1-1 Schematic set-up of a laser processing system using a longitudinally excited CO_2 laser.	78
Fig. 4.1-2 Examples of laser pulse waveforms at a repetition rate of 200 Hz. Laser intensity was normalized to the maximum value of the spike pulse. Black, red, and blue lines represent laser pulse waveforms with energy ratios of 1:10, 1:25, and 1:45 respectively. (a) Overall waveform. (b) Magnified timescale of spike pulse.	78
Fig. 4.1-3 Laser beam profiles. (a) Doughnut-like beam. (b) Central-peak-intensity with large shoulders beam.	79
Fig. 4.1-4 Image of a glass surface with cracks after irradiation of 50 laser pulses with an energy ratio of 1:25 and a fluence per single of 13.9 J/cm^2 at a repetition rate of 1 Hz. .	80
Fig. 4.1-5 Image of a glass surface with cracks after irradiation of 50 laser pulses with an energy ratio of 1:35 and a fluence per single of 14.3 J/cm^2 at a repetition rate of 50 Hz.	81

Fig. 4.1-6 Image of a glass surface with cracks and without cracks at a repetition rate of 100 Hz. (a) Hole with cracks after irradiation of 50 laser pulses with an energy ratio of 1:30 and a fluence per single of 8.81 J/cm ² . (b) Hole without cracks after irradiation of 50 laser pulses with an energy ratio of 1:70 and a fluence per single of 22.1 J/cm ²	82
Fig. 4.1-7 Image of a glass surface without cracks after irradiation of 50 laser pulses with an energy ratio of 1:25 and a fluence per single of 12.0 J/cm ² at a repetition rate of 150 Hz.....	83
Fig. 4.1-8 Image of a glass surface without cracks after irradiation of 50 laser pulses with an energy ratio of 1:18 and a fluence per single of 33.1 J/cm ² at a repetition rate of 200 Hz.....	84
Fig. 4.1-9 Image of a glass surface without cracks after irradiation of 50 laser pulses with an energy ratio of 1:25 and a fluence per single of 16.9 J/cm ² at a repetition rate of 400 Hz.....	85
Fig. 4.1-10 Top and side views of the crown glass sample irradiated by 30 pulses of the CO ₂ laser short pulse with an energy ratio of 1:25, a fluence per single pulse of 34.1 J/cm ² , a total irradiation fluence of 1023 J/cm ² and a repetition rate of 200 Hz. (a) Top view. (b) Side view.....	87
Fig. 4.1-11 Dependence of hole depth and estimated hole volume on laser pulse waveforms, fluence per single pulse and total irradiation fluence at a repetition rate of 200 Hz. (a) Hole depth. (b) Estimated hole volume. Legend is in the Table 4.1-8.....	88
Fig. 4.1-12 Dependence of a surface hole diameter and a ratio of a surface hole diameter to an irradiation diameter on a laser pulse waveform, a fluence per single pulse and a total irradiation fluence at a repetition rate of 200 Hz. (a) Surface hole diameter. (b) Ratio of a surface hole diameter to an irradiation diameter. Legend is in the Table 4.1-10.	91
Fig. 4.1-13 Dependence of a surface HAZ diameter and a ratio of a surface HAZ diameter to an irradiation diameter on a laser pulse waveform, a fluence per single pulse and a total irradiation fluence at a repetition rate of 200 Hz. (a) Surface HAZ diameter. (b) Ratio of a surface HAZ diameter to an irradiation diameter. Legend is in the Table 4.1-13.	94
Fig. 4.2-1 Glass drilling set-up with longitudinally excited CO ₂ laser.....	98
Fig. 4.2-2 Laser pulse waveform. Laser intensity was normalized to the maximum value of the spike pulse. (a) Overall waveform. (b) Magnified timescale of spike pulse.....	98
Fig. 4.2-3 Flat-top beam profile.....	99

Fig. 4.2-4 Dependence of the spot diameter and the fluence per single pulse on the focus offset. (a) Spot diameter. (b) Fluence per single pulse. Circle, square and triangle symbols represent fluences per pulse of 31.0 J/cm², 38.0 J/cm² and 46.8 J/cm² at a focus offset of 0.00 mm.....99

Fig. 4.2-5 Top and side views of a sample glass irradiated by a flat-top beam at the focus offsets of -0.20 mm to +0.40 mm, a number of pulses of 30 and a repetition rate of 200 Hz..... 100

Fig. 4.2-6 Dependence of the hole depth and the hole depth with respective focus offset distance on the focus offset, the fluence per single pulse and the total irradiation fluence. (a) Hole depth. (b) Hole depth with respective focus offset distance. (c) Estimated hole volume. Symbol colors white, green, red, yellow, black, blue and cyan represent focus offsets of -0.20 mm, -0.10 mm, 0.00 mm, +0.10 mm, +0.20 mm, +0.30 mm and +0.40 mm, respectively. Table 4.2-1 presents the legend of Fig. 4.2-6 (a), (b) and (c). 101

Fig. 4.2-7 Dependence of the surface hole diameter and the ratio of the surface hole diameter to the irradiation diameter on the focus offset, the fluence per single pulse and the total irradiation fluence. (a) Surface hole diameter. (b) Ratio of the surface hole diameter to the irradiation diameter. Symbol colors white, green, red, yellow, black, blue and cyan represent focus offsets of -0.20 mm, -0.10 mm, 0.00 mm, +0.10 mm, +0.20 mm, +0.30 mm and +0.40 mm, respectively. Table 4.2-4 presents the legend of Fig. 4.2-7 (a) and (b). 103

Fig. 4.2-8 Dependence of the taper angle on the focus offset, the fluence per single pulse and the total irradiation fluence. Symbol colors white, green, red, yellow, black, blue and cyan represent focus offsets of -0.20 mm, -0.10 mm, 0.00 mm, +0.10 mm, +0.20 mm, +0.30 mm and +0.40 mm, respectively. Table 4.2-5 presents the legend of Fig. 4.2-8. 104

Fig. 4.2-9 Dependence of the aspect ratio of a cylindrical hole on the focus offset, the fluence per single pulse and the total irradiation fluence and the relation between the hole depth and the surface hole diameter in a cylindrical hole. (a) Aspect ratio. (b) Hole depth vs. surface hole diameter of a cylindrical hole. Symbol colors black, blue and cyan represent focus offsets of +0.20 mm, +0.30 mm and +0.40 mm, respectively. Table 4.2-6 presents the legend of Fig. 4.2-9 (a) and (b)..... 105

Fig. 4.2-10 Dependence of the surface HAZ diameter and the ratio of the surface HAZ diameter to the irradiation diameter on the focus offset, the fluence per single pulse and the total irradiation fluence. (a) Surface HAZ diameter. (b) Ratio of surface HAZ diameter to irradiation diameter. Symbol colors white, green, red, yellow, black, blue and

cyan represent focus offsets of -0.20 mm, -0.10 mm, 0.00 mm, +0.10 mm, +0.20 mm, +0.30 mm and +0.40 mm, respectively. Table 4.2-7 presents the legend of Fig. 4.2-10 (a) and (b)..... 107

Fig. 4.3-1 Glass drilling set-up with longitudinally excited CO₂ laser..... 110

Fig. 4.3-2 Laser pulse waveform. The laser intensity was normalized to the maximum value of the spike pulse. (a) Overall waveform. (b) Magnified timescale of spike pulse. 110

Fig. 4.3-3 Laser beam profiles. (a) Central-peak-intensity beam. (b) Flat-top beam. 110

Fig. 4.3-4 Dependence of a spot diameter and a fluence per single pulse on a focus offset. Red and black symbols represent the central-peak-intensity beam and the flat-top beam, respectively. (a) Spot diameter. (b) Fluence per single pulse..... 111

Fig. 4.3-5 Top and side views of a sample glass irradiated by the central-peak-intensity beam and the flat-top beam at focus offsets of -0.20 mm to +0.20 mm, a number of pulses of 30 and a repetition rate of 200 Hz. (a) Top and side views of a sample glass in the central-peak-intensity beam. (b) Top and side views of a sample glass in the Flat-top beam..... 112

Fig. 4.3-6 Dependence of the hole depth and the estimated hole volume on the beam profile, the focus offset, the fluence per single pulse and the total irradiation fluence. (a) and (b) Hole depth in the central-peak-intensity beam and the flat-top beam, respectively. (c) and (d) Estimated hole volume in the central-peak-intensity beam and the flat-top beam, respectively. Symbol colors purple, green, red, yellow and black represent focus offsets of -0.20 mm, -0.10 mm, 0.00 mm, +0.10 mm and +0.20 mm, respectively. Table 4.3-1 presents the legend of Fig. 4.3-6 (a) to (d). 114

Fig. 4.3-7 Dependence of the surface hole diameter and the ratio of the surface hole diameter to the irradiation diameter on the beam profile, the focus offset, the fluence per single pulse and the total irradiation fluence. (a) and (b) Surface hole diameter in the central-peak-intensity beam and the flat-top beam, respectively. (c) and (d) Ratio of the surface hole diameter to the irradiation diameter in the central-peak-intensity beam and the flat-top beam, respectively. Symbol colors purple, green, red, yellow and black represent focus offsets of -0.20 mm, -0.10 mm, 0.00 mm, +0.10 mm and +0.20 mm, respectively. Table 4.3-4 presents the legend of Fig. 4.3-7 (a) to (d)..... 117

Fig. 4.3-8 Dependence of the ratio of a waist diameter to the surface hole diameter and the ratio of the waist depth to the hole depth in a biconical hole. (a) Ratio of the waist diameter to the surface hole diameter. (b) Ratio of the waist depth to the hole depth.

Symbol colors red, yellow and black represent focus offsets of 0.00 mm, +0.10 mm and +0.20 mm, respectively. Table 4.3-5 presents the legend of Fig. 4.3-8 (a) and (b)..... 119

Fig. 4.3-9 Dependence of a ratio of a surface HAZ diameter to an irradiation diameter on a beam profile, a focus offset, a fluence per single pulse and a total irradiation fluence. (a) and (b) Surface HAZ diameter in the central-peak-intensity beam and the flat-top beam, respectively. (c) and (d) Ratio of a surface HAZ diameter to an irradiation diameter in the central-peak-intensity beam and the flat-top beam, respectively. Symbol colors purple, green, red, yellow and black represent focus offsets of -0.20 mm, -0.10 mm, 0.00 mm, +0.10 mm and +0.20 mm, respectively. Table 4.3-6 presents the legend of Fig. 4.3-9 (a) to (d). 120

Fig. 5.1-1 Summary of the key findings. 127

List of tables:

Table 2.1-1 Glass drilling by a mechanical method, a chemical method and a laser-based method. 12

Table 2.1-2 Examples of various glass drilling with various lasers and drilling methods. 16

Table 2.2-1 Various beam profiles.40

Table 2.2-2 Laser beam polarization types.....42

Table 2.2-3 Basic properties of the various glasses.....44

Table 3.4-1 Basic properties of a crown glass [139,140].68

Table 3.5-1 Values of the system parameters, the process parameters and the material properties that were used in the chapter 4. 70

Table 4.1-1 Laser pulses and the surface conditions at a repetition rate of 1 Hz.80

Table 4.1-2 Laser pulses and the surface conditions at a repetition rate of 50 Hz.81

Table 4.1-3 Laser pulses and the surface conditions at a repetition rate of 100 Hz.82

Table 4.1-4 Laser pulses and the surface conditions at a repetition rate of 150 Hz.83

Table 4.1-5 Laser pulses and the surface conditions at a repetition rate of 200 Hz.84

Table 4.1-6 Laser pulses and the surface conditions at a repetition rate of 400 Hz.85

Table 4.1-7 Presence and absence of cracks in the crown glass depending on the CO₂ laser parameters. The number of pulses was 50. The length of the scale bar is 200 μm in all images.86

Table 4.1-8 Dependence of a hole depth and an estimated hole volume per a total irradiation fluence on a laser pulse waveform and a fluence per single pulse at a repetition rate of 200 Hz. The hole depth and the estimated hole volume per the total irradiation fluence are the slopes of Fig. 4.1-11 (a) and (b), respectively.....88

Table 4.1-9 Dependence of a hole depth and an estimated hole volume per a total irradiation fluence of 50 pulses at a repetition rate of 200 Hz, 300 Hz and 400 Hz.90

Table 4.1-10 Legend of Fig. 4.1-12.....92

Table 4.1-11 The ratio of a surface hole diameter to an irradiation diameter at a total irradiation fluence of 500 J/cm².....92

Table 4.1-12 The ratio of a surface hole diameter to an irradiation diameter at a total irradiation fluence of 1000 J/cm².....93

Table 4.1-13 Legend of Fig. 4.1-13.....95

Table 4.1-14 The ratio of a surface HAZ diameter to an irradiation diameter at a total irradiation fluence of 500 J/cm².....95

Table 4.1-15 The ratio of a surface HAZ diameter to an irradiation diameter at a total irradiation fluence of 1000 J/cm ²	96
Table 4.2-1 Legend of Fig. 4.2-6 (a), (b) and (c). The irradiation diameter for circle, square and triangle symbols at each focus offset corresponds to Fig. 4.2-4 (a).	101
Table 4.2-2 Slope of the Fig. 4.2-6 (a).	102
Table 4.2-3 Slope of the Fig. 4.2-6 (c).	102
Table 4.2-4 Legend of Fig. 4.2-7 (a) and (b). The irradiation diameter for circle, square and triangle symbols at the each focus offset corresponds to Fig. 4.2-4 (a).....	104
Table 4.2-5 Legend of Fig. 4.2-8. The irradiation diameter for circle, square and triangle symbols at each focus offset corresponds to Fig. 4.2-4 (a).	105
Table 4.2-6 Legend of Fig. 4.2-9 (a) and (b). The irradiation diameter for circle, square and triangle symbols at each focus offset corresponds to Fig. 4.2-4 (a).	106
Table 4.2-7 Legend of Fig. 4.2-10 (a) and (b). The irradiation diameter for circle, square and triangle symbols at each focus offset corresponds to Fig. 4.2-4 (a).	107
Table 4.3-1 Legend of Fig. 4.3-6 (a) to (d). The irradiation diameter for diamond, pentagon, star, circle, triangle and square symbols at each focus offset corresponds to Fig. 4.3-4 (a).	115
Table 4.3-2 Slopes of Fig. 4.3-6 (a) and (b).	115
Table 4.3-3 Slopes of Fig. 4.3-6 (c) and (d).	116
Table 4.3-4 Legend of Fig. 4.3-7 (a) to (d). The irradiation diameter for diamond, pentagon, star, circle, triangle and square symbols at each focus offset corresponds to Fig. 4.3-4 (a).	118
Table 4.3-5 Legend of Fig. 4.3-8 (a) and (b). The irradiation diameter for diamond, pentagon and star symbols at each focus offset corresponds to Fig. 4.3-4 (a).	119
Table 4.3-6 Legend of Fig. 4.3-9 (a) to (d). The irradiation diameter for cross, pentagon, star, circle, triangle and square symbols at each focus offset corresponds to Fig. 4.3-4 (a).	121

CHAPTER 1

Introduction

CHAPTER 1

Introduction

1.1 Introduction

Glass is a non-crystalline and a transparent solid with an excellent physical and optical properties [1–3]. The demand of microfabrication of glass such as drilling, piercing, grooving and cutting is increasing in a micro-lens array, an electronic packaging, an optical aperture, a fiber grating, a D-shaped fiber, a microfluidic channel, and a micro/nanostructure [4–13]. To form micro/nanostructures in the glass surface, various conventional methods such as diamond drilling and dicing, waterjet drilling, sandblasting and ultrasonic processing have been used for few decades [1,14,15]. But these conventional methods have limitations in quality and processing speed. Recently, laser-based glass processing is improving in terms of simplicity, quality, processing speed and cost-effectiveness [16–21]. The laser radiation also has several unique properties such as a high intensity of an electromagnetic energy flux and a very narrow beam focused upon a small area. However, among various lasers, a CO₂ laser has become popular due to numerous benefits, including a simple construction, a low cost, an easy maintenance and an efficient absorption in glass [6,22–24].

A CO₂ laser emits light at mid-infrared wavelengths of 9.2 μm to 11.4 μm (mainly 9.6 μm and 10.6 μm). The emitting light from a CO₂ laser is a CW (Continuous wave) or pulsed light depending on the construction of the CO₂ laser. In previous experiments of our group [25–29], a longitudinally excited CO₂ laser with a controllable excitation circuit, gas medium or optical cavity produced various laser pulses such as a tail-free short pulse with a pulse width of 99 ns to 281 ns, a short pulse with a spike pulse width of 137 ns to 480 ns and a pulse tail length of 23.5 μs to 150 μs and an energy ratio of a spike pulse to a pulse tail of 1:14 to 1:112 or a long pulse with a pulse width of 25.7 μs to 82.7 μs. The CO₂ laser with a controllable optical cavity produced various beam profiles such as a gaussian beam, a gaussian-like beam, a doughnut beam, a doughnut-like beam, a flat-top beam and a flat-top-like beam [25,28]. Moreover, the short-pulse CO₂ laser operated at a repetition rate of 1 kHz [30]. In a short-pulse CO₂ laser, a spike pulse gives a thermal processing with a small

thermal effect, and a pulse tail gives a thermal processing with a large thermal effect. A long pulse gives a thermal processing and a large thermal effect. Thermal effect in a glass processing produces a thermal damage such as cracks, HAZ (Heat affected zone) and debris. The thermal damage depends on the radiated laser light parameters such as a laser pulse waveform, a beam profile and a repetition rate, and the sample properties such as a thermal expansion coefficient (CTE), a melting point (MP), a thermal diffusivity and a thermal conductivity [31,32]. Among the sample properties, a CTE and an MP of a glass are the considerable parameters. A commercial glass has a CTE of $5.5 \times 10^{-7} /K$ to $94 \times 10^{-7} /K$ and an MP of 724°C to 1600°C. A high CTE may attribute to produce cracks. A low MP may attribute to produce HAZ. In a Pyrex 7740 glass with a CTE of $33 \times 10^{-7} /K$ and an MP of 820°C and a Schott D263Teco glass with a CTE of $72 \times 10^{-7} /K$ and an MP of 736°C, a CW and long-pulse CO₂ laser with an extra treatment such as pre-heating, gas assistance, liquid assistance and PDMS (Polydimethylsiloxane) layer was used to reduce thermal damages [33–35]. The extra treatments make the processing complex and give extra cost. However, in a fused silica glass with a CTE of $5.5 \times 10^{-7} /K$ and an MP of 1600°C, and an alkali-free glass with a CTE of $32 \times 10^{-7} /K$ and an MP of 971°C, a short-pulse CO₂ laser without an extra treatment produced less thermal damage [23,36].

Moreover, common short-pulse CO₂ lasers, had a gaussian-like beam that produced conical holes [1,23,37,38]. In glass processing, cylindrical hole formation has been attracting attention. A cylindrical hole minimizes light scattering in an optical waveguide, reduces fluidic flow resistance in a microfluidic system, and improves the overall systems functionality compared to a conical hole. Currently, to produce a cylindrical hole, a trepanning drilling method and a helical drilling method, which involve moving a laser beam on a sample, are used [20,39,40]. The helical and trepanning drilling methods result in large surface hole diameters, make the processing complex, and have a lower processing speed than the percussion drilling method that does not involve moving a laser beam on a sample. However, industrial applications require an easy processing system for various kinds of glass and want to produce various hole shapes.

In this thesis, drilling characteristics of a crown glass with a high CTE of $94 \times 10^{-7} /K$ and a low MP of 724°C by a short-pulse CO₂ laser with tunable laser parameters were investigated. At first, to find the crack-free drilling conditions without an extra

treatment and to investigate the influence of a laser pulse waveform, short laser pulses with a spike pulse width of 250 ns, a pulse tail length of 31.4 μs to 135 μs and an energy ratio of a spike pulse to a pulse tail of 1:7.1 to 1:92 were irradiated on a sample at a repetition rate of 1 Hz to 400 Hz. The laser beam was a doughnut-like beam with a beam quality factor M^2 of 3.4 to 7.9 at a repetition rate of 1 Hz to 50 Hz. The laser beam was a central-peak-intensity with large-shoulders beam with a beam quality factor M^2 of 3.1 to 6.7 at a repetition rate of more than 50 Hz to 400 Hz. The short laser pulses were irradiated by a focusing lens with a focal length of 38.1 mm at a focus offset of 0.00 mm. The Rayleigh length was 116 μm to 146 μm . The short laser pulses produced crack-free holes regardless of the energy of the pulse tail at a repetition rate of 150 Hz to 400 Hz. The short laser pulse irradiation was realized a high drilling efficiency that is a hole depth per a total irradiation fluence of 1.56 $\mu\text{m}/\text{J}/\text{cm}^2$ by a laser pulse waveform with an energy ratio of a spike pulse to a pulse tail of 1:25, a fluence per single pulse of 11.9 J/cm^2 , a total irradiation fluence of 937 J/cm^2 and a repetition rate of 200 Hz. The drilling characteristics such as the dependence of a crack or crack-free hole, a hole depth, an estimated hole volume, a drilling efficiency, a surface hole diameter, a ratio of a surface hole diameter to an irradiation diameter, a surface HAZ diameter, a ratio of a surface HAZ diameter to an irradiation diameter on a laser pulse waveform, a fluence per single pulse, a total irradiation fluence and a repetition rate were investigated.

Next, a cylindrical hole drilling in the crown glass with a high CTE of 94×10^{-7} /K and a low MP of 724°C using a short-pulse CO₂ laser with a flat-top beam was investigated. The short laser pulse consisted of a spike pulse with a pulse width of 276 ns, a pulse tail with a length of 56.9 μs and an energy ratio of a spike pulse to a pulse tail of 1:20 at a repetition rate of 200 Hz. The laser beam had a flat-top profile with a beam quality factor M^2 of 13.5. The flat-top beam was focused by the focusing lens with a focal length of 12.7 mm on the glass surface at a focus offset of -0.20 mm to +0.40 mm. The Rayleigh length was 188 μm . The flat-top beam produced conical holes at focus offsets of -0.20 mm to 0.00 mm and produced cylindrical holes at focus offsets of +0.20 mm to +0.40 mm. In the cylindrical holes, the hole depth was 109 μm to 434 μm , the surface hole diameter was 152 μm to 366 μm , and the aspect ratio, defined as the ratio of the hole depth to the surface hole diameter, was 0.30 to 2.89. The drilling characteristics such as the dependence of a hole shape, a hole depth, a surface hole

diameter, a ratio of a surface hole diameter to an irradiation diameter, a surface HAZ diameter, a ratio of a surface HAZ diameter to an irradiation diameter and properties of a cylindrical hole on a focus offset, a fluence per single pulse and a total irradiation fluence were investigated.

Later, the drilling characteristics of a crown glass with a high CTE of 94×10^{-7} /K and a low MP of 724°C by a short-pulse CO₂ laser with a central-peak-intensity beam and a flat-top beam were investigated and compared. The CO₂ laser produced a short pulse with a spike pulse width of 276 ns, a pulse tail length of 56.9 μs, an energy ratio of a spike pulse to a pulse tail of 1:20 and a central-peak-intensity beam or a flat-top beam at a repetition rate of 200 Hz. In the central-peak-intensity beam and the flat-top beam, a beam quality factor M^2 was 7.6 and 13.5, respectively. The laser beam was focused by a focusing lens with a focal length of 12.7 mm on the glass surface at a focus offset of -0.20 mm to +0.20 mm. The Rayleigh length was 106 μm and 188 μm at the central-peak-intensity beam and the flat-top beam, respectively. The central-peak-intensity beam produced a conical hole at a focus offset of -0.20 mm to -0.10 mm and produced a biconical hole with a wide waist diameter at a focus offset of 0.00 mm to +0.20 mm. The flat-top beam produced a conical hole at a focus offset of -0.20 mm to +0.10 mm and produced a cylindrical hole at a focus offset of +0.20 mm. The comparison of the drilling characteristics such as the dependence of a hole shape, a hole depth, a surface hole diameter, a ratio of a surface hole diameter to an irradiation diameter, a surface HAZ diameter, a ratio of a surface HAZ diameter to an irradiation diameter and properties of a biconical hole on a beam profile, a focus offset, a fluence per single pulse and a total irradiation fluence were investigated.

1.2 Problem statement

To realize crack-free holes in a glass with a high CTE and a low MP and to improve the glass processing by a CO₂ laser in terms of simplicity and efficiency, extensive research is still ongoing. However, there are the following concerns in CO₂ laser processing of glass.

1. A thermal damage such as cracks and HAZ.
2. An extra treatment such as pre-heating, liquid assistance or gas assistance.
3. A suitable laser pulse waveform.

4. A suitable beam profile.
5. An unknown drilling characteristic in a glass with a high CTE and a low MP.

1.3 Research objectives

This research was conducted to produce cracks-free hole, control a hole shape, increase the drilling efficiency and reduce the HAZ in a crown glass with a high CTE of $94 \times 10^{-7} /\text{K}$ and a low MP of 724°C without an extra treatment such as pre-heating, liquid assistance or gas assistance by a short-pulse CO_2 laser with tunable laser parameters such as a laser pulse waveform, a beam profile, a focus offset, a fluence per single pulse, a total irradiation fluence and a repetition rate. Moreover, the drilling characteristics like the dependence of a hole shape, a hole depth, an estimated hole volume, a drilling efficiency, a taper angle, an aspect ratio, a surface hole diameter, a ratio of a surface hole diameter to an irradiation diameter, a surface HAZ diameter, a ratio of surface HAZ diameter to an irradiation diameter on the tunable laser parameters were investigated. The detail research goals are described in the below sections:

1.3.1 CO_2 laser parameters for crack-free holes in crown glass

Experimental conditions:

1. A sample was a crown glass with a high CTE of $94 \times 10^{-7} /\text{K}$, a low MP of 724°C and a thickness of $1150 \mu\text{m}$.
2. A spike pulse width was 250 ns , a pulse tail length was $31.4 \mu\text{s}$ to $135 \mu\text{s}$ and the energy ratio of a spike pulse to a pulse tail was 1:7.1 to 1:92.
3. A laser beam profile was a doughnut-like beam and a central-peak-intensity with large-shoulder beam.
4. A focusing lens was with a focal length of 38.1 mm .
5. A focus offset was 0.00 mm .
6. A Rayleigh length was $116 \mu\text{m}$ to $146 \mu\text{m}$.
7. A fluence per single pulse was 6.01 J/cm^2 to 38.1 J/cm^2 .
8. A total irradiation fluence was 238 J/cm^2 to 1305 J/cm^2 .
9. A repetition rate was 1 Hz to 400 Hz .

Research objectives:

1. To realize cracks-free hole drilling in a crown glass by a short-pulse CO₂ laser without an extra treatment.
2. To investigate the dependence a hole depth, an estimated hole volume, a drilling efficiency, a surface hole diameter, a ratio of a surface hole diameter to an irradiation diameter, a surface HAZ diameter, a ratio of a surface HAZ diameter to an irradiation diameter on a laser pulse waveform, a fluence per single pulse, a total irradiation fluence and a repetition rate.

1.3.2 Cylindrical hole drilling in glass by a short-pulse CO₂ laser with a flat-top beam

Experimental conditions:

1. A sample was a crown glass with a high CTE of 94×10^{-7} /K, a low MP of 724°C and a thickness of 1150 μm.
2. A spike pulse width was 276 ns, a pulse tail length was 56.9 μs and the energy ratio of a spike pulse to a pulse tail was 1:20.
3. A laser beam profile was a flat-top beam.
4. A focusing lens was with a focal length of 12.7 mm.
5. A focus offset was -0.20 mm to +0.40 mm.
6. A Rayleigh length was 188 μm.
7. A fluence per single pulse was 3.7 J/cm² to 46.8 J/cm².
8. A total irradiation fluence was 110 J/cm² to 4209 J/cm².
9. A repetition rate was 200 Hz.

Research objectives:

1. To produce a cylindrical hole in a crown glass.
2. To investigate the dependence of a hole shape, a hole depth, a taper angle, an aspect ratio, a surface hole diameter, a ratio of a surface hole diameter to an irradiation diameter, a surface HAZ diameter, a ratio of a surface HAZ diameter to an irradiation

diameter on a focus offset, a fluence per single pulse and a total irradiation fluence.

1.3.3 Comparison of glass drilling characteristics in a short-pulse CO₂ laser with two different beam profiles

Experimental conditions:

1. A sample was a crown glass with a high CTE of $94 \times 10^{-7} /K$, a low MP of 724°C and a thickness of 1150 μm .
2. A spike pulse width was 276 ns, a pulse tail length was 56.9 μs and the energy ratio of a spike pulse to a pulse tail was 1:20.
3. A laser beam profile was a central-peak-intensity beam and a flat-top beam.
4. A focusing lens was with a focal length of 12.7 mm.
5. A focus offset was -0.20 mm to +0.20 mm.
6. A Rayleigh length was 106 μm and 188 μm .
7. A fluence per single pulse was 12.8 J/cm² to 47.7 J/cm².
8. A total irradiation fluence was 383 J/cm² to 4296 J/cm².
9. A repetition rate was 200 Hz.

Research objectives:

1. To compare the hole shape with a central-peak-intensity beam and a flat-top beam at various focus offset.
2. To compare the dependence of a hole shape, a hole depth, a surface hole diameter, a ratio of a surface hole diameter to an irradiation diameter, a surface HAZ diameter, a ratio of a surface HAZ diameter to an irradiation diameter and on a beam profile, a focus offset, a fluence per single pulse and a total irradiation fluence.

1.4 Organization of the thesis

The thesis is divided into five chapters as shown in the Fig.1.4-1. This introductory chapter described the problem statement and research objectives in a glass

processing that has a high CTE and a low MP. Chapter 2 will describe various lasers that are used in glass processing, importance of laser parameters in glass processing and recent glass processing by a CO₂ laser. Chapter 3 will describe the construction of the short-pulse CO₂ laser, the laser parameters that were used in the experiments and the result acquisition methods. Chapter 4 will present the obtained results and the relevant discussions and finally Chapter 5 will conclude with the summary of the research.

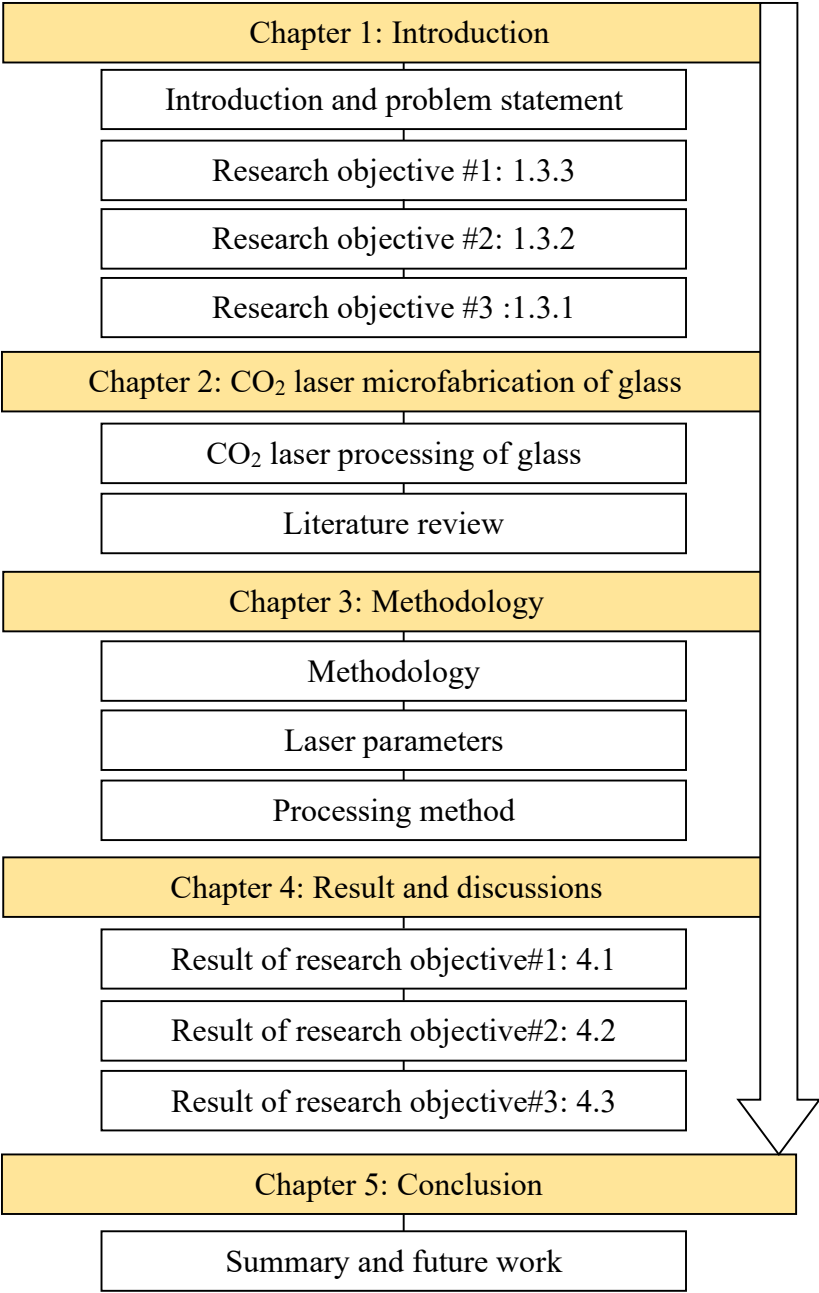


Fig. 1.4-1 Flow chart of the thesis.

CHAPTER 2

CO₂ laser microfabrication of glass

CHAPTER 2

CO₂ laser microfabrication of glass

2.1 Introduction

Microfabrication of glass such as drilling, piercing, grooving and cutting is required in various industrial applications such as manufacturing of optical components, electronic packaging, optical sensors and microfluidic devices [41–45]. Fig. 2.1-1 shows various methods of glass processing. Mechanical methods such as grinding, powder blasting, abrasive jet micromachining and ultrasonic vibration, and chemical methods such as wet etching, deep reactive ion etching and hydrofluoric acid etching are commonly used [43,46–52]. In a mechanical method and a chemical method of glass processing, quality and processing speed are the limitations [1,53–55]. Besides, a laser-based method of glass processing is becoming popular due to numerous advantages such as simplicity, quality, processing speed and cost-effectiveness [21,55–58]. Table 2.1-1 shows the advantages of a laser-based method compared to a mechanical method and a chemical method in glass drilling. The drilling speed of a laser-based method was higher than that of a mechanical method and a chemical method. Moreover, the produced hole diameter was also small in a laser-based method.

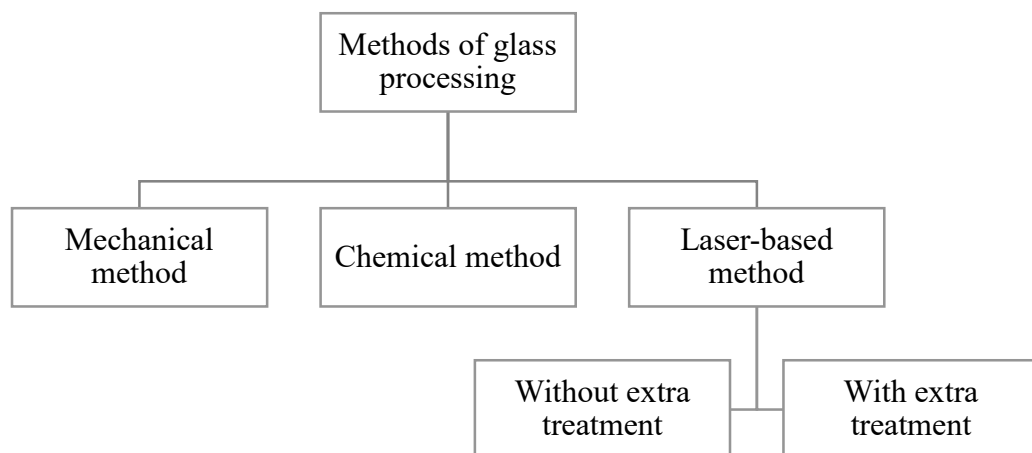
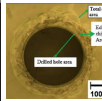
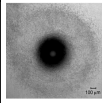
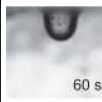
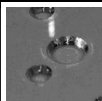
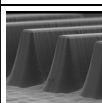
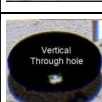
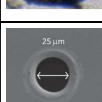
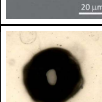
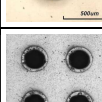
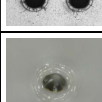


Fig. 2.1-1 Various methods of glass drilling.

Table 2.1-1 Glass drilling by a mechanical method, a chemical method and a laser-based method.

Ref.	Method	Diameter	Hole depth	Speed	Sample image
[49]	Grinding (Mechanical)	1011-1223 μm	4000 μm	5 $\mu\text{m/s}$	
[50]	Abrasive jet (Mechanical)	800 μm	50 μm	32 $\mu\text{m/s}$	N/A
[51]	Abrasive slurry jet (Mechanical)	800 μm	900 μm	1.88 $\mu\text{m/s}$	
[15]	Abrasive slurry jet (Mechanical]	390 μm	350 μm	4.38 $\mu\text{m/s}$	
[46]	Wet etching (Chemical)	3000 μm	1000 μm	0.13 $\mu\text{m/s}$	
[59]	Deep reactive ion etching (Chemical)	200 μm	250 μm	0.035 $\mu\text{m/s}$	
[52]	Deep reactive ion etching (Chemical)	100 μm	300 μm	0.0058 $\mu\text{m/s}$	
[36]	CO ₂ laser	25 μm	100 μm	20000 $\mu\text{m/s}$	
[35]	CO ₂ laser	280 μm	500 μm	11400 $\mu\text{m/s}$	
[33]	CO ₂ laser	71 μm	500 μm	2000 $\mu\text{m/s}$	
[60]	CO ₂ laser	125 μm	1025 μm	5857 $\mu\text{m/s}$	

In laser-based glass drilling, an absorption of a laser wavelength in a glass is important. An absorption or a transmission of a glass depends on a wavelength. Fig. 2.1-2 shows the absorption coefficient in a fused silica glass at a wavelength of 100 nm to 12 μm [61,62]. Moreover, Fig. 2.1-3 shows the transmission spectra of various glasses such as a fused silica glass, a borosilicate glass and a soda lime glass with a

thickness of 2 mm at a wavelength of 100 nm to 12 μm [63]. A CO₂ laser with a wavelength of 10.6 μm has a high absorption in various types of glasses.

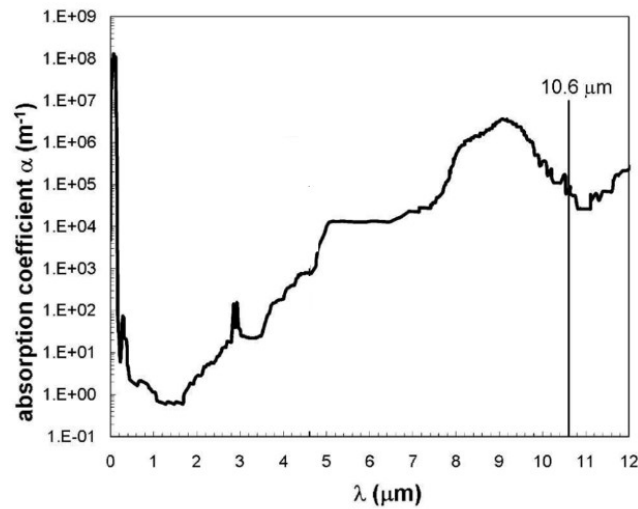


Fig. 2.1-2 Absorption coefficient of a fused silica glass [61,62].

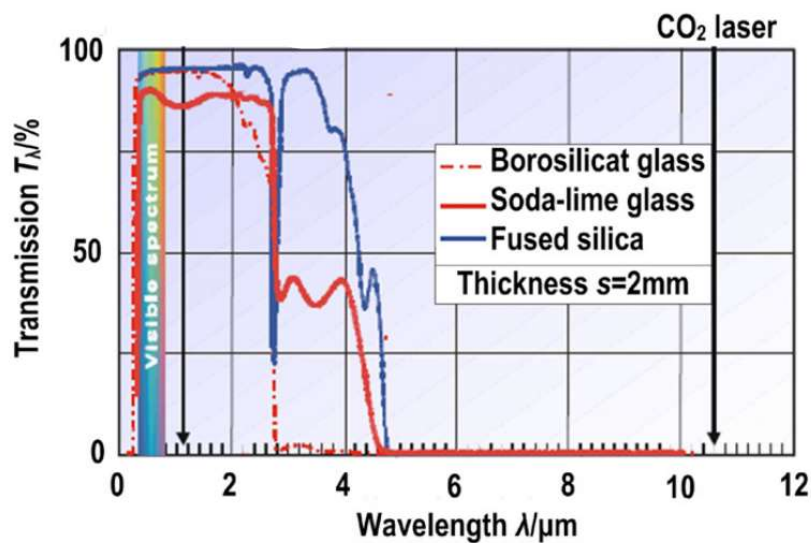


Fig. 2.1-3 Transmission rate of various glasses such as a fused silica glass, a borosilicate glass, a soda lime glass with the thickness of 2 mm [63].

In laser-based drilling, various drilling methods such as single-pulse drilling, percussion drilling, trepanning drilling and helical drilling are the most common methods. Fig. 2.1-4 shows a schematic illustration of the various drilling methods. In a single-pulse drilling method, a pulsed laser irradiates only one pulse on a sample. A single-pulse drilling method requires a high irradiated laser fluence to form a high-

aspect-ratio hole. A single-pulse drilling method does not require the movement of a sample or a focusing system. In a percussion drilling method, a pulsed laser irradiates multiple pulses on the same spot in a sample. A hole depth is controlled by a number of irradiated pulses or a total irradiated laser fluence. In a percussion drilling method, a sample and a focusing systems do not require a movement from an irradiation axis. But the sample might move toward or backward the laser beam irradiation depending on requirement of a hole shape. In a trepanning drilling method, multiple overlapping holes are drilled around the circumference of a targeted hole. A pulsed laser with a high repetition rate or a CW laser is used in a trepanning drilling method. A trepanning drilling method requires rotation of a laser beam axis or a sample. In a helical drilling method, which is a type of trepanning drilling method, the laser beam follows a helical path, rotating with respect to the sample. Furthermore, an area scanning drilling method is more likely to a helical drilling method that is used to produce a rectangular hole or groove. Therefore, a single pulse drilling method and a percussion drilling method do not require the movement of a laser beam that require a simple set-up and make the processing simple. On the other hand, a trepanning drilling method and a helical drilling method require a movement of a laser beam that require a complex set-up and make the processing complex.

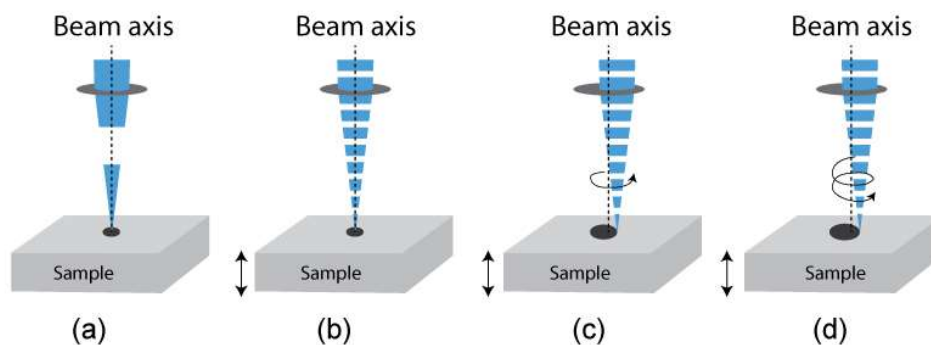


Fig. 2.1-4 Various drilling methods. (a) Single-pulse drilling. (b) Percussion drilling. (c) Trepanning drilling. (d) Helical drilling.

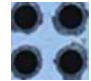
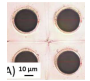
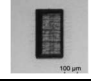
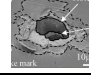
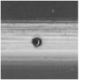
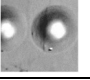
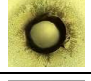
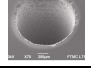
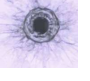
Table 2.1-2 shows examples of various glass drilling with various lasers and drilling methods. Various lasers, especially a UV (Ultraviolet) laser with a wavelength of 100 nm to 400 nm, a visible laser with a wavelength of 400 nm to 700 nm, a near infrared laser with a wavelength of 700 nm to about 3 μm and a CO₂ laser with a wavelength of 9.3 μm and 10.6 μm are typically used in a glass drilling. In a UV laser,



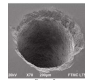
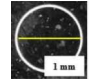
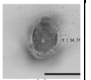
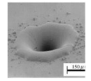
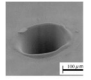
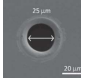
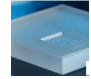
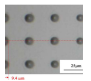
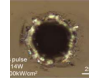
such as an F₂ laser with a wavelength of 157 nm, an ArF laser with a wavelength of 193 nm, a KrF laser with a wavelength of 248 nm and a Nd:YAG FHG (Fourth harmonic generation) laser with a wavelength of 266 nm, and with a pulse width of about 5 ns to 30 ns, the processing mechanism is a photoionization process and a thermal process [64]. A high photon energy gives the photoionization process, and a pulse width of nanosecond gives the thermal process with small thermal effects. Therefore, a smooth processing without debris can realize by a high photon energy of an F₂ laser of 7.8 eV, an ArF laser of 6.4 eV and a KrF laser of 4.9 eV [65,66]. A UV laser can realize sub-microns processing by a small focus spot diameter due to a short wavelength.

An ultrafast laser with a wavelength of 800 nm to 1552 nm and a pulse width of several hundreds of femtoseconds induces multiphoton absorption and gives a non-thermal ablation process [67,68]. A non-thermal process can give a smooth processing. However, an ultrafast laser has a very low pulse energy of about several nanojoules, but the repetition rate is very high and about several hundreds of kilohertz to gigahertz. The accumulated heat cannot be ignored. Therefore, an additional cooling method such as an assist gas has to be used in femtosecond laser processing. The assist gas is useful for removing debris. Additionally, an ultrafast laser realizes processing inside the glass (in volume processing) because a glass is transparent in the wavelength of 800 nm to 1552 nm and the processing takes place by multiphoton absorption near the focus area. An ultrafast laser can realize several microns processing.

On the other hand, a CO₂ laser has a main wavelength of 9.6 μm and 10.6 μm and a pulse width of several tens of nanoseconds to several milliseconds. A CO₂ laser is absorbed at the surface of a glass because the CO₂ laser wavelengths have a high absorption coefficient in a glass. A CO₂ laser can realize several-tens-of-microns processing because of a long wavelength of 9.2 μm to 11.4 μm. A CO₂ laser gives high efficiency processing by a high absorption of 99% in glass and a high efficiency from an electric energy to a laser energy of about 5% to 20% [69–71]. Therefore, in glass processing by a CO₂ laser, the overall efficiency is high. CO₂ laser processing is a thermal process where processing is dominated by melting and vaporization of a locally irradiated glass surface. Various thermal damages such as cracks, HAZ and debris are produced during glass processing depending on the irradiation conditions and the glass properties. Therefore, the sustainable control of the laser parameters is necessary for CO₂ laser processing.

Table 2.1-2 Examples of various glass drilling with various lasers and drilling methods.

Ref. (Year)	Laser (Wavelength)	Pulse width	Fluence /pulse	Rep. Rate	Drilling method	Hole diameter	Ratio of hole diameter to irradiation diameter	Drilling efficiency	Crown glass	Foturan glass	Soda lime glass	Borosilicate (Pyrex 7740) glass	Alkali-free glass	Fused silica glass
[72] (2014)	ArF (193 nm)	25 ns	7 J/cm ²	25 Hz	Percussion	25 μm	N/A	0.02 μm/J/cm ²						
[73] (2007)	Nd:YAG (FHG) (266 nm)	5 ns	10 J/cm ²	10 Hz	Area scanning	(sub-mm size)	N/A	0.50 μm/J/cm ²						
[74] (2020)	Nd:YAG (FHG) (266 nm)	8 ns	N/A	10 kHz	Percussion	30 μm	N/A	N/A						
[75] (2005)	Nd:YAG THG (Third harmonic generation) (355 nm)	30 ns	N/A	1 kHz	Percussion	12 μm	1.71	N/A						
[76] (2004)	Nd:YVO ₄ (355 nm)	20 ns	305 J/cm ²	2.5 kHz	Percussion	10 μm	2.00	N/A						
[77] (2012)	Nd:YAG SHG (Second harmonic generation) (532 nm)	30 ns	N/A	N/A	Percussion	100 μm	N/A	N/A						
[20] (2015)	Nd:YVO ₄ (532 nm)	30 ns	26 J/cm ²	25 kHz	Helical	1000 μm	N/A	N/A						
[78] (2019)	Nd:YAG (SHG) (532 nm)	5 ns	130 J/cm ²	N/A	Percussion	27 μm	6.4	N/A						

Ref. (Year)	Laser (Wavelength)	Pulse width	Fluence /pulse	Rep. Rate	Drilling method	Hole diameter	Ratio of hole diameter to irradiation diameter	Drilling efficiency	Crown glass	Foturan glass	Soda lime glass	Borosilicate (Pyrex 7740) glass	Alkali-free glass	Fused silica glass
[79] (2007)	Ti:sapphire (775 nm)	150 fs	10 J/cm ²	1 kHz	Helical	56 μm	6.22	N/A						
[80] (2014)	Fiber (1030 nm)	750 fs	20 J/cm ²	100 kHz	Trepanning	60 μm	2.40	0.25 μm/J/cm ²						
[20] (2015)	Nd:YVO ₄ (1064 nm)	30 ns	68 J/cm ²	10 kHz	Helical	1000 μm	N/A	N/A						
[81] (2020)	Er-doped fiber (1552 nm)	800 fs	70 J/cm ²	N/A	Helical	1000 μm	166	N/A						
[82] (2017)	Er-doped fiber (1552 nm)	800 fs	Not enough data	100 kHz	Percussion	54 μm	N/A	N/A						
[6] (2003)	CO ₂ (9.3 μm)	1000 μs	3767 J/cm ²	1 Hz	Single-pulse +Percussion	150 μm	1.15	0.14						
[36] (2015)	CO ₂ (9.3 μm)	1 μs	Not enough data	1 Hz	Single-pulse	25 μm	N/A	N/A						
[83] (2015)	CO ₂ (10.6 μm)	380 ns	15 J/cm ²	100 Hz	Area scanning	5000 μm	25.0	N/A						
[23] (2011)	CO ₂ (10.6 μm)	50 ns	9.6 J/cm ²	1 Hz	Percussion	9.4 μm	0.47	0.005 μm/J/cm ²						
[84] (2015)	CO ₂ (10.6 μm)	50 μs	25 J/cm ²	250 Hz	Percussion	45 μm	0.75	N/A						

2.2 CO₂ laser drilling of glass

2.2.1 Heat generation and propagation

A CO₂ laser emits light that is an electromagnetic radiation at the mid-infrared wavelengths of 9.2 μm to 11.4 μm (mainly 9.6 μm and 10.6 μm). In laser processing of materials, various phenomena occur immediately after the laser irradiation until the processing is completed. Fig. 2.2-1 shows a schematic model of the various processes involved in a heat generation and a heat propagation. When a CO₂ laser with a pulse width of about 100 ns is irradiated on a glass surface, the glass absorbs the laser energy at the surface. The absorbed laser intensity can be expressed by the Eq. 2.2-1 [21,85]:

$$I(z) = I_0 \exp(-\alpha z) \quad \text{Eq. 2.2-1}$$

Where, $I(z)$ is the absorbed laser intensity [W/m^2], I_0 is the initial laser intensity [W/m^2], α is the absorption coefficient [m^{-1}], and z is the depth [m] from the irradiated position. The absorbed laser intensity is the highest on the surface and exponentially decays into the material so does the produced heat. In glass, atoms are tightly bonded with the surrounding atoms and keep vibrating at their own equilibrium positions. The absorbed electromagnetic wave gives a lattice vibration which releases energy in a form of a heat energy [86–89]. The generated heat from the absorbed laser can be expressed by the Eq. 2.2-2:

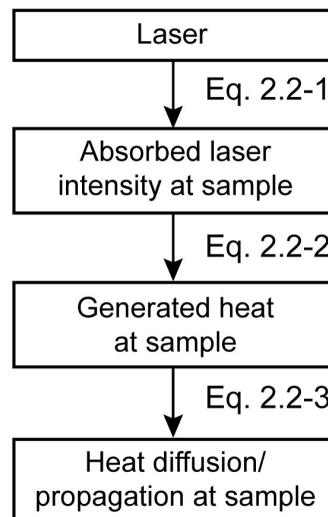


Fig. 2.2-1 Schematic model of heat generation and propagation in laser processing.

$$Q = \beta I$$

$$\text{Eq. 2.2-2}$$

Where, Q is the generated heat intensity [W/m^2], I is the absorbed laser intensity [W/m^2] and β is the energy conversion efficiency. In common energy transfer, the loss energy changes the heat. The energy conversion efficiency β can be 100%, which can affect the produced heat intensity. Therefore, it is important to consider β in a heat propagation although most studies ignored the term to represent the generated heat intensity in a laser irradiation.

The generated heat by laser irradiation on the glass surface transfers in the glass. Fig. 2.2-2 shows the heat propagation schematic in the glass and Eq. 2.2-3 represents the mathematical expression of the heat propagation [89–91].

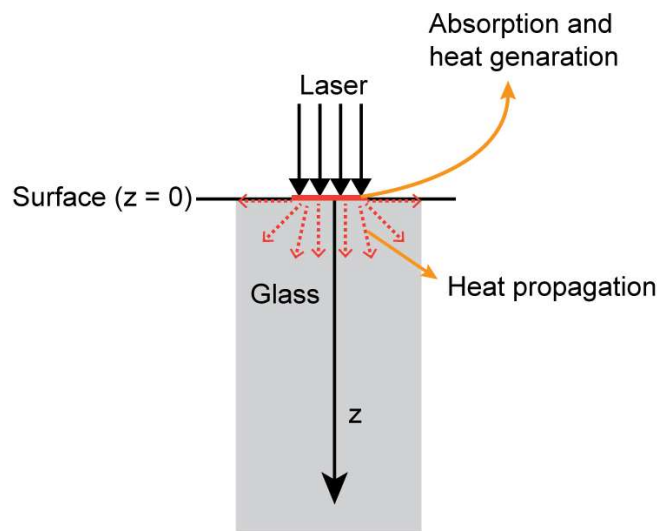


Fig. 2.2-2 Heat transfer model in a glass by a laser irradiation.

$$\rho c_p \frac{\partial T}{\partial t} = Q + \nabla \cdot (K \nabla T)$$

$$\rho c_p \frac{\partial T(x,y,z,t)}{\partial t} = Q(x,y,z,t) + K \left[\frac{\partial^2 T(x,t)}{\partial x^2} + \frac{\partial^2 T(y,t)}{\partial y^2} + \frac{\partial^2 T(z,t)}{\partial z^2} \right] \quad \text{Eq. 2.2-3}$$

Where, ρ is the density [kg/m^3], c_p is the specific heat capacity [J/kgK], K is the thermal conductivity [W/mK], Q is the generated heat density [W/m^3], and T is the temperature [K]. Most studies treated a laser source on the surface as a heat flux and calculated the Eq. 2.2-3 only without considering the Eq. 2.2-2 is shown the conversion of a laser energy to a heat energy [89–91]. In addition to the above, there is actually

heat conversation loss and the calculation of heat and processing shape is very difficult and has not been realized yet.

The solution of the Eq. 2.2-3 gives the temperature at the different distances into the material as the schematic of laser irradiation on a fused silica glass and a crown glass is shown in Fig. 2.2-3. The temperature distributions at different distances from the irradiation spot and at various time after the laser irradiation are shown in Fig. 2.2-4. For an example, a generated heat of 3000 K at $x = 0.0$ mm with a pulse width of 100 ns and an irradiation diameter of 100 μm on a fused silica glass with a thermal conductivity of 1.38 W/mK, a density of 2201 kg/m^3 and a heat capacity of 1273 J/kgK gives a temperature of 293 K at $x = 1.0$ mm and $t = 0.0$ s that is just after completing the irradiation of 100 ns pulse. Later, at $t > 0.0$ s, the assumed maximum temperature of 3000 K at $x = 0.0$ mm will conduct through the glass. Therefore, the maximum temperature at $x = 0.0$ mm will reduce with $t > 0.0$ s as well as conduct into the glass. The calculated temperature at $x = 0.0$ mm and $x = 1.0$ mm is 350 K and 310 K, respectively at $t = 1.0$ s.

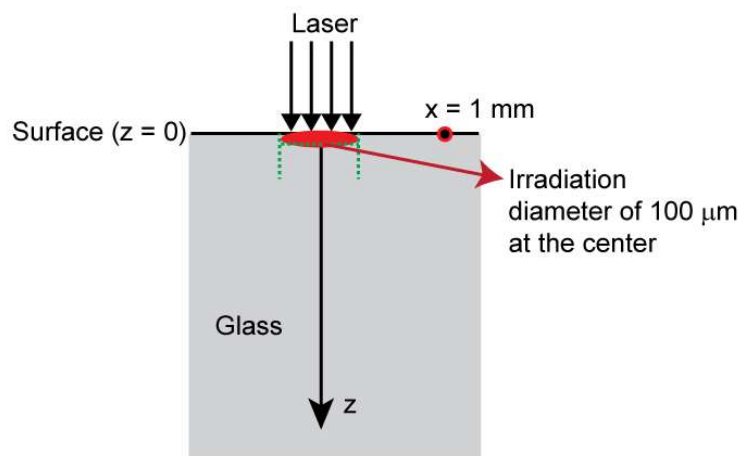
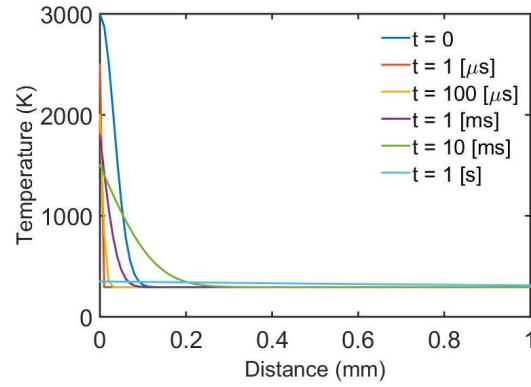
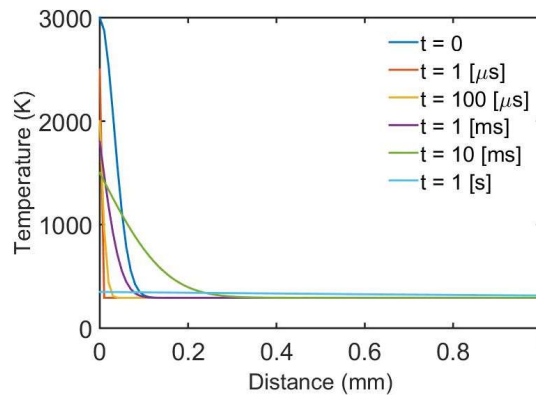


Fig. 2.2-3 Schematic of temperature at 1.0 mm from the irradiation spot.

However, the temperature can be lost due to the propagation into the air and due to the thermal radiation. The heat loss due to the propagation into the air is expressed by Eq. 2.2-4. Where, $Q_{\text{loss}1}$ is the rate of the heat propagation into the air per unit time [W], h is the convective heat transfer coefficient [$\text{W/m}^2\text{K}$], A is the heat transfer area



(a)



(b)

Fig. 2.2-4 Temperature distribution from the center of laser irradiation to the x-direction in glass. The calculation is based on the Fig. 2.2.3. (a) Fused silica glass with a thermal conductivity of 1.38 W/mK, a density of 2201 kg/m³ and a heat capacity of 1273 J/kgK. (b) Crown glass with a thermal conductivity of 1.38 W/mK, a density of 2560 kg/m³ and a heat capacity of 800 J/kgK. The MATLAB code for the calculation is presented in APPENDIX 2.I.

[m²], T is the temperature [K] on the surface and T₀ is the ambient temperature [K]. Therefore, in the case of Fig. 2.2-3, a generated temperature T of 3000 K on the surface of a glass with an ambient temperature T₀ of 293 K and a convective heat transfer coefficient in the air h of 2.5 W/m²K gives a heat propagation into the air per unit time of 5.31×10⁻⁵ W that is 5.31×10⁻⁵ K/s. Hence, the temperature loss due to the propagation into the air is too small and negligible.

$$Q_{\text{loss1}} = hA(T-T_0) \quad \text{Eq. 2.2-4}$$

The heat loss due to the thermal radiation is expressed by Eq. 2.2-5. Where, Q_{loss2} is the rate of the thermal radiation per unit time [W], ε is the emissivity that is 0.89 in glass, σ is the Stefan's constant that is 5.67×10⁻⁸ W/m²K⁴, A is the heat radiating area

$[\text{m}^2]$, T is the temperature $[\text{K}]$ on the surface and T_0 is the ambient temperature $[\text{K}]$. Therefore, in the case of Fig. 2.2-3, a generated temperature T of 3000 K on the surface of a glass with an ambient temperature T_0 of 293 K gives the thermal radiation per unit time of 0.032 W that is 0.032 K/s. Hence, the temperature loss due to the thermal radiation is small and negligible.

$$Q_{\text{loss}2} = \varepsilon\sigma A(T^4 - T_0^4) \quad \text{Eq. 2.2-5}$$

Therefore, Eq. 2.2-3 is important. In my experiments, the irradiated laser intensity is adjustable, and the temperature at 1.0 mm at different time intervals is measurable. Thus, the temperature by a CO_2 laser irradiation is predictable.

Several numerical analyses based on simulation are conducted to analyze a temperature distribution during the laser processing [92–94]. For example, Fig. 2.2-5 shows a numerically investigated time-dependent temperature distribution in a pulsed CO_2 laser irradiation at different distances in a fused silica glass surface at the pulse duration of 4 ms, the fluence per single pulse of 108 J/cm^2 and the repetition rate of 50 Hz [94]. During the laser pulse irradiation, the temperature raised rapidly and dropped

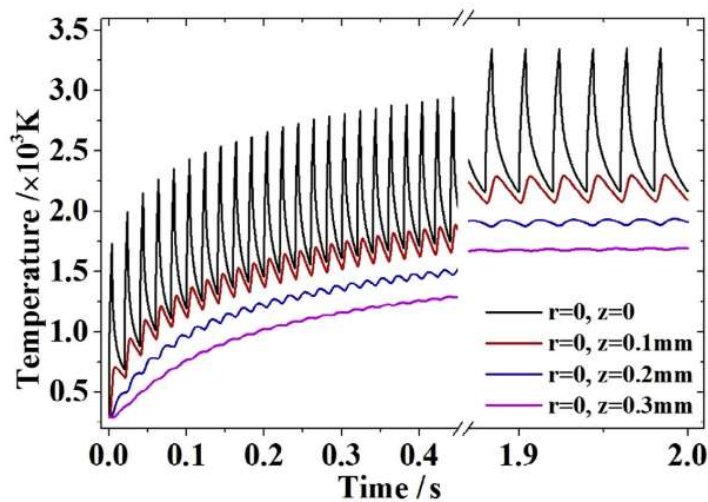


Fig. 2.2-5 Time-dependent temperature changes during the pulse operation time into z direction in a fused silica glass at a pulse width of 4.0 ms, a fluence per single pulse of 108 J/cm^2 and a repetition rate of 50 Hz [94].

rapidly until the next pulse was irradiated. The simulation result showed that the first pulse produced a temperature of about 1750 K at $t = 0.012 \text{ s}$ and the temperature dropped about 750 K at $t = 0.025 \text{ s}$ then the second pulse was irradiated, and the

temperature was raised to about 2000 K at $t = 0.029$ s and the temperature dropped to about 850 K at $t = 0.04$ s. The maximum temperature at the surface was 3354 K at $t = 1.984$ s. When the irradiation was completed that is at $t = 2.0$ s, the temperature at the glass surface will gradually cool down through the natural convection cooling method to the room temperature. During percussion drilling, heat accumulates between the consecutive pulses. In a high repetition rate, the pulse interval time is small, and temperature cannot drop much before the next pulse apply. Therefore, a high repetition rate gives a higher amount of heat accumulation than a low repetition rate.

However, recently, many studies based on machine learning have been conducted to match inputs such as a heat source and an incident power density and output such as processing shape, ignoring modeling and simulation by considering the actual heat produced by the laser energy, the phase change of the processed material during processing and shape change such as a drilling shape [95].

2.2.2 Processing mechanism

Fig. 2.2-6 shows the laser power density regimes as a function of a pulse duration for various processes in laser processing of a material. The processes are mainly categorized into four processes such as a heating without a melting and a vaporization, a melting without a vaporization, a vaporization and a non-thermal process. To initiate

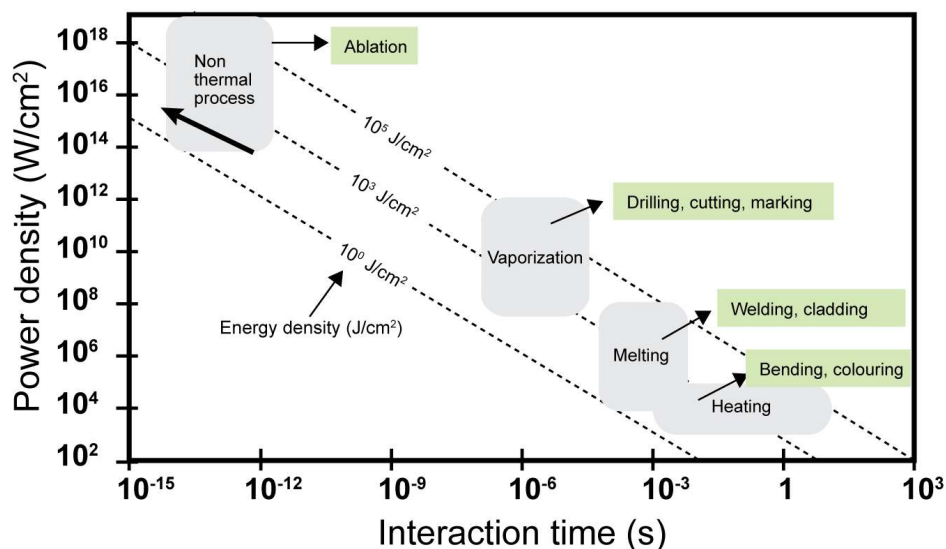


Fig. 2.2-6 Process map in terms of laser power density as a function of interaction time for different examples of laser material processing [86,96,97].

each process a threshold power density is required. A laser power density of below 10^5 W/cm² with a long pulse with an approximate pulse width of 10^1 s to 10^{-3} s gives a surface heating process that is required in bending, coloring and etc. A laser power density of 10^6 W/cm² to 10^7 W/cm² with a long pulse irradiation gives a melting process that is required in welding, cladding and etc. A laser power density of over 10^8 W/cm² with a short pulse with an approximate pulse width of 10^{-6} s to 10^{-8} s gives a vaporization process that is required in drilling, cutting, marking and etc. A laser power density of over 10^{12} W/cm² with an ultrashort pulse with an approximate pulse width of 10^{-12} s to 10^{-15} s gives a non-thermal process that is required in an ablation.

When a laser irradiated on the glass surface, the generated heat by a laser irradiation causes the glass to undergo several phase changes as shown in Fig. 2.2-7. Initially, the solid glass absorbs the laser at the surface, which raises the surface temperature. Once the temperature exceeds the melting point of the glass, a transition from a solid state to a liquid state occurs. The liquid state is a transient phase that occurs during the heating process and facilitates the material removal. As the laser continues to heat the liquid glass, the temperature increases further, causing the liquid

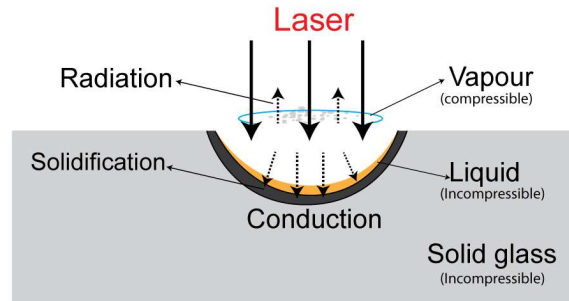


Fig. 2.2-7 Various process and phase change in the glass during the CO₂ laser irradiation.

to vaporize. Once the laser irradiation stops, the remaining molten glass cools down and solidifies, returning to the solid state. The compressibility and incompressibility nature of the various glass states play an important role in laser processing. The laser irradiation causes a rapid and intense local increase in temperature, leading to the vaporization of the material and the formation of a high-pressure plasma. The high pressure creates a shockwave that propagates through the glass. Since the solid glass is incompressible, the shockwave can cause stress and potential damage in the glass. Therefore, laser irradiation gives phase changes such as solid, liquid, gas, plasma in

glass and the shape change of a sample. So, the simulation of laser processing is very difficult and has not been realized yet.

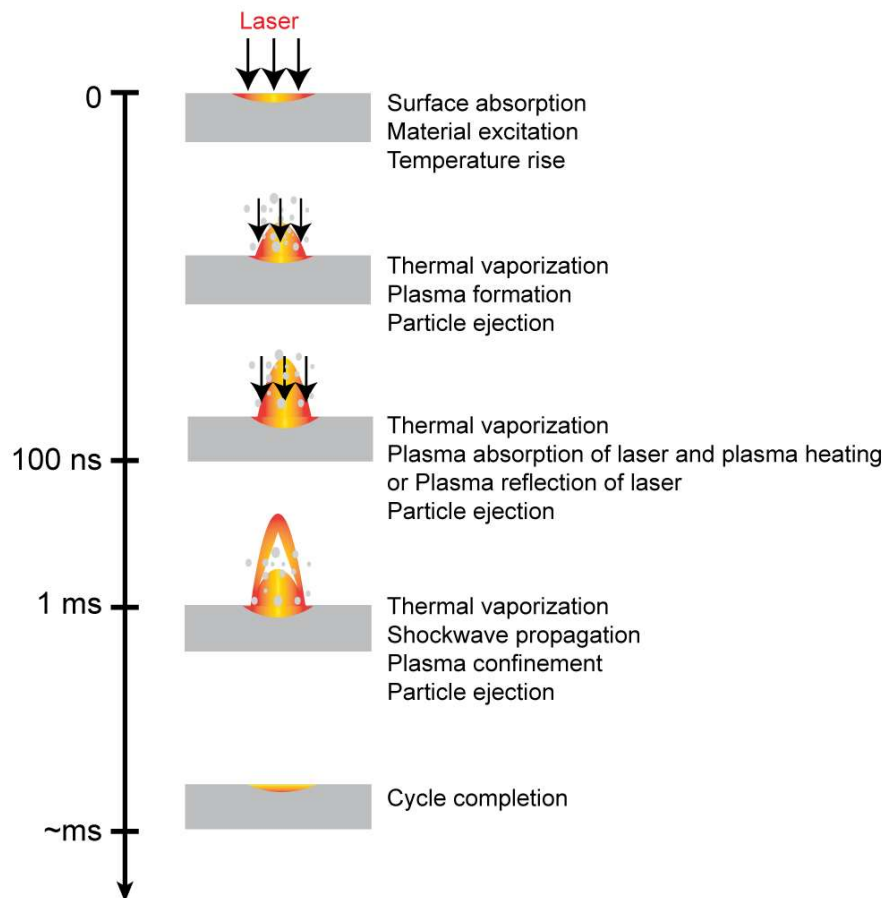


Fig. 2.2-8 Approximate timescales of various process involved in a nanosecond (for example 100 ns) laser irradiation [98].

In a pulsed laser processing, several processes exist for material ablation. Fig. 2.2-8 shows an example of an approximate timescale of various processes involved in a nanosecond (for example 100 ns) laser irradiation. Within the 100 ns pulse interaction time, a sample surface temperature raises to the melting and the vaporization temperature that led to the vapor ejection. During the vaporization, the laser radiation can also be absorbed in the vapor, and the vapor may become ionized through the various physical processes, not only a heating, but also a direct interaction of the laser radiation with carriers in the formed plasma [89,96,99,100]. Created plasma plumes may effectively shield the sample surface against further laser radiation, making processes ineffective at least for the residual duration of the currently applied laser

pulse [101,102]. However, the plasma may be heated by the laser and may affect the processing [86,88]. After, 100 ns shockwave and plasma confinement may occur [98]. Particle ejection from the glass surface will be finished around in millisecond range after the irradiation of a 100 ns pulse.

2.2.3 Importance of laser pulse shape in processing

In a pulsed CO₂ laser, various types of laser pulses such as a short pulse with a pulse width of 10 ns to 400 ns without a pulse tail [25], a short pulse with a spike pulse width of 10 ns to 400 ns and a pulse tail length of about 10 μs to 100 μs [103] and a long pulse with a pulse width of 10 μs to 1.0 ms [6] can be produced as shown in Fig. 2.2-9.

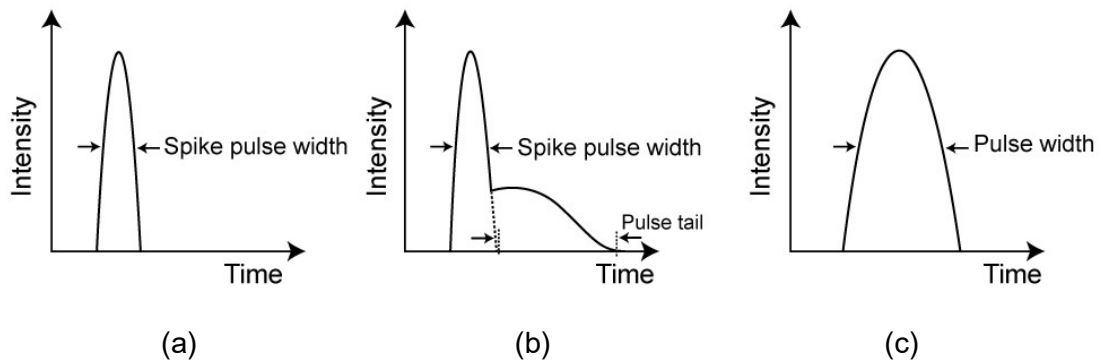


Fig. 2.2-9 Schematic of various pulse shapes in a CO₂ laser. (a) Short pulse without a pulse tail. (b) Short pulse with a spike pulse and a pulse tail. (c) Long pulse.

Fig. 2.2-10 shows examples of the short pulses without a pulse tail, and the pulse width was 45 ns to 170 ns. The short pulses without a pulse tail are produced by a Q-switched CO₂ laser, a TEA (Transversely excited atmospheric) CO₂ laser and a longitudinally excited CO₂ laser. To produce a short pulse without a pulse tail in a TEA CO₂ laser and a longitudinally excited CO₂ laser, an adjustment of a gas medium and use of a fast discharge are important. To control the pulse width of about several tens of nanoseconds, a plasma shutter in a TEA CO₂ laser has been reported [104]. To control the pulse width of about 100 ns to 400 ns, an adjustable optical cavity in a longitudinally excited CO₂ laser has been reported [25]. To control the pulse width of about several nanoseconds, a semiconductor switching facilitated by a ruby laser in a TEA CO₂ laser has been reported [105,106]. In a short pulse without a pulse tail, heat

will be generated only by the spike pulse energy and gives thermal processing with a small thermal effect.

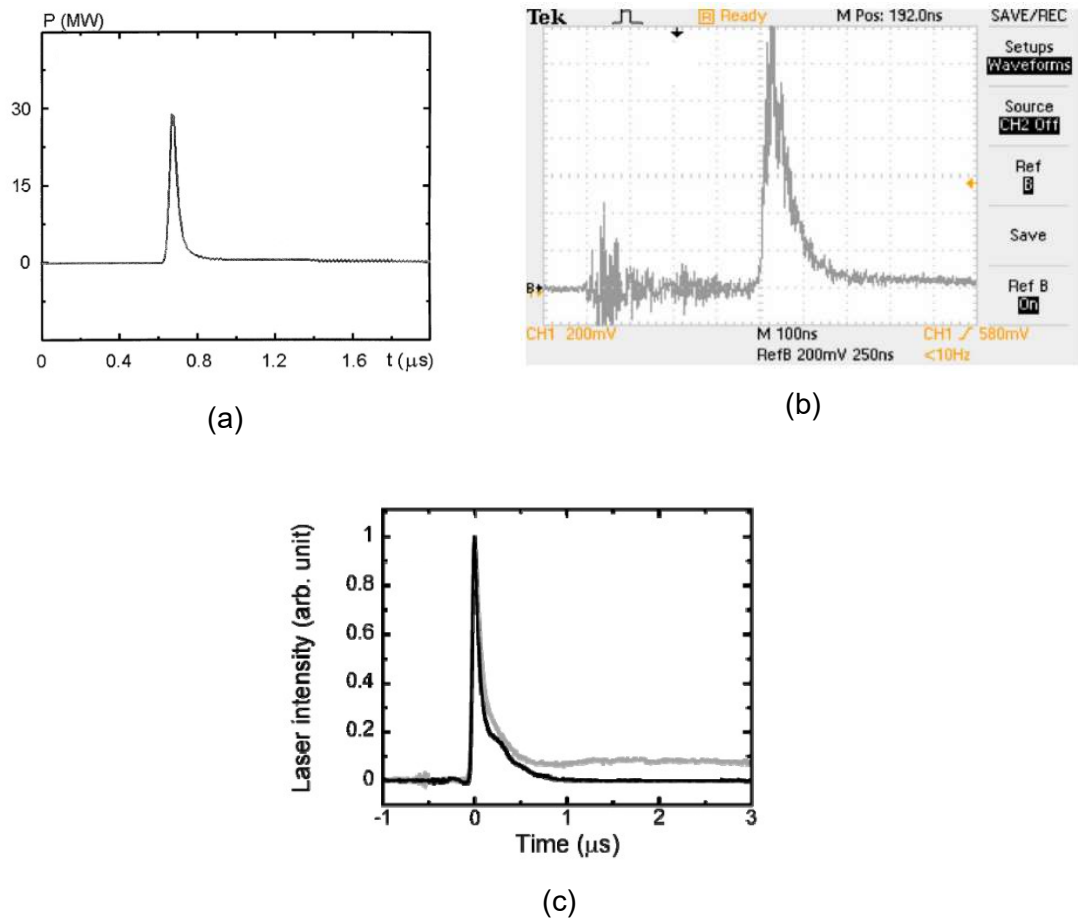


Fig. 2.2-10 Example of short pulses without a pulse tail in a pulsed CO₂ laser. (a) Short pulse with a pulse width of 45 ns by a TEA CO₂ laser [107]. (b) Short pulse with a pulse width of 170 ns by a TEA CO₂ laser [70]. (c) Short pulse with a pulse width of 110 ns by a longitudinally excited CO₂ laser [29].

Fig. 2.2-11 shows examples of the short pulses with a pulse tail, and the spike pulse width and the pulse tail length were 50 ns to 200 ns and 5.0 μs to 200 μs, respectively. The short pulses with a spike pulse and a pulse tail are produced by a TEA CO₂ laser and a longitudinally excited CO₂ laser. To control the pulse tail length and the pulse tail energy in a TEA CO₂ laser and a longitudinally excited CO₂ laser, an adjustment of a gas medium and/or an excitation circuit are important. To control the energy ratio of a spike pulse to a pulse tail of 1:0 to 1:200, adjustment of a gas medium and an excitation circuit in a longitudinally excited laser CO₂ laser has been reported [26,27]. In a short pulse with a spike pulse and a pulse tail, heat will be generated by

the spike pulse energy and the pulse tail energy. A spike pulse gives thermal processing with a small thermal effect and a pulse tail gives thermal processing with a large thermal effect.

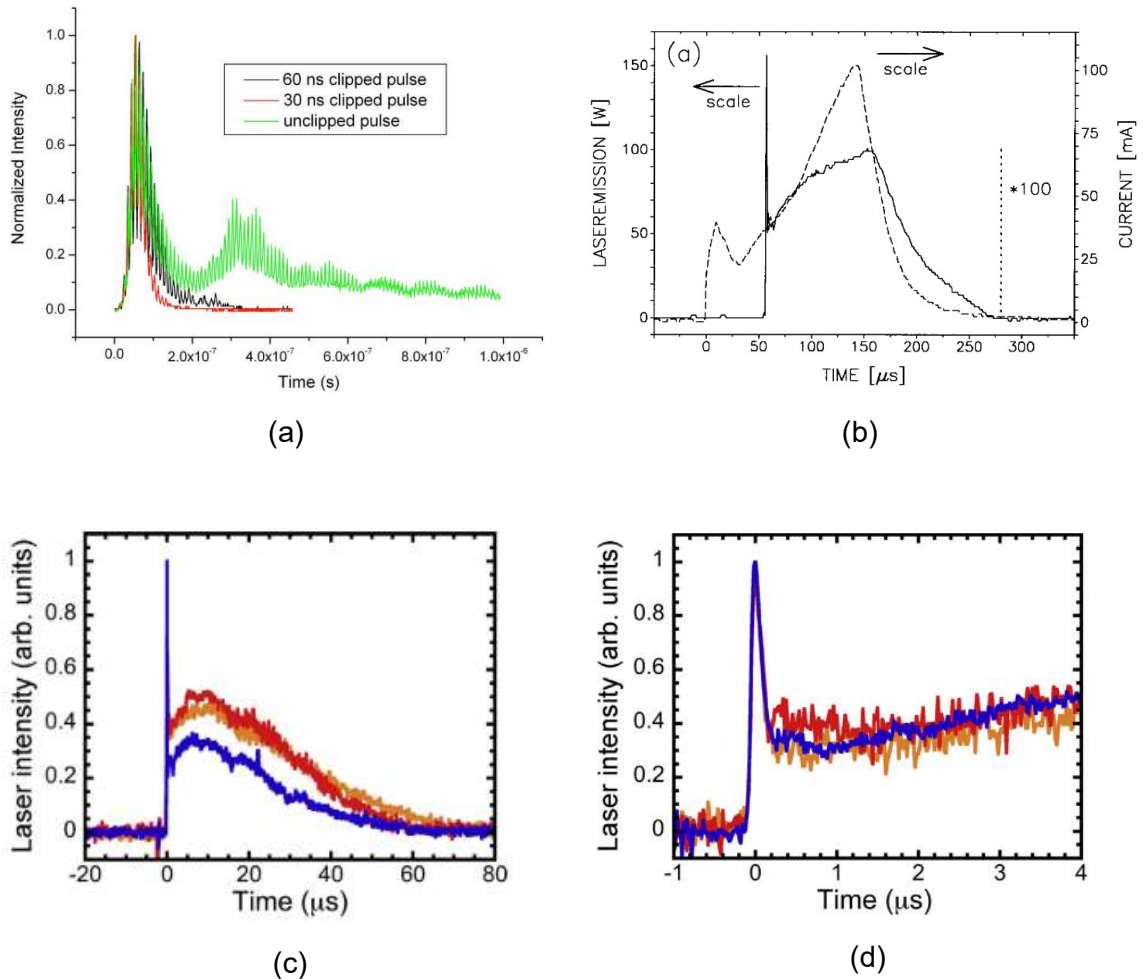


Fig. 2.2-11 Examples of short pulses with a pulse tail in a pulsed CO₂ laser. (a) Short pulse with a spike pulse width of 50 ns and a pulse tail length of about 5.0 μ s by a TEA CO₂ laser [104]. (b) Short pulse with a spike pulse width of 120 ns and a pulse tail length of about 200 μ s by a longitudinally CO₂ laser [108]. (c) Overall and (d) magnified time scale waveform of the short pulse with a spike pulse width of 200 ns and a pulse tail length of about 60 μ s by a longitudinally excited CO₂ laser [26].

Fig. 2.2-12 shows examples of the long pulses, and the long pulse width was 20 μ s to 1000 μ s. The long pulses are produced by a RF (Radio frequency) excited CO₂ laser and a CW CO₂ laser using an electrical switching, a longitudinally excited CO₂ laser using slow discharge, a longitudinally excited CO₂ laser using multiple discharge circuits, and a TE (Transversely excited) CO₂ laser using a special spiker-sustainer

circuit. To control the long pulse width of 1.0 μs to 100 μs and about several milliseconds, electrical switching in a RF excited CO_2 laser and a CW CO_2 laser has been reported [109,110]. To control the long pulse width of about 10 μs to 3.0 ms, adjustment of the discharge formation time with slow discharge in a longitudinally CO_2 laser has been reported [26,111]. To control the long pulse width of 250 μs to 1000 μs , a multiple discharge circuits in a longitudinally excited CO_2 laser has been reported [112]. To control the long pulse width of about 20 μs , a special spiker-sustainer circuit in a TE CO_2 laser has been reported [113]. A long pulse gives a thermal processing and a large thermal effect. In CO_2 laser processing of glass, thermal effect produces thermal damage such as cracks, HAZ and debris.

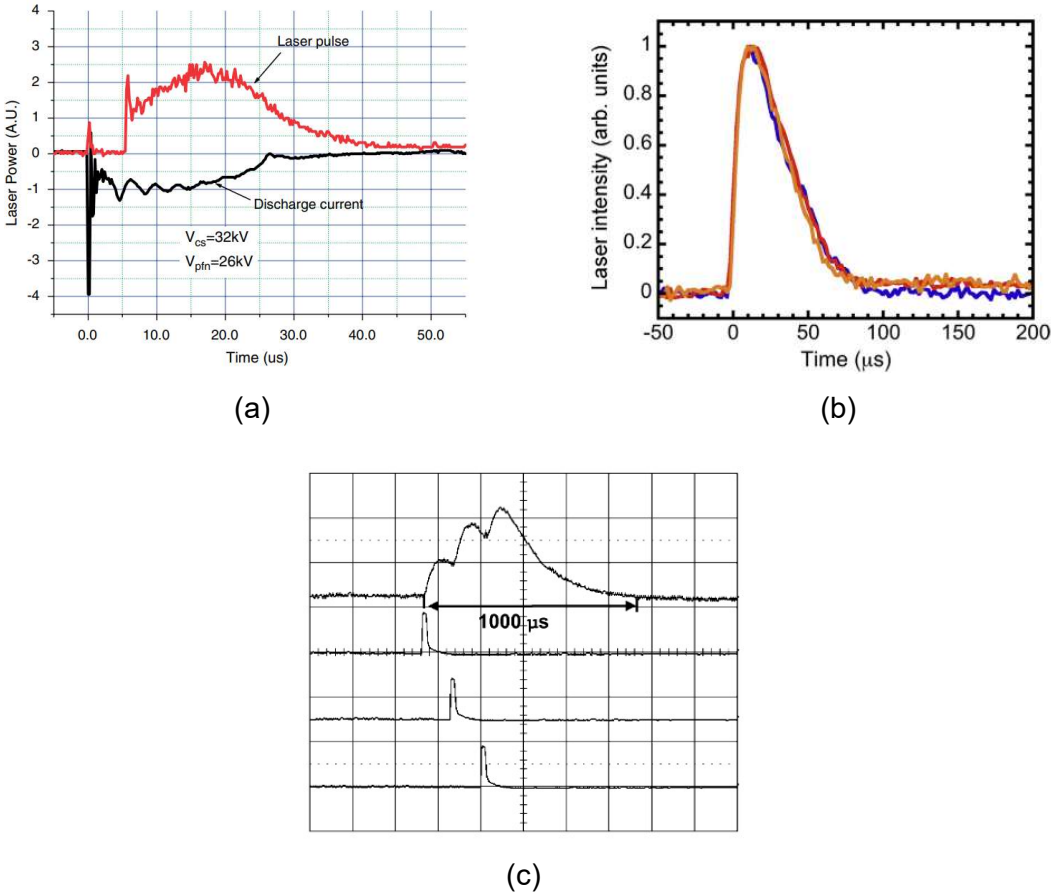


Fig. 2.2-12 Examples of long pulses in a pulsed CO_2 laser. (a) Long pulse with a pulse width of 20 μs by a TE CO_2 laser using a special spiker-sustainer circuit [113]. (b) Long pulse with a pulse width of 40 μs by a longitudinally excited CO_2 laser [26]. (c) Long pulse with a pulse width of 250 μs to 1000 μs by a longitudinally excited CO_2 laser using multiple discharge circuits [112].

Therefore, to realize fine microfabrication in CO₂ laser processing, it is important to consider the laser pulse shape. In the previous studies on a longitudinally excited CO₂ lasers, the control of the spike pulse width was 137 ns to 332 ns by adjusting the optical cavity length [25]. The control of the pulse tail energy was 1.0 to 200 times of the spike pulse energy by adjusting a gas medium [27] and an excitation circuit [26]. The control of the long pulse width was 10 μs to 100 μs by adjusting of a gas medium [27] and an excitation circuit [26], and 250 μs to 1000 μs by adjusting a discharge time of a discharge tube with three pulsed power supply [112]. In this thesis, a longitudinally excited CO₂ laser with a spike pulse width of about 250 ns, a pulse tail length of 31.4 μs to 134.7 μs and an energy ratio of a spike pulse to the pulse tail of 7.0 to 92.0 was used for the investigation of a glass drilling characteristic.

2.2.4 Importance of laser beam profile in processing

A laser can produce various kinds of laser beams such as a gaussian beam, a doughnut beam and a flat-top beam. A laser beam profile defines the spatial distribution of a laser intensity. Fig. 2.2-13 shows the schematic of the intensity distribution in various types of laser beam profiles.

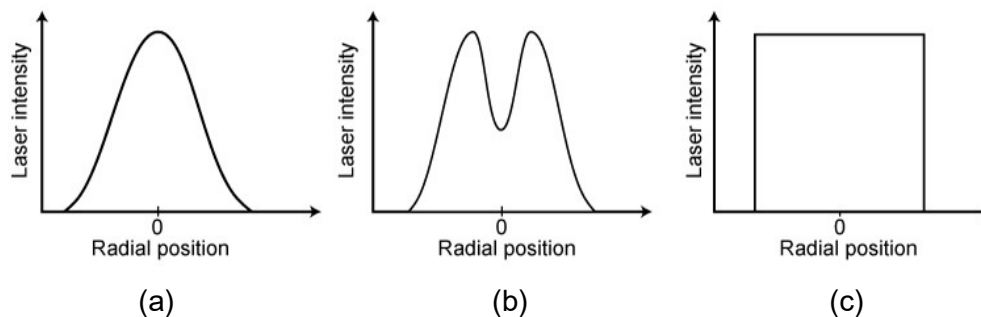


Fig. 2.2-13 Schematic of various laser beam profiles. (a) Gaussian beam. (b) Doughnut beam. (c) Flat-top beam.

In laser processing, the laser beam is focused by a focusing lens as shown in Fig. 2.2-14. Where, D is the beam diameter [mm] before the focusing lens, f is the focal length [mm] of the lens, and λ is the wavelength [μm] of the laser light, DOF (Depth of focus) is the depth of focus [μm] and d is the focus spot diameter [μm]. The beam propagation along the z -axis as shown in the Fig. 2.2-15 is expressed by the following equation:

$$w(z) = w_0 \sqrt{1 + \left(\frac{z}{z_R}\right)^2} \quad \text{Eq. 2.2-6}$$

Where, $w(z)$ is the propagation along the z -axis, w_0 is the beam waist radius [μm] that is $d/2$, and z_R is the Rayleigh length [μm] and is defined by:

$$z_R = \frac{\pi w_0^2}{\lambda} \quad \text{Eq. 2.2-7}$$

Where, w_0 is the beam waist radius that is $d/2$ [μm], and λ is the wavelength [μm].

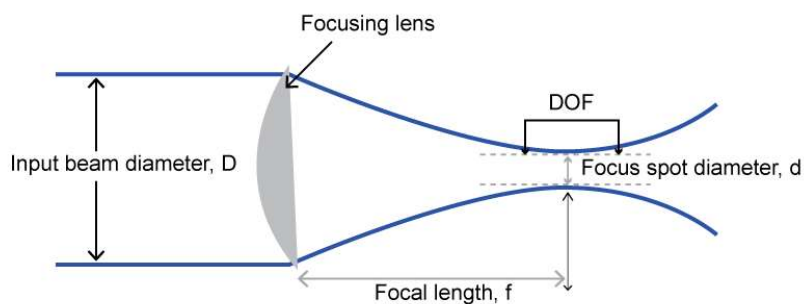


Fig. 2.2-14 Schematic of a laser beam focusing.

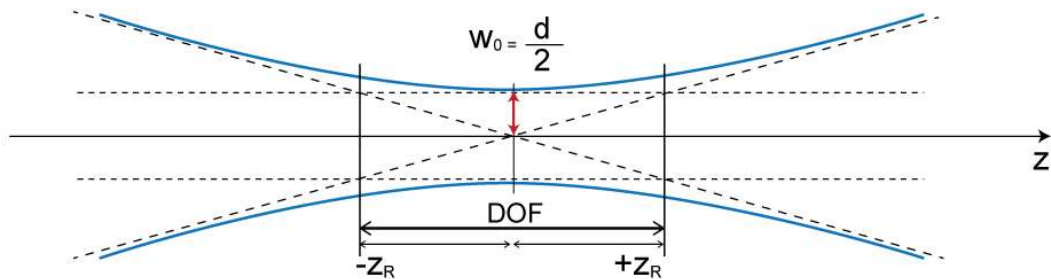


Fig. 2.2-15 Beam propagation along the z -axis.

The focus spot diameter that is the smallest diameter at the focal plane is expressed by Eq. 2.2-8. The DOF that is the length on both side from a focus spot diameter to where a diameter is with $\sqrt{2}$ times the focus spot diameter and the DOF is the twice of the Rayleigh length is expressed by Eq. 2.2-9. The Rayleigh length that is the length on either side from the focus spot diameter to the point where a diameter increased by a factor of $\sqrt{2}$ and is expressed by Eq. 2.2-10. The NA (Numerical aperture) that is the ratio of the input laser beam diameter and the focal length of the lens is expressed by the Eq. 2.2-11.

$$\text{Focus spot diameter, } d = \frac{4M^2\lambda f}{\pi D} = \frac{2M^2\lambda}{\pi} \left(\frac{1}{NA} \right) \quad \text{Eq. 2.2-8}$$

$$\begin{aligned} \text{Depth of focus, DOF} &= \frac{8M^2\lambda}{\pi} \left(\frac{f}{D} \right)^2 \\ &= \frac{2M^2\lambda}{\pi} \left(\frac{1}{NA} \right)^2 \end{aligned} \quad \text{Eq. 2.2-9}$$

$$\text{Rayleigh length, } Z_R = \frac{4M^2\lambda}{\pi} \left(\frac{f}{D} \right)^2 = \frac{M^2\lambda}{\pi} \left(\frac{1}{NA} \right)^2 \quad \text{Eq. 2.2-10}$$

$$\text{Numerical aperture, } NA = \frac{D}{2f} \quad \text{Eq. 2.2-11}$$

In Eq. 2.2-8, the beam quality factor M^2 influences the spot diameter in various laser beam profiles with a same input beam diameter and a focal length of the focusing lens. For instance, when an M^2 value is 1.0 which is refer to as a perfect gaussian beam. The M^2 value of 1.0 is difficult to produce in a practical laser. Fig. 2.2-16 shows the dependence of a spot diameter on an f/D and an M^2 . For example, an input diameter D of 22.0 mm and a focal length f of 38.1 mm resulting in an f/D of 1.73 at a wavelength λ of 10.6 μm will produce a spot diameter of 23.3 μm , 46.6 μm and 70.0 μm in an M^2 of 1.0, 2.0 and 3.0, respectively.

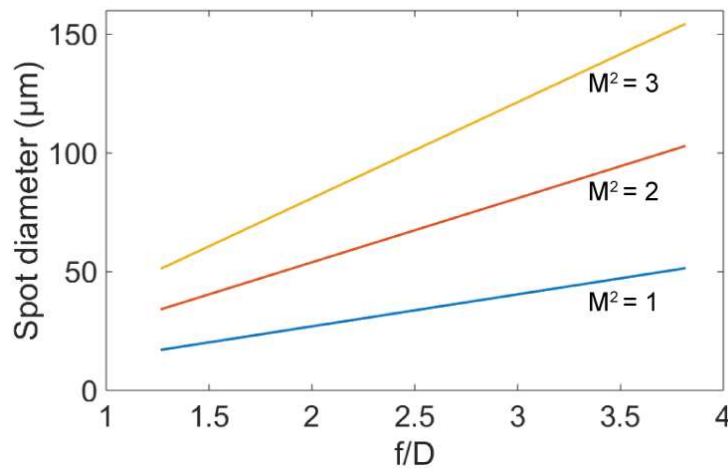


Fig. 2.2-16 Relation of the spot diameter with the f/D and the M^2 .

However, when an input laser beam is focused by a focusing lens, a beam profile at the focal plane is identified by the Fourier transform of the input beam profile function. Based on diffraction theory, the resulting beam profile at the focal plane of a

focusing lens is proportional to the Fourier transform of the input laser beam [114,115]. For instance, the Fourier transform of a gaussian function is still a gaussian function [114]. Eq. 2.2-12 shows the function of a gaussian beam. Where, w_0 is the input laser beam waist radius [mm]. Eq. 2.2-13 shows the Fourier transform of the gaussian function and the Fourier transform of an exponential term in a gaussian function also gives an exponential term. Therefore, the beam profile at the focal plane is gaussian. Fig. 2.2-17 shows a schematic of a gaussian beam profile at the lens entrance and at the focal plane for an input laser beam diameter of 22 mm, a focal length of the focusing lens of 38.1 mm and a wavelength of 10.6 μm . The calculated focus spot diameter at the focal plane using Eq. 2.2-8 is $M^2 \times 0.023$ mm. The M^2 value of an ideal gaussian laser beam with a TEM_{00} (Transverse electromagnetic) mode has a value of $1+2n = 1+2 \times 0 = 1.0$ [116]. Therefore, the focus spot diameter in an ideal gaussian laser beam is 23.3 μm at an f/D of 1.73.

$$f(x) = \exp\left(-\frac{2x^2}{w_0^2}\right) \quad \text{Eq. 2.2-12}$$

The Fourier transform of the gaussian function is:

$$\begin{aligned} X(\omega) &= \int_{-\infty}^{\infty} f(x)e^{-j\omega x} dx \\ &= w_0 \sqrt{\frac{\pi}{2}} \exp\left(-\frac{\omega^2}{2w_0^2}\right) \end{aligned} \quad \text{Eq. 2.2-13}$$

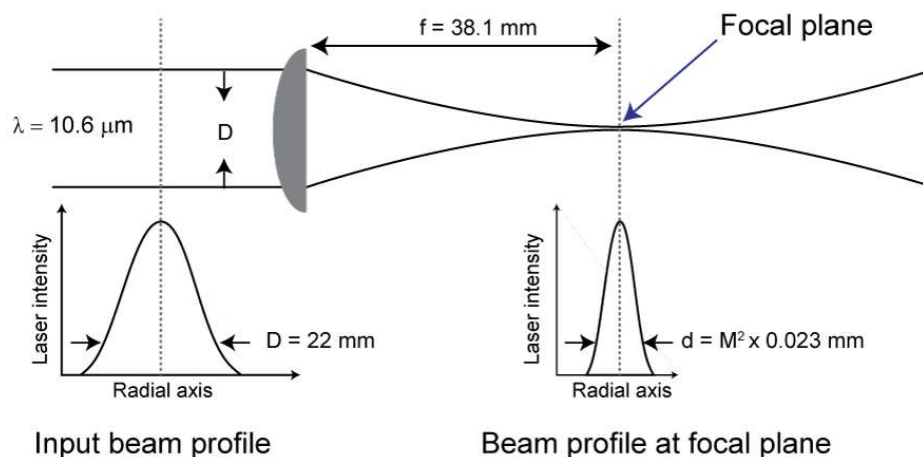


Fig. 2.2-17 Schematic of a gaussian beam profile at the focusing lens entrance and at the focal plane.

In the case of a doughnut laser beam, the beam distribution consists of two gaussian functions with a subtraction with each other. Eq. 2.2-14 shows the function of a doughnut laser beam. Where, w_1 the input laser beam waist radius [mm] and w_2 is the distance between two gaussian peak [mm]. Eq. 2.2-15 shows the corresponding Fourier transform and the Fourier transform of two exponential terms in a doughnut function also gives two exponential terms. Therefore, the beam profile at the focal plane is doughnut. Fig. 2.2-18 shows a schematic of a doughnut beam profile at the lens entrance and at the focal plane for an input laser beam diameter of 22 mm, a focal length of the focusing lens of 38.1 mm and a wavelength of 10.6 μm . The calculated focus spot diameter at the focal plane using Eq. 2.2-8 is $M^2 \times 0.023$ mm. The M^2 value of an ideal doughnut laser beam with a TEM_{01} mode has a value of $1+2n = 1+2 \times 1 = 3.0$ [116]. In addition, the M^2 value of an ideal doughnut laser beam with a TEM_{01}^* and an LG_{01} (Laguerre-Gaussian) mode is 2.0 [117]. Therefore, the focus spot diameter in an ideal doughnut laser beam is 70.1 μm and 46.6 μm in an M^2 of 3.0 and 2.0 at an f/D of 1.73, respectively.

$$f(x) = \exp\left(-\frac{2x^2}{w_1}\right) - \exp\left(-\frac{2x^2}{w_2}\right) \quad \text{Eq. 2.2-14}$$

The Fourier transform of the doughnut function is:

$$\begin{aligned} X(\omega) &= \int_{-\infty}^{\infty} f(x)e^{-j\omega x} dx \\ &= w_0\sqrt{\frac{\pi}{2}} \exp\left(-\frac{\omega^2}{2w_1}\right) - w_0\sqrt{\frac{\pi}{2}} \exp\left(-\frac{\omega^2}{2w_2}\right) \end{aligned} \quad \text{Eq. 2.2-15}$$

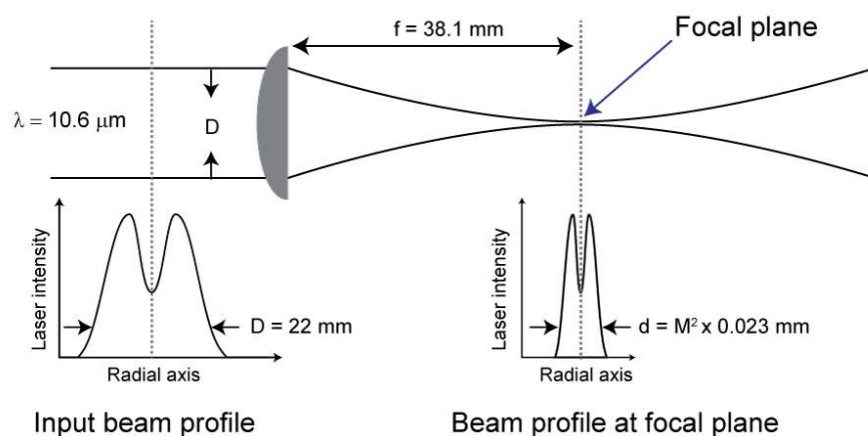


Fig. 2.2-18 Schematic of a doughnut beam profile at the focusing lens entrance and at the focal plane.

In the case of a flat-top laser beam, the beam distribution is a unit rectangular function. Eq. 2.2-16 shows the function of a unit rectangle to represent a flat-top laser beam. Where, w_0 is the input laser beam waist radius [mm]. Eq. 2.2-17 shows the corresponding Fourier transform and the Fourier transform of a unit rectangular function gives a *sinc* function. Therefore, the beam profile at the focal plane is the airy disk pattern. Fig. 2.2-19 shows a schematic of a flat-top beam profile at the lens entrance and at the focal plane for an input laser beam diameter of 22 mm, a focal length of the focusing lens of 38.1 mm and a wavelength of 10.6 μm . The calculated focus spot diameter at the focal plane using Eq. 2.2-8 is $M^2 \times 0.023$ mm. In an ideal flat-top laser beam the M^2 is larger than 1.0 for an example M^2 of 5.0 and 10 will give a focus spot diameter of 116 μm and 233 μm at an f/D of 1.73.

$$f(x) = \begin{cases} 1 & ; \text{for } -w_0 \leq x \leq w_0 \\ 0 & ; \text{for otherwise} \end{cases} \quad \text{Eq. 2.2-16}$$

The Fourier transform of the unit rectangular function is:

$$\begin{aligned} X(\omega) &= \int_{-\infty}^{\infty} f(x)e^{-j\omega x} dx \\ &= 2w_0 \text{sinc}(\omega w_0) \end{aligned} \quad \text{Eq. 2.2-17}$$

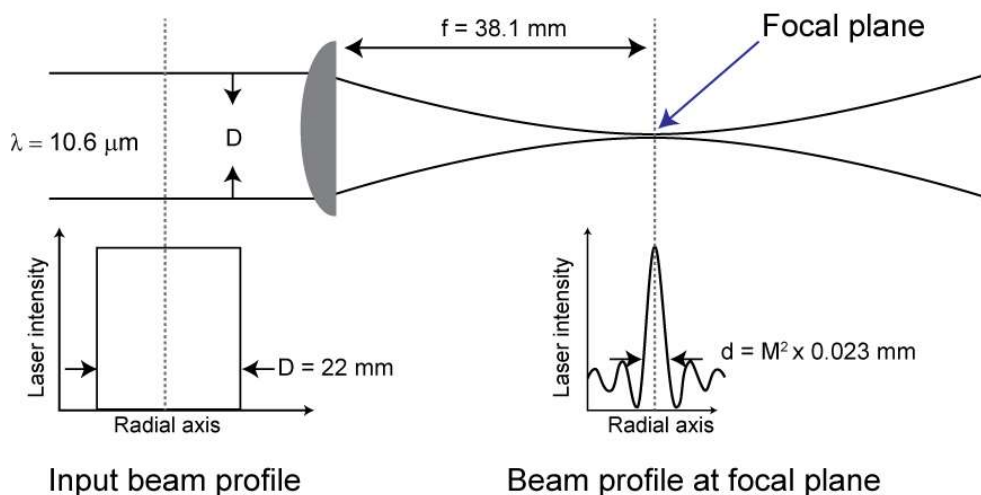


Fig. 2.2-19 Schematic of a flat-top beam profile at the focusing lens entrance and at the focal plane.

Fig. 2.2-20 (a) shows the input beam profile with a diameter of 22 mm for a gaussian laser beam, a doughnut laser beam and a flat-top laser beam. In a gaussian

laser beam, the intensity is the highest in the center of the radial axis and gradually decay from the center of the radial axis. In a doughnut laser beam, the intensity is the lowest at the center of the radial axis and increases towards the highest intensity at a finite radius at both sides from the center of the radial axis, then decreases again. In a

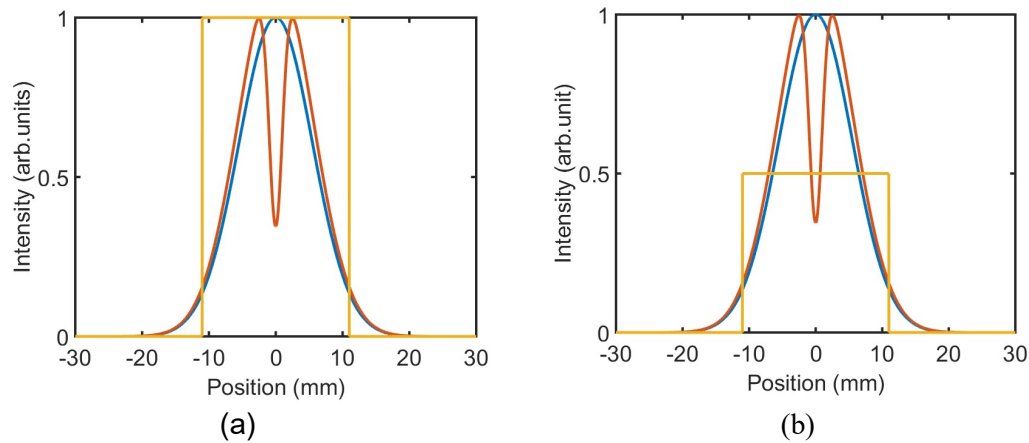


Fig. 2.2-20 Comparison of the various laser beams before focusing. Blue, orange and yellow colors represent a gaussian laser beam, a doughnut laser beam and a flat-top laser beam respectively. (a) Laser beam profiles with a diameter of 22 mm before focusing by a focusing lens with a focal length of 38.1 mm with normalized peak intensity of 1. (b) Peak intensities in various laser beam profiles, maximum value of a gaussian laser beam is normalized as 1. The MATLAB code for beam plotting is presented in APPENDIX 2.II.

flat-top laser beam, the laser intensity is uniformly distributed within the radial axis. Fig. 2.2-20 (b) shows the peak intensity comparison in a gaussian laser beam, a doughnut laser beam, and a flat-top laser beam. In the same amount of power, the peak intensity in a gaussian laser beam and a doughnut laser beam is twice that of a flat-top laser beam. Fig. 2.2-21 (a) shows the transformed beam profile at the focal plane of a focusing lens with a focal length of 38.1 mm in various beam profiles. In various beam profiles due to the variation in M^2 , the spot diameters are also changed despite a same f/D of 1.73. The peak intensities are normalized to the peak intensity of the gaussian laser beam. The spot diameter in the gaussian laser beam, the doughnut laser beam and the flat-top laser beam are 23.3 μm , 70.1 μm and 116 μm , respectively. A gaussian laser beam gives a small spot diameter. Therefore, a gaussian laser beam will give small size processing. Fig. 2.2-21 (b) shows the normalized peak intensity for each beam to the maximum value of 1.0. Fig. 2.2-21 (c) shows the transformed beam profiles at the focal plane of a focusing lens with a focal length of 38.1 mm in the same

M^2 of 5.0 and an f/D of 1.73. The spot diameters are same and $116 \mu\text{m}$ in the gaussian laser beam, the doughnut laser beam and the flat-top laser beam.

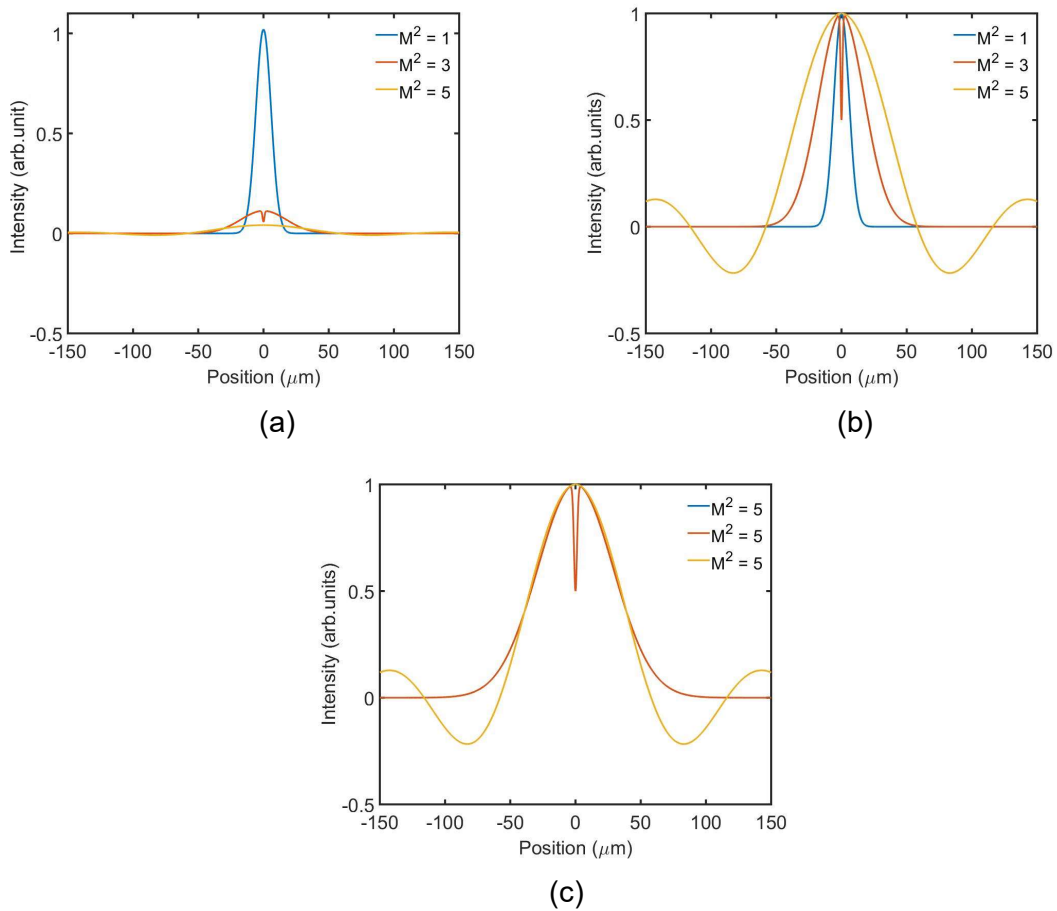


Fig. 2.2-21 Comparison of the various laser beams after focusing. Blue, orange and yellow colors represent a gaussian laser beam, a doughnut laser beam and a flat-top laser beam respectively. (a) Laser beam profiles with different M^2 at the focal plane of the lens with peak intensity normalized with the peak intensity of the gaussian laser beam profile. (b) Laser beam profiles with different M^2 at the focal plane of the lens with normalized peak intensity of 1. (c) Laser beam profiles with the same M^2 of 5.0 at the focal plane of the lens with normalized peak intensity of 1. The MATLAB code for beam plotting is presented in APPENDIX 2.III.

A beam profile affects thermal distribution. To consider laser processing characteristics, a laser beam profile is important. However, most common lasers produce a gaussian-type beam. To produce a flat-top laser beam at the focal plane, the input beam should be a gaussian-like laser beam with an airy pattern. The duality property of a Fourier transforms states that if the Fourier transform of a function is itself, then the inverse Fourier transform of the function is the same function. Since the

Fourier transform of the unit rectangular function is the *sinc* function, the inverse Fourier transform of the *sinc* function is the unit rectangular function as shown in Eq. 2.2-18. Therefore, a flat-top laser beam at the focal plane can be produced if the input laser beam has a shape like a *sinc* function as shown in Fig. 2.2-22. On the other hand, to produce a flat-top beam beyond the focal plane that is at the out-of-focus position a focus offset needs to be controlled. Fig. 2.2-23 shows the propagation of a flat-top laser beam through a focusing lens [114,115,118]. When a flat-top laser beam passes through a focusing lens, the beam intensity distribution transforms into higher frequency lobes at the in-focus. The beam intensity reform as a single-peaked *sinc* function that is directly proportional to the Fourier transform of the input flat-top laser beam at the focal plane. As the beam propagates away from the focal plane, the wavefronts begin to spread out and interfere with each other and the profile at focal plane gradually reforms the flat-top beam profile at an out-of-focus region. The recovered flat-top laser beam can be utilized in glass drilling with a proper adjustment of a focus offset and an out-of-focus drilling approach could produce a cylindrical hole.

The inverse Fourier transform of a *sinc* function is:

$$\begin{aligned}
 f(x) &= \int_{-\infty}^{\infty} \text{sinc}(\omega w_0) e^{-j\omega x} dx \\
 &= \text{rect}(x)
 \end{aligned}
 \tag{Eq. 2.2-18}$$

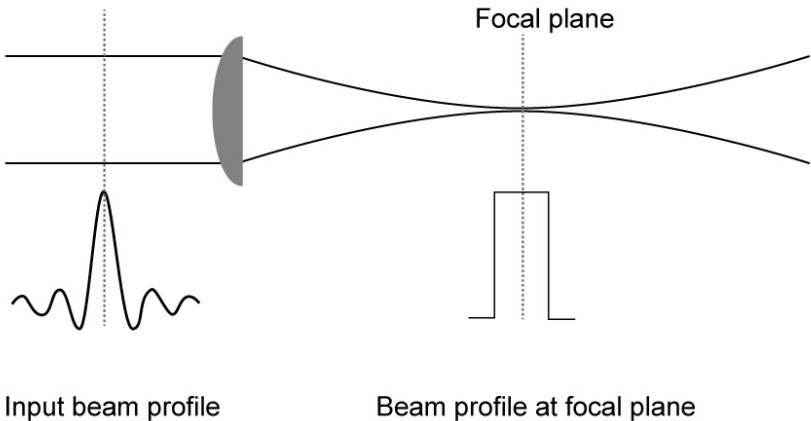


Fig. 2.2-22 Schematic of an airy beam profile at the focusing lens entrance and a flat-top beam profile at the focal plane.

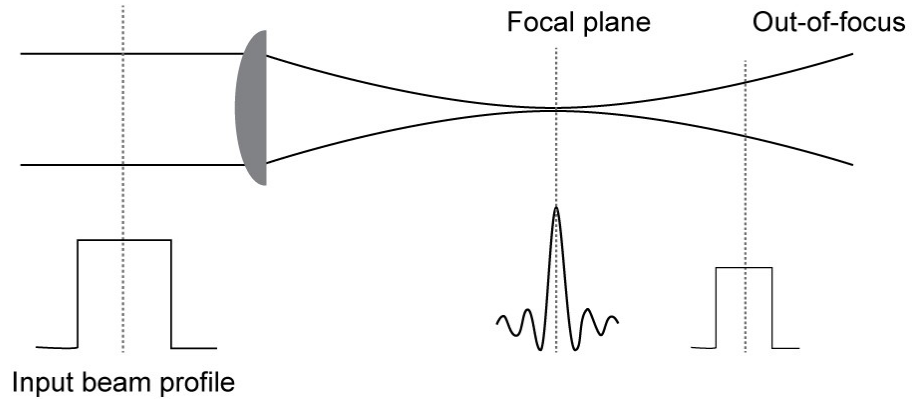
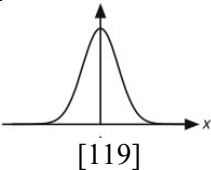
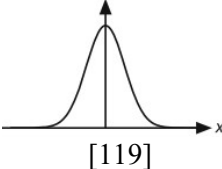
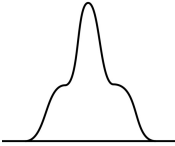
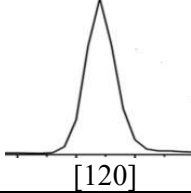
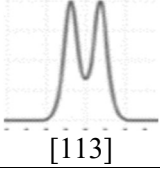
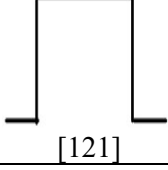
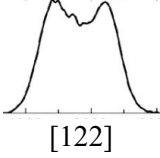


Fig. 2.2-23 Schematic of a flat-top beam at the focusing lens entrance and generation of a flat-top beam profile at the out-of-focus.

However, apart from the ideal shape of a laser beam such as a gaussian beam, a doughnut beam and a flat-top beam, various arbitrary laser beam shape such as a gaussian-like beam, a central-peak-intensity with large-shoulders beam, a central-peak-intensity beam and a flat-top-like beam can be seen in a practical laser. In this thesis, the various beam profiles were defined as Table 2.2-1.

In this thesis, the dependence of drilling characteristics such as a hole shape, a hole depth, a surface hole diameter, a ratio of a surface hole diameter to an irradiation diameter, a surface HAZ diameter, a ratio of a surface HAZ diameter to an irradiation diameter, a taper angle, an aspect ratio and etc. on various laser parameters including a beam profile such as a gaussian-like beam, a central-peak-intensity with large-shoulders beam, a central-peak-intensity beam and a flat-top beam was investigated.

Table 2.2-1 Various beam profiles.

Beam profile name	Beam quality factor M^2	Beam profile	TEM mode
Gaussian	1.0 to 1.6		TEM_{00}
Gaussian-like	2.0 to 3.0		TEM_{00}
Central-peak intensity with large-shoulders	3.0 to 8.0		Superposition of TEM_{00} and TEM_{01}^*
Central-peak-intensity	3.0 to 8.0		TEM_{00}
Doughnut	2.0 to 6.0		TEM_{01}^* , LG_{01}
Flat-top	12.0 to 20.0 or more		TEM_{00}
Flat-top like	8.0 to 12.0		TEM_{00}


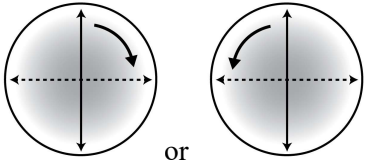
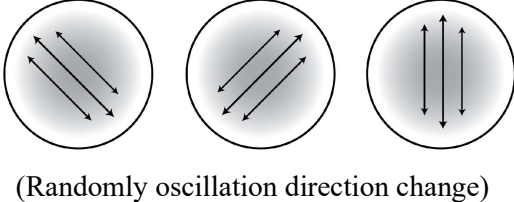
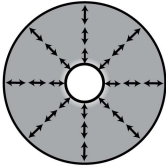
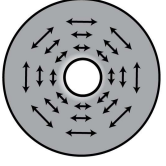
2.2.5 Laser beam polarization

The polarization of a laser beam refers to the direction in which the electric field vector of the electromagnetic wave oscillates. Table 2.2-2 shows the various polarization type such as a linear polarization, a circular polarization, a random polarization, a radial polarization and an azimuthal polarization in a laser beam. In a linear polarization, the electric field vector oscillates in a certain linear direction perpendicular to the propagation direction. A linear polarization is produced by using a Brewster window or a polarizer inside the optical cavity of a laser tube [123]. In a circular polarization, the electric field vector oscillates in the circular direction with equal strength but a relative phase change of 90° . A circular polarization is produced by using a quarter-wave plate outside the optical cavity of a laser tube producing a linear polarization or a reflective polarizer inside the optical cavity [123]. In a random polarization, the electric field vector oscillates randomly perpendicular to the propagation direction. A random polarization is produced by a laser tube without using a Brewster window or a polarizer inside the optical cavity. In a radial polarization, the electric field vectors point away from the center of the propagation axis. A radial polarization is produced by using a radially segmented half-wave plate outside of a laser tube producing a linear polarization, using a resonant grating mirror inside the optical cavity, a triple axicon mirror designed for a radial polarization or using a half-wave plate for a laser tube producing an azimuthal polarization [117,124,125]. In an azimuthal polarization, the electric field vectors form rings around the propagation axis. An azimuthal polarization is produced by using an azimuthally segmented half-wave plate outside the optical cavity of a laser tube producing a linear polarization, using a polarization-selective reflector as one of the mirrors inside the optical cavity, a triple axicon mirror designed for a azimuthal polarization or using a half-wave plate for a laser tube producing an radial polarization [117,124,125].

In laser processing, the direction of the laser beam polarization relative to the plane of incidence is crucial as the direction influences laser absorption. The direction of laser beam polarization parallel to the incident plane is called p-polarization and perpendicular to the incident plane is called s-polarization. In a linear polarization, the laser and material surface interaction either occurs in p- or s-polarization. In a circular and a random polarization the laser and material surface interaction is a time average of the p- and s-polarization [124]. In a radial polarization, the laser and material surface

interaction is in p-polarization and in an azimuthal polarization the interaction is in s-polarization [126]. Generally, a linear polarization is used in laser processing. But, depending on the processing such as for cutting a radial polarization and for drilling an azimuthal polarization is suitable [117,124,126,127]. However, to produce vortex beam requires special optical components which makes the device complex and costly. In industries, simple and low-cost laser devices are required. Therefore, in this thesis, glass processing was performed in a simple laser device.

Table 2.2-2 Laser beam polarization types.

Polarization type	Schematic view	Ref.
Linear polarization		[124,127]
Circular polarization		[124,127]
Random polarization		[124,127]
Radial polarization		[124,126,127]
Azimuthal polarization		[124,126,127]

2.2.6 Crack and HAZ formation mechanisms

In laser processing, thermal effects such as cracks, HAZ, recast layer and debris can be formed depending on the laser irradiation conditions and the material properties. Fig. 2.2-24 shows possible various damages by laser processing. As described in section 2.2.2, the heat generated by a nanosecond laser melts and vaporizes the glass. The molten glass is partially ejected from the cavity by the vapor and plasma pressure, but a part of the molten glass remains near the surface. After the end of laser irradiation, the heat dissipates into the bulk of the material.

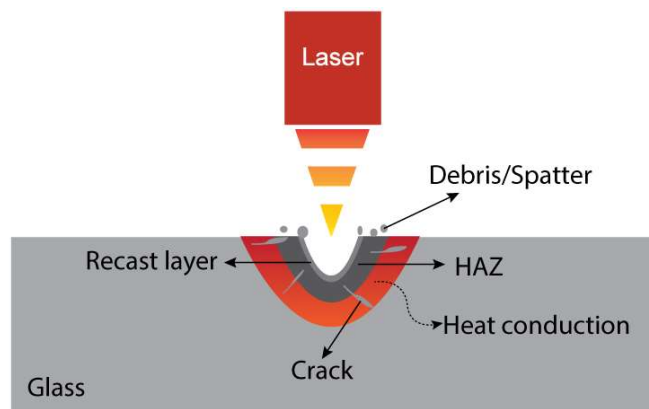


Fig. 2.2-24 Various damages in laser drilling of glass.

In the case of cracks, the rapid temperature gradient produces cracks. Thermal stress gives a tensile stress (σ_t) that can be described by the following equation:

$$\sigma_t = \left(\frac{E \times \alpha}{1 - \nu} \right) \times \Delta T \quad \text{Eq. 2.2-19}$$

Where, σ_t is the tensile stress [Pa], E is the Young's modulus [Pa], α is the thermal expansion coefficient (CTE) [K^{-1}], ν is the Poisson ratio [unit less] and ΔT is the temperature gradient [K] at one position during the laser ablation. Tensile stress (σ_t) is vastly depended on the thermal gradient and the CTE of the material. The thermal expansion involved a pressure load on the material and the ejection of the material, and that the impulse applied to the material is equal to the momentum of the ejected material, based on the conservation law of momentum. Moreover, a rapid heating and a rapid cooling effect causes large temperature gradients. However, the temperature gradient can be controlled by various mechanisms such as by controlling the laser

parameters that are contributed to heat generation and adjusting experiment environmental conditions such as using underwater or pre-heating method.

In the case of HAZ and recast layer, the melt glass that does not reach up to the vaporization temperature remains as melt and HAZ. The recast layer is produced by re-solidification process of the melt. The melting point (MP) of a glass is important in HAZ formation. Debris are generated when the ejected droplet particles are gathered on the entrance of the hole.

2.2.7 Thermal expansion coefficient and melting point of glass

The thermal expansion coefficient (CTE) and the melting point (MP) of a glass are the two crucial parameters to consider during laser processing. The CTE is a measure of the rate at which a material expands each unit change in temperature. In laser processing of glass, a high CTE implies that the glass will undergo significant dimensional changes when heated, which can affect the precision and quality. A glass with a high CTE can suffer from thermal stress and possible cracking when subjected to rapid heating and cooling cycles that is a processing at a high repetition rate. The MP

Table 2.2-3 Basic properties of the various glasses.

Type of glass	CTE	MP	Thermal conductivity	Heat capacity	Density	Ref.
Fused silica glass	$5.5 \times 10^{-7} /K^{-1}$	1600°C	1.3 W/mK	1273 J/kgK	2201 kg/m ³	[128]
Alkali-free glass	$32 \times 10^{-7} /K^{-1}$	971°C	1.0 W/mK	840 J/kgK	2330 kg/m ³	[36]
Borosilicate glass (Pyrex)	$33 \times 10^{-7} /K^{-1}$	820°C	1.1 W/mK	830 J/kgK	2230 kg/m ³	[129]
TFT (Thin film transistor) LCD (Liquid crystal display) glass	$38 \times 10^{-7} /K^{-1}$	667°C	1.3 W/mK	830 J/kgk	2400 kg/m ³	[130]
Borosilicate glass (Schott D263)	$72 \times 10^{-7} /K^{-1}$	736°C	1.2 W/mK	840 J/kgK	2330 kg/m ³	[33]
Soda lime glass	$87 \times 10^{-7} /K^{-1}$	740°C	1.0 W/mK	850 J/kgK	2500 kg/m ³	[6]
Crown glass	$94 \times 10^{-7} /K^{-1}$	724°C	1.3 W/mK	800 J/kgK	2560 kg/m ³	[131]

of a glass is the temperature at which it changes state from solid to liquid. In laser processing of glass, MP of a glass is important in HAZ formation. Table 2.2-3 shows basic properties of the various glasses such as a CTE, an MP, a thermal conductivity, a heat capacity and a density.

2.2.8 CO₂ laser drilling of glass with an extra treatment

CO₂ laser drilling of glass is a thermal process and has thermal effects such as cracks and HAZ. To eliminate thermal damages such as cracks and HAZ, CO₂ laser drilling of glass with various treatment such as pre/post or during-heating a sample, placing a sample under water, flowing a gas onto the processing area or using a PDMS layer on the top of a sample was reported in previous research [33–35,132,133].

- **Pre/post or during-heating treatment**

In a pre/post or during-heating treatment, a glass sample is heated prior, post or during processing to reduce the thermal gradient. In a pre-heating treatment, a glass sample is heated up through external heating source or adjusting the focusing lens just before processing. In a during-heating treatment, the glass sample or the processing area is heated during processing by another heat source. In a post-heating treatment, after completing the drilling process, the entire glass is kept inside an oven to equilibrium the temperature gradient. However, the thermal treatments were required extra times than that of processing without a thermal treatment [33].

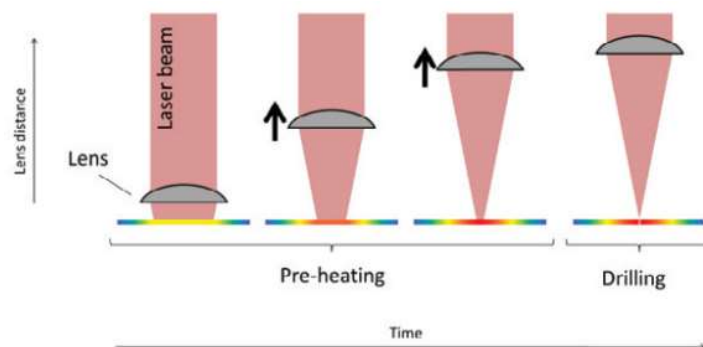


Fig. 2.2-25 CO₂ laser drilling of a borosilicate glass (Schott D263Teco) with a pre-heating treatment [33].

For example, three types of heating methods were reported in CO₂ laser drilling of a borosilicate glass (Schott D263Teco) with a CTE of 72×10^{-7} /K and an MP of 736°C [33]. The one method was pre-heating the glass surface by adjusting the focusing lens position as shown in Fig. 2.2-25. The drilling time was increased due to the lens movement up to 14 s per hole than that of 0.25 s per hole without pre-heating. The second method was heating the entire processing area up to 100°C to 400°C during processing know as during-heating as shown in Fig. 2.2-26. The entire sample was heated up and cracks were prevented with this method. In this method, the drilling time was same as of 0.25 s per hole without heating [33]. The third method was a post-heating treatment, where, after the drilling process, the entire glass sample was placed inside an oven for thermal relaxation of the induced stress. Curing at a temperature of 529°C for 30 minutes removes the stress completely.

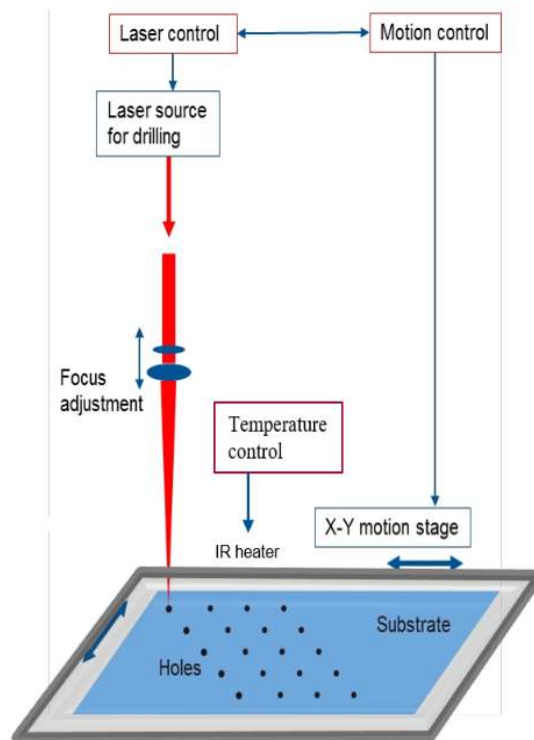


Fig. 2.2-26 CO₂ laser drilling of a borosilicate glass (Pyrex 7740) with a during-heating treatment [135].

- **Liquid assisted treatment**

In a liquid assisted or an underwater treatment, a glass sample is submerged in a liquid or water to eliminate cracks and HAZ as shown in Fig. 2.2-27 [35,130,132,133].

However, in an underwater treatment, a glass sample is required to be submerged into the water with precise control of the water depth. When a glass is submerged in a high depth of water, the irradiated laser beam loses energy or deviates in the water. Therefore, there is a challenge to select the optimum water level to submerge a glass sample into the underwater treatment. Further cleaning of a glass sample is also required in the underwater treatment.

For example, a CW CO₂ laser at an average power of 6 W and 10 passes with a scanning speed of 11.4 mm/s was used in drilling of a borosilicate glass (Pyrex 7740) with a CTE of 33×10^{-7} /K and an MP of 820°C with an underwater treatment [35]. The borosilicate glass was submerged into the water at a depth of 0.5 mm and 1.0 mm. Without water that is drilling in the air produced large cracks around the hole entrance. The high temperature gradient in the air induced a high stress for a crack formation while the small temperature gradient in the water had a less HAZ and eliminated the crack during processing. However, a high water depth required a greater number of passes than a low water depth. Another CW CO₂ laser at an average power of 24 W, 80 passes with a scanning speed of 114 mm/s was used in an underwater processing of a borosilicate glass [83]. In that case, the borosilicate glass was submerged into the water in a depth of 0.3 mm to 1.0 mm. The water depth of 0.3 mm was still produced cracks and 0.5 mm was considered as the optimal water depth.

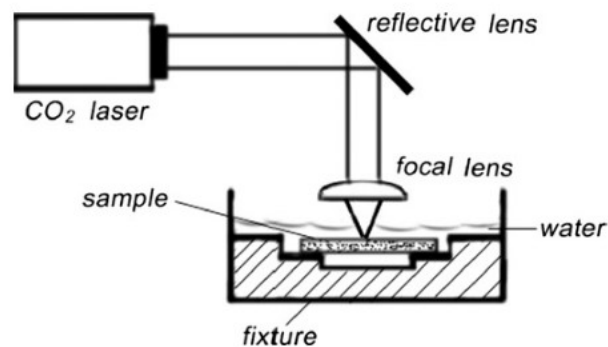


Fig. 2.2-27 CO₂ laser drilling of a borosilicate glass (Pyrex 7740) with an underwater treatment [35].

2.2.9 CO₂ laser drilling of glass without an extra treatment

CO₂ laser drilling of glass without an extra treatment is simple and cost-effective process because extra set-ups are not required. Fig. 2.2-28 shows a schematic of CO₂ laser drilling of a glass without an extra treatment [6].

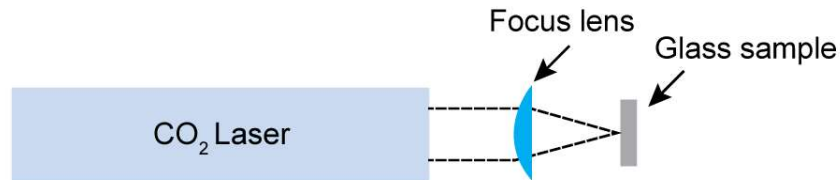


Fig. 2.2-28 Schematic set-up of CO₂ laser drilling of glass without an extra treatment [6].

For example, a long-pulse CO₂-laser drilling without an extra treatment in a fused silica glass with a CTE of 5.5×10^{-7} /K and an MP of 1600°C, in a borosilicate glass (Pyrex 7740) with a CTE of 33×10^{-7} /K and an MP of 820°C and in a soda lime glass with a CTE of 85×10^{-7} /K and an MP of 740°C were reported in [6]. Fig. 2.2-29 (a) shows the image of the fused silica glass surface after processing without an extra treatment [6]. A laser pulse width was varied from 100 μs to 1000 μs to investigate an entrance hole diameter, an exit hole diameter and a melt pile up around the hole. A long pulse with a pulse width of 400 μs or more was necessary in a single-pulse drilling method to produce through hole in a fused silica glass with a thickness of 500 μm at a fluence of 3767 J/cm². The long pulse irradiation did not produce any cracks on the fused silica

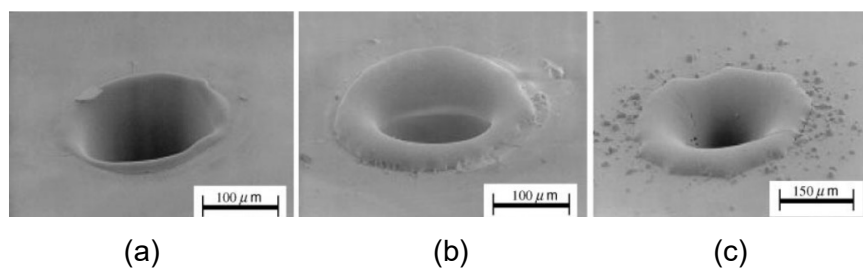


Fig. 2.2-29 CO₂ laser drilling of various glasses without an extra treatment [6]. The processing method was single-pulse drilling. The pulse width was 1000 μs and an irradiation diameter was 130 μm. (a) Fused silica glass. (b) Borosilicate (Pyrex 7740) glass. (c) Soda lime glass.

glass but produced a small melt pile-up around the hole. The low CTE of the fused silica glass gives a resistance against a long pulse irradiation to give a large thermal

damage. Fig. 2.2-29 (b) shows the image of the borosilicate glass surface after processing without an extra treatment [6]. A long pulse with a pulse width of 1000 μs with a single-pulse drilling method produced a through hole in a soda lime glass with a thickness of 500 μm at a fluence of 3767 J/cm^2 . The long pulse melted the glass, which flowed and accumulated at the edges of the hole. The most accumulation occurred in the borosilicate glass where the fused silica glass showed the least accumulation as shown in Fig. 2.2-29 (a) and (b). Fig. 2.2-29 (c) shows the image of the soda lime glass surface after processing without an extra treatment [6]. A long pulse with a pulse width of 1000 μs with a single-pulse drilling method produced a through hole in a soda lime glass with a thickness of 500 μm at a fluence of 3767 J/cm^2 [6]. The long pulse irradiation in the soda lime glass, produced micro cracks and a large amount of melt pile-up and debris in the hole entrance as shown in Fig. 2.2-29 (c). In the through hole drilling of the fused silica glass, the borosilicate glass and the soda lime glass with a thickness of 500 μm , the hole diameter was about 150 μm .

A short pulse with a spike pulse width of 50 ns and a pulse tail length of 1.0 μs produced a hole in a fused silica glass without an extra treatment [23]. Although, to produce a very small hole diameter, a Copper mask grid of 20 $\mu\text{m} \times 20 \mu\text{m}$ was used. The hole diameter was 9.4 μm and a ratio of a surface hole diameter to an irradiation diameter was 0.47, and the hole depth was 0.5 μm and a drilling efficiency was 0.005 $\mu\text{m}/\text{J}/\text{cm}^2$. A thermal damage was not present, but this method was limited to produce deep hole. The maximum hole depth was 0.5 μm .

Table 2.3-4 shows the summary of CO_2 laser drilling of the various glasses with or without an extra treatment. A glass with a high CTE and a low MP was often processed with an extra treatment. For example, drilling of a soda lime glass with a CTE of $85 \times 10^{-7} /\text{K}$ and an MP of 740°C was conducted with a during-heating treatment [135], drilling of a borosilicate glass (D263Teco) with a CTE of $72 \times 10^{-7} /\text{K}$ and a MP of 736°C was conducted with a pre-heating treatment [33], drilling of a TFT LCD glass with a CTE of $38 \times 10^{-7} /\text{K}$ and an MP of 667°C was conducted with an underwater treatment [130]. Without an extra treatment, a glass with a large CTE such as a soda lime glass was attempted to drill with a long pulse CO_2 laser. But the soda lime glass produced micro cracks, large amounts of spatter and HAZ [6]. Therefore, crack-free drilling in a glass with a high CTE and a low MP is yet to be investigated extensively.

2.3 Optimization in CO₂ laser microfabrication of glass

To realize fine microfabrication such as drilling, piercing, grooving and cutting of glass by a CO₂ laser with simple processing scheme, high efficiency and low cost for next generation industries such as the lab-on-a-chip systems, the optoelectronics systems and the MEMS (Microelectromechanical systems), researchers have to investigate below conditions systematically:

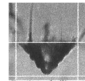
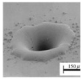
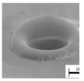
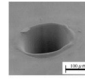
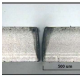
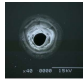
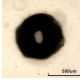
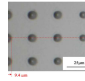
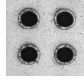
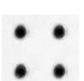
- Dependence on a CO₂ laser wavelength of 9.2 μm to 11.4 μm.
- Dependence on a laser beam polarization of a linear polarization, a circular polarization, a radial polarization, an azimuthal polarization and a random polarization.
- Dependence on a laser beam profile with a gaussian beam with a beam quality factor M^2 of 1.0 to 2.0, a doughnut beam with a beam quality factor M^2 of 2.0 to 4.0 and a flat-top beam with a beam quality factor M^2 of 10 to 20.
- Dependence on a focusing lens with a focal length of 12.7 mm to 100 mm and a NA of 0.10 to 0.90.
- Dependence on a focus offset of -1.00 mm to +1.00 mm.
- Dependence on a laser pulse waveform with a short-pulse with a pulse width of 10 ns to 1000 ns without a pulse tail, a short-pulse with a spike pulse width of about 10 ns to 1000 ns and a pulse tail length of about 1.0 μs to 100 μs and a long pulse with a pulse width of 100 μs to 1.0 ms.
- Dependence on a fluence per single pulse of 1.0 J/cm² to 100 J/cm²
- Dependence on a total irradiation fluence of 1.0 J/cm² to 100000 J/cm²
- Dependence on a repetition rate of 1.0 Hz to 1.0 kHz.
- Dependence on a glass properties such as a CTE of 5.5×10^{-7} /K to 94×10^{-7} /K and an MP of 724°C to 1600°C.
- Dependence on a glass thickness of 10 μm to 5000 μm.

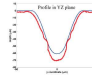
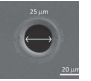
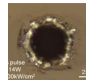

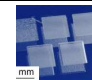
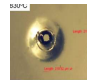

In this thesis, to realize cracks-free hole drilling in a glass, the dependence on the below laser parameters were extensively investigated.

- A CO₂ laser with a wavelength of 10.6 μm.
- A laser beam polarization with a random polarization.
- Dependence on a laser beam profile with a central-peak-intensity with large shoulders beam with a beam quality factor M² of 3.1 to 8.0, a central-peak-intensity beam with a beam quality factor M² of 7.5 and a flat-top beam with a beam quality factor M² of 13.5.
- Dependence on a focusing lens with a focal length of 12.7 mm and 38.1 mm and a NA of 0.15 to 0.50.
- Dependence of a focus offset of -0.20 mm to +0.40 mm.
- Dependence on a laser pulse waveform of a short-pulse with a spike pulse width of 250 ns, a pulse tail length of 31.4 μs to 135 μs and an energy ratio of a spike pulse to a pulse tail of 1:7.1 to 1:92.
- Dependence on a fluence per single pulse of 3.7 J/cm² to 46.8 J/cm².
- Dependence on a total irradiation fluence of 110 J/cm² to 4209 J/cm².
- Dependence on a repetition rate of 1.0 Hz to 400 Hz.
- A crown glass with a CTE of 94×10^{-7} /K and an MP of 724°C.
- A glass thickness of 1150 μm.

In this thesis, by adjusting the laser parameters of a short-pulse CO₂ laser such as a laser beam profile, a focus offset, a laser pulse waveform, a fluence per single pulse, a total irradiation fluence and a repetition rate drilling of a crown glass with a high CTE of 94×10^{-7} /K and an MP of 724°C was investigated without an extra treatment. This thesis realized crack-free holes, a high drilling efficiency of 1.56 μm/J/cm² and a small hole diameter of 28.2 μm by a direct short-pulse CO₂ laser irradiation. Moreover, a cylindrical hole drilling by a flat-top laser beam with the adjustment of the focus offset of a focusing lens with a focal length of 12.7 mm in a percussion drilling method was realized.

Table 2.3-4 Various glass drilling by CO₂ laser with or without extra treatment.

Ref. (Year)	Wavelength	Pulse width	Fluence /pulse Or fluence/s canning (CW)	Rept. Rate	Extra treatment	Hole diameter	Ratio of surface hole diameter to irradiation diameter	Drilling efficiency	Crown glass	Soda lime glass	Borosilicate (D263Teco) glass	TFT LCD glass	Borosilicate (Pyrex 7740) glass	Alkali-free glass	Fused silica glass
[136] (2002)	10.6 μm	5 μs	100 J/cm ²	1 Hz	-	59.0 μm	2.18	0.32 μm/J/cm ²							
[6] (2003)	9.3 μm	1000 μs	3767 J/cm ²	1 Hz	-	150 μm	1.15	0.14 μm/J/cm ²							
[133] (2009)	10.6 μm	CW	277 J/cm ²	N/A	Under water	83.0 μm	1.09	0.02 μm/J/cm ²							
[130] (2009)	10.6 μm	N/A	N/A	1 Hz	Under water	900 μm	6.92	N/A							
[35] (2010)	10.6 μm	CW	692 J/cm ²	N/A	Under water	200 μm	2.63	0.07 μm/J/cm ²							
[23] (2011)	10.6 μm	50 ns	9.6 J/cm ²	1 Hz	Metal masking to reduce hole size	9.40 μm	0.47	0.005 μm/J/cm ²							
[33] (2012)	10.6 μm	N/A	N/A	N/A	Pre-heating	100 μm	N/A	N/A							
[134] (2014)	10.6 μm	N/A	N/A	N/A	Post-heating	55.0 μm	N/A	N/A							

Ref. (Year)	Wavelength	Pulse width	Fluence /pulse	Rept. Rate	Extra treatment	Hole diameter /Shape size	Ratio of surface hole diameter to irradiation diameter	Drilling efficiency	Crown glass	Soda lime glass	Borosilicate (D263Teco) glass	TFT LCD glass	Borosilicate (Pyrex 7740) glass	Alkali-free glass	Fused silica glass
[137] (2014)	10.6 μm	200 μs	43.4 J/cm^2	1 Hz	-	60.0 μm	0.92	0.32 $\mu\text{m}/\text{J}/\text{cm}^2$							
[36] (2015)	9.3 μm	1 μs	N/A	1 Hz	-	25.0 μm	N/A	N/A							
[84] (2015)	10.6 μm	50 μs	25 J/cm^2	250 Hz	-	60.0 μm	0.75	N/A							
[83] (2015)	10.6 μm	380 ns	15 J/cm^2	100 Hz	--	5000 μm (Rect. Size)	25.0	N/A							
[17] (2016)	10.6 μm	130 ns	15.1 J/cm^2	3 Hz	-	324 μm	0.69	0.06 $\mu\text{m}/\text{J}/\text{cm}^2$							
[135] (2020)	10.6 μm	100-1000 μs	20 - 203 J/cm^2	1 Hz	During processing -heating	200 μm	N/A	N/A							
[138] (2020)	10.6 μm	300 ns	89 J/cm^2	1 Hz	-	59.1 μm	0.47	0.32 $\mu\text{m}/\text{J}/\text{cm}^2$							
This study	10.6 μm	250 ns	6.01 - 37.9 J/cm^2	200-400 Hz	-	30.0-366 μm	0.47-0.53	0.61-1.56 $\mu\text{m}/\text{J}/\text{cm}^2$							

APPENDIX 2.I: Temperature distribution calculation.

MATLAB code for the calculation in Fig. 2.2-4 (a) and (b)

```
clc;
clear all;
clear all figure;
%%%%%%%%Define the material properties%%%%%%%%
k=1.38; %Thermal conductivity of glass
p=2201; %for crown glass 2560, for silica glass 2201
cp=1273; %for crown glass 800, for silica glass 1273
diff=k/(p*cp); %Diffusion calculation
%%%%%%%%%%%%%%

%%%%%%%%Temperature distribution calculation from x = 0.0 mm to x = 1.0 mm%%%%%%%%

x=[0:1e-5:1e-3] %Distance in x direction
T0=293+(3000-293)*(exp(-4.74e8.*x.^2)) %function for t=0
t1=1e-6
T1=293+(2500-293).*(1-erf(x/(2*sqrt(diff*t1)))) %function for t= 1 us
t2=100e-6
T2=293+(2000-293).*(1-erf(x/(2*sqrt(diff*t2)))) %function for t= 100 us
t3=1e-3
T3=293+(1800-293).*(1-erf(x/(2*sqrt(diff*t3)))) %function for t= 1 ms
t4=10e-3
T4=293+(1500-293).*(1-erf(x/(2*sqrt(diff*t4)))) %function for t= 10 ms
t5=1
T5=293+(350-293).*(1-erf(x/(2*sqrt(diff*t5)))) %function for t= 1 s

figure(2)
plot(x/1e-3,T0,x/1e-3,T1,x/1e-3,T2,x/1e-3,T3,x/1e-3,T4,x/1e-3,T5,'linewidth',2.2)
set(gca, 'FontSize',26)
set(gca, 'linewidth',2)
xlabel('Distance (mm)', 'fontsize',24)
```

```

ylabel('Temperature (K)','fontsize',24)
legend('t = 0','t = 1 [\mus]','t = 100 [\mus]','t = 1 [ms]','t = 10 [ms]','t = 1 [s]')
legend('boxoff')

```

APPENDIX 2.II. Comparison of various laser beams before focusing.

MATLAB code for the calculation in Fig. 2.2-20 (a) and (b)

```

clc;
clear all;
clear all figure;
%%%%%%%%% Define scale and parameters
x=[-30:0.01:30]
w0=22/2
w00=2
w1=22
%%%%%%%%% Ideal beam plot Fig. 2.2-20 (a)
f=exp(-(2*(x.^2)/w0^2))
f1=1.145*(exp(-(2*x.^2)/w0^2))-0.8*(exp(-(2*x.^2)/w00^2))
f2=rectpuls(x,w1)
figure(3)
plot(x,f,x,f1,x,f2,'linewidth',3.5)
set(gca, 'linewidth',3)
set(gca, 'fontsize',28)
xlabel('Position (mm)','fontsize',28)
xlim([-30 30])
ylabel('Intensity (arb.units)','fontsize',28)
%legend('Gaussian beam','Doughnut beam','Flat-top beam')
legend('boxoff')
*****

```

%%%%%%%% Peak intensity normalized to Gaussian beam peak intensity Fig. 2.2-20
 (b)%%%%%%%%%

```

    f1=exp(-(2*(x.^2)/w0^2))
    f11=1.145*(exp(-(2*x.^2)/w0^2))-0.8*(exp(-(2*x.^2)/w00^2))
    f22=0.5*rectpuls(x,w1)
    figure(4)
    plot(x,f1,x,f11,x,f22,'linewidth',3.5)
    set(gca, 'linewidth',3)
    set(gca, 'fontsize',28)
    xlabel('Position (mm)','fontsize',24)
    xlim([-30 30])
    ylabel('Intensity (arb.unit)','fontsize',24)
    %legend('Gaussian beam','Doughnut beam','Flat-top beam')
    legend('boxoff')
  
```

APPENDIX 2.III. Comparison of various laser beams after focusing.

MATLAB code for the calculation in Fig. 2.2-21.

%%%%%%%% Different M^2 and peak intensity normalized to gaussian beam peak intensity
 - Fig. 2.2-21(a) %%%%%%%%%

```

clc;
clear all;
clear all figure;
%%%%%%%% Define scale and parameters
x=[-150:0.01:150]
P = 1 ; %Power
d=23.3 %pot diameter at focus spot; D=22 mm, m2=1
w0= (d/4)
w1=d/50
IG= P/(pi*(d/2)^2) %Peak intensity
f=IG/IG(max)*(exp(-(x.^2)/(2*w0^2))) % Function for Gaussian beam
P = 1 ; %Power
  
```

```

d1=70 %spot diameter at focus spot" D=22 mm, m2=3
w1= (d1/4)
w2=d1/100
ID= P/(pi*(d1/2)^2) %Peak intensity
f1=ID/IG(max)*((exp(-(x.^2)/(2*w1^2)))- 0.5*(exp(-(x.^2)/(2*w2^2)))) %
Function for doughnut beam
P = 1 ; %Power
d2=116 ;%diameter at focus spot D=22 mm, M2=5
wf=d2/2;
omega=pi/wf
IF= P/(pi*(d2/2)^2) %Peak intensity
f2=IF/IG(max)*(sin(omega.*x))./(omega.*x) % Function for flat-top beam
figure(5)
plot(x,f,x,f1,x,f2,'linewidth',2.5)
set(gca, 'linewidth',3)
set(gca, 'fontsize',28)
xlabel('Position (\mum)','fontsize',28)
xlim([-150 150])
ylabel('Intensity (arb.unit)','fontsize',28)
legend('M^2 = 1','M^2 = 3','M^2 = 5')
legend('boxoff')

*****

%%%%%%%%% Different M2 and peak intensities normalized to 1 - Fig. 2.2-21 (b)
%%%%%%%%%

clc;
clear all;
clear all figure;
%%%%%%%%% Define scale and parameters
x=[-150:0.01:150]
P = 1 ; %Power
d=23.3 %pot diameter at focus spot; D=22 mm, m2=1
w0= (d/4)

```

```

w1=d/50
IG= P/(pi*(d/2)^2) %Peak intensity
f=IG/IG*(exp(-(x.^2)/(2*w0^2))) % Function for Gaussian beam
P = 1 ; %Power
d1=70 %spot diameter at focus spot" D=22 mm, m2=3
w1= (d1/4)
w2=d1/100
ID= P/(pi*(d1/2)^2) %Peak intensity
f1=ID/ID*((exp(-(x.^2)/(2*w1^2)))- 0.5*(exp(-(x.^2)/(2*w2^2)))) % Function
for doughnut beam
P = 1 ; %Power
d2=116 ;%diameter at focus spot D=22 mm, M2=5
wf=d2/2;
omega=pi/wf
IF= P/(pi*(d2/2)^2) %Peak intensity
f2=IF/IF*(sin(omega.*x))./(omega.*x) % Function for flat-top beam
figure(5)
plot(x,f,x,f1,x,f2,'linewidth',2.5)
set(gca, 'linewidth',3)
set(gca, 'fontsize',28)
xlabel('Position (\mum)','fontsize',28)
xlim([-150 150])
ylabel('Intensity (arb.units)','fontsize',28)
legend('M^2 = 1','M^2 = 3','M^2 = 5')
legend('boxoff')
*****
%%%%Same M2 of 5 and peak intensities normalized to 1-Fig. 2.2-21(c)
%%%%
clc;
clear all;
clear all figure;
%%%% Define scale and parameters
x=[-150:0.01:150]

```

```

d1=116 %pot diameter at focus spot; D=22 mm, m2=5
w00= (d1/4)
w11=d1/50
f1=(exp(-(x.^2)/(2*w00^2))) % Function for Gaussian beam
d11=116 %spot diameter at focus spot" D=22 mm, m2=5
w11= (d11/4)
w22=d11/100
f11=((exp(-(x.^2)/(2*w11^2)))- 0.5*(exp(-(x.^2)/(2*w22^2)))) % Function for
doughnut beam
d22=116 ;%diameter at focus spot D=22 mm, M2=5
wf1=d22/2;
omega1=pi/wf1
f22=(sin(omega1.*x))./(omega1.*x) % Function for flat-top beam
figure(6)
plot(x,f1,x,f11,x,f22,'linewidth',2.5)
set(gca, 'linewidth',3)
set(gca, 'fontsize',28)
xlabel('Position (\mum)','fontsize',28)
xlim([-150 150])
ylabel('Intensity (arb.units)','fontsize',28)
legend('M^2 = 5','M^2 = 5','M^2 = 5')
legend('boxoff')

```

```

*****

```

CHAPTER 3

Methodology

CHAPTER 3

Methodology

3.1 Introduction

In this thesis, glass drilling by a short-pulse CO₂ laser with tunable laser parameters was investigated. This chapter describes the laser device properties such as a discharge tube, a high-voltage pulsed-power-supply system and a gas supply system. The laser parameters such as a laser pulse waveform, a laser beam profile, a spot diameter, a fluence per single pulse and a total irradiation fluence. The sample glass properties such as a thermal expansion coefficient, a melting point and a thickness. The result analysis methodologies such as cracks or cracks-free hole, a hole shape, a surface hole diameter, a ratio of a surface hole diameter to an irradiation diameter, a surface HAZ diameter, a ratio of a surface HAZ diameter to an irradiation diameter, a hole depth, a hole volume, a drilling efficiency, a taper angle of a conical hole, an aspect ratio of a cylindrical hole, a ratio of a waist diameter to an surface hole diameter of a biconical hole and a ratio of a waist depth to a hole depth of a biconical hole.

3.2 Laser device

3.2.1 Longitudinally excited CO₂ laser

Fig. 3.2-1 shows a schematic set-up of a longitudinally excited CO₂ laser. Fig. 3.2-2 shows the photograph of the longitudinally excited CO₂ laser with various components such as a discharge tube, an optical cavity, an electrode and a gas supply connection. The discharge tube was made of an alumina ceramic pipe with an inner diameter of 13 mm, an outer diameter of 17 mm and a length of 45 cm and two metallic electrodes attached to both ends of the pipe. The optical cavity was formed by a flat ZnSe output coupler with a reflectivity of 85% at a wavelength of 10.6 μm and an Au-coated high reflective-mirror with a radius of curvature of 20 m and a reflectivity of 99% at a wavelength of 10.6 μm. Therefore, in this experimental set-up, the wavelength was assumed to be 10.6 μm. The optical cavity length was adjustable. The discharge

tube was connected with a high-voltage pulsed-power-supply system and a gas supply system.

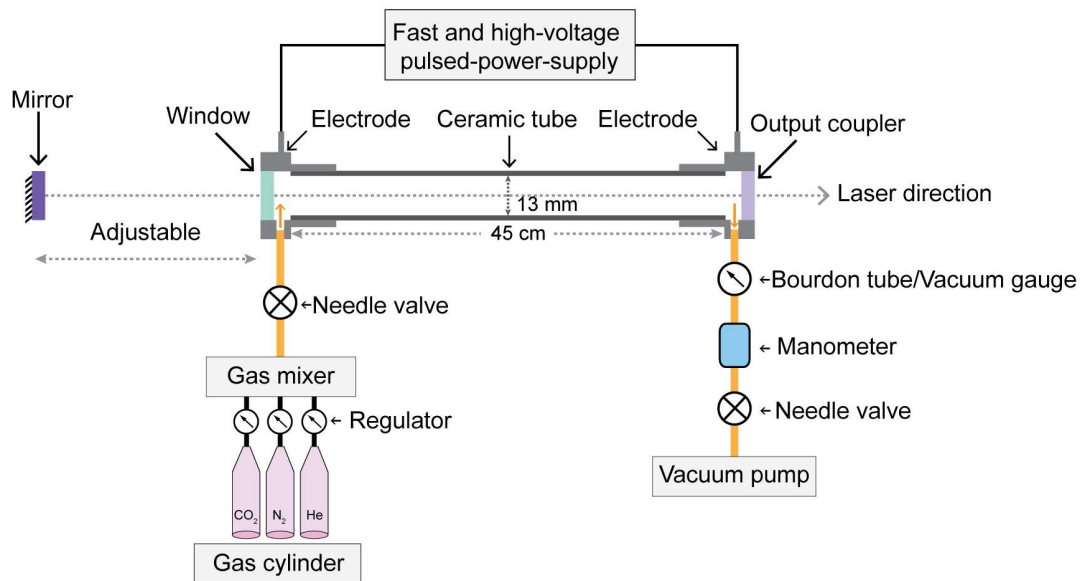


Fig. 3.2-1 Schematic set-up of the longitudinally excited CO₂ laser.

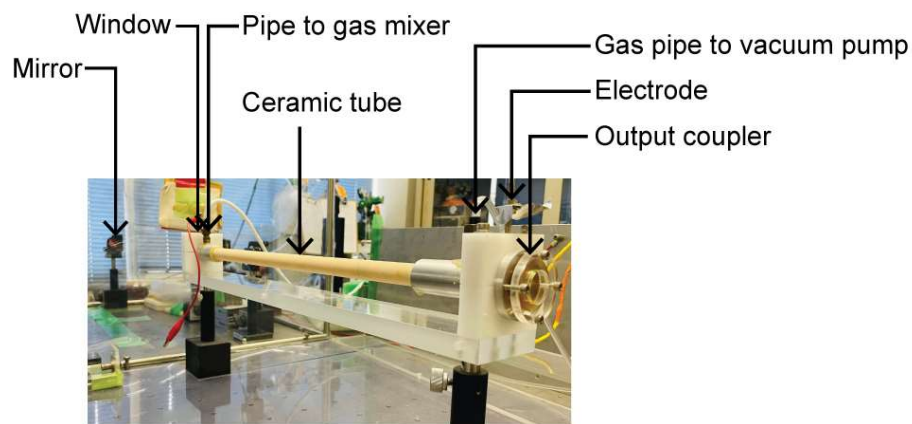


Fig. 3.2-2 Photograph of the longitudinally excited CO₂ laser with various components.

3.2.2 High-voltage pulsed-power-supply system

Fig. 3.2-3 shows the block diagram of the high-voltage pulsed-power-supply system. The power supply system had three modules. The first module was a DC power supply (Takasago, ZX-S-800HA). The second module was a function generator (Agilent, 33220A) to control the repetition rate and the number of laser pulses. The third module that is the main unit was a fast-and-high-voltage generation circuit

(Seidensha Electronics Co., LTD). The high-voltage pulsed-power-supply system produced a high voltage pulse from 15.0 kV to 35.0 kV at a rise time of 200 ns to 800 ns with an input energy to discharge tube of 123 mJ to 736 mJ at a repetition rate of 1 Hz to 400 Hz. The voltage was measured by a high voltage probe (Tektronix, P6015A) and an oscilloscope (Teledyne LeCroy, wavesurfer 10M). The input energy to the discharge tube can be controlled by adjusting the high-voltage pulsed-power-supply system. However, if the input energy changes, the breakdown voltage may change, and the laser pulse waveform may also change. Using an attenuator is a way to change the laser energy without changing the laser pulse waveform.

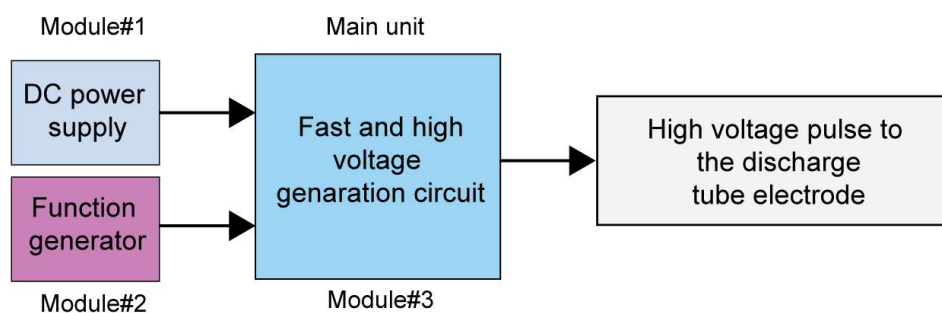


Fig. 3.2-3 Block diagram of the high-voltage pulsed-power-supply system.

3.2.3 Gas supply system

A gas supply system with three gas cylinders, three regulators (Yutaka Crown, FR-IIS-0P), a gas mixture (Fronto, LogMix), two needle valves (Fujikin, DUE-12), a manometer (Okanoworks, U-200), a vacuum gauge (Naganokeiki, 1423602) and a vacuum pump (ULVAC, G-50D) maintained a constant flow of CO₂, N₂ and He gases inside the discharge tube at a distinct gas mixing ratio, a gas pressure and a gas flow rate. A gas mixing ratio was adjusted by the gas mixture. A gas pressure was adjusted by the two needle valves and the manometer. In a longitudinally excited CO₂ laser, by adjusting a gas mixing ratio and/or a gas pressure, various laser pulse waveforms such as a tail-free short pulse, a short pulse with a pulse tail or a long pulse can be produced, but a laser energy also changes [27].

3.3 Laser parameters

3.3.1 Laser pulse waveform

In this thesis, various laser pulses were generated to investigate the influence of laser pulse waveforms on drilling characteristics. Fig. 3.3-1 shows an example of a laser pulse waveform measured by a photon drag detector (Hamamatsu Photonics, B749) and an oscilloscope (Teledyne LeCroy, wavesurfer 10M). The short pulse had a

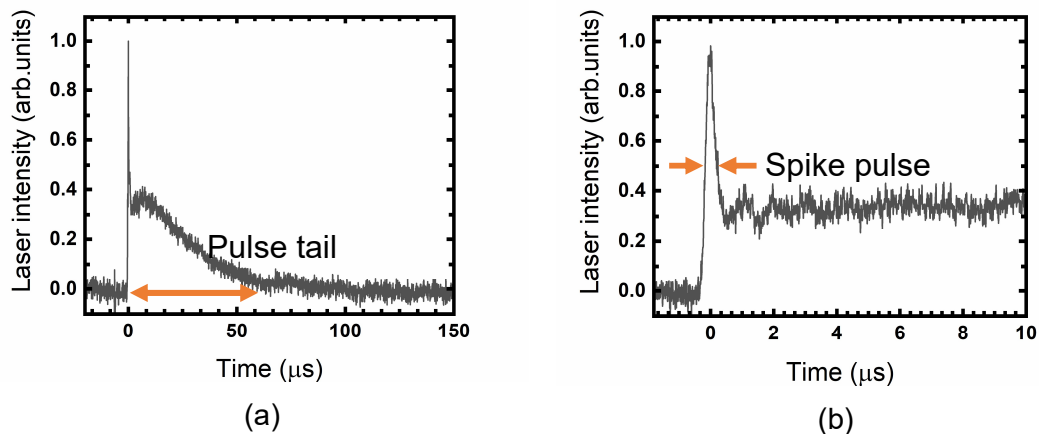


Fig. 3.3-1 Example of a laser pulse waveform. (a) Overall waveform. (b) Magnified timescale of spike pulse.

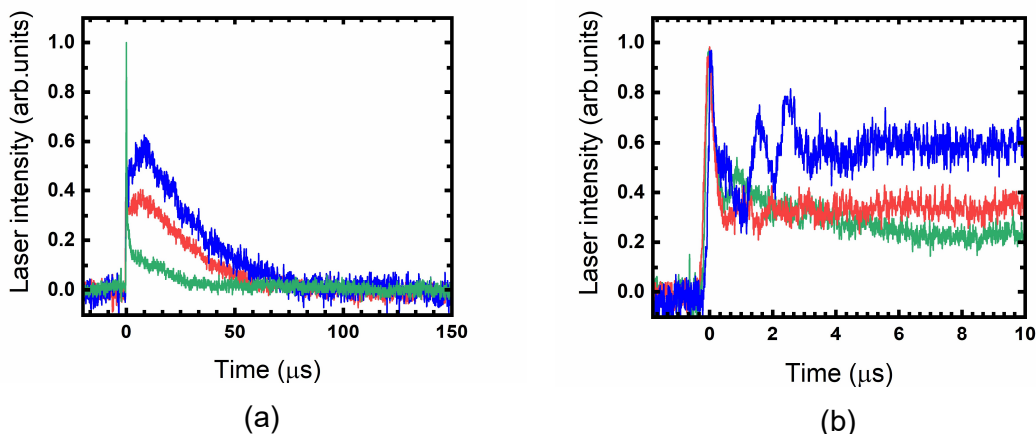


Fig. 3.3-2 Laser pulse waveforms by adjusting a gas medium. Green, red and blue lines represent the laser pulse waveform at an optical cavity length of 125 cm, a gas pressure of 2.0 kPa, 2.4 kPa and 2.6 kPa in a 1:1:2 mixture of CO₂/N₂/He and a repetition rate of 200 Hz. (a) Overall waveform. (b) Magnified timescale of spike pulse.

spike pulse with a width of 280 ns at the full width half maximum (FWHM). The pulse tail length was 86.0 μs . The pulse tail length was defined as the length from the end of the spike pulse to the end of the pulse tail. The energy ratio of the spike pulse to the pulse tail was 1:25. A laser pulse waveform can be controlled by adjusting an excitation circuit and/or a gas medium. In this thesis, a laser pulse waveform was controlled by adjusting a gas medium. Fig. 3.3.2 shows the obtained laser pulse waveforms by adjusting a gas medium at a repetition rate of 200 Hz. For example, a gas pressure of 2.0 kPa, 2.4 kPa and 2.6 kPa in a 1:1:2 mixture of $\text{CO}_2/\text{N}_2/\text{He}$ produced a short pulse with a spike pulse width of 245 ns, 255 ns and 235 ns, a pulse tail length of 43.4 μs , 67.7 μs and 84.8 μs and an energy ratio of the spike pulse to the pulse tail of 1:10, 1:25 and 1:45 at an optical cavity length of 125 cm.

3.3.2 Laser beam profile

The CO_2 laser produced a circular beam. A laser beam profile defines the spatial intensity distribution of a laser beam. The laser beam profile was measured by a knife-edge method where an aperture of $1\text{ mm} \times 1\text{ mm}$ was scanned through the cross section of the laser beam as shown in Fig. 3.3-3. The aperture was 10 cm away from the output coupler. As the aperture moved across the beam, the transmitted energy through the aperture was measured by an energy meter (Gentec, QE50LP-S-MB-D0). By plotting the transmitted energy through the aperture as a function of the position of the aperture, a profile of the beam intensity across the laser beam diameter was obtained. The laser

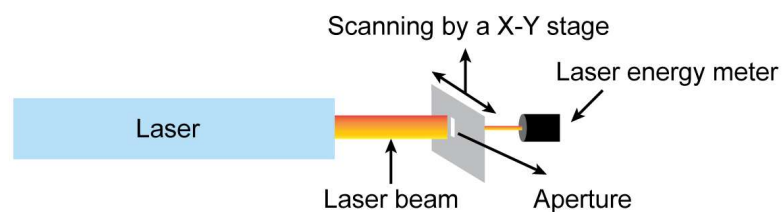


Fig. 3.3-3 Schematic diagram of a knife-edge method.

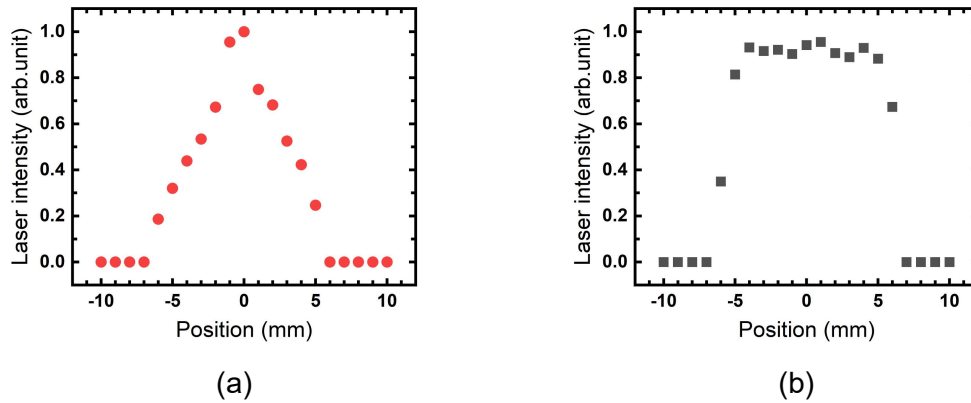


Fig. 3.3-4 Example of a laser beam profile measured by a knife-edge method. The gas pressure was 3.2 kPa in a 1:2 mixture of CO₂/N₂ and a repetition rate was 200 Hz. (a) Central-peak-intensity beam with a beam quality factor M^2 of 7.0 at an optical cavity length of 150 cm. (b) Flat-top beam with a beam quality factor M^2 of 13.5 at an optical cavity length of 60 cm.

beam profile was controlled by placing an aperture at the optical cavity and by adjusting the optical cavity length. For example, at an optical cavity length of 150 cm, a gas pressure of 3.2 kPa in a 1:2 mixture of CO₂/N₂ and a repetition rate of 200 Hz, a central-peak-intensity beam was produced as shown in Fig. 3.3-4 (a) but the shape was not a gaussian. The beam diameter was 12.5 mm and the beam quality factor M^2 was 7.0. At an optical cavity length of 60 cm, a gas pressure of 3.2 kPa in a 1:2 mixture of CO₂/N₂ and a repetition rate of 200 Hz, a flat-top beam as shown in Fig. 3.3-4 (b) was produced. The beam diameter was 12.5 mm and the beam quality factor M^2 was 13.5.

3.3.3 Spot diameter, fluence per single pulse and total irradiation fluence

The spot diameter is the laser beam diameter after focusing by a focusing lens on a sample surface. The spot diameter is the smallest at focal plane of the focusing lens. However, in practical, measuring a spot diameter is a challenging task and requires very precise measurement techniques. In this thesis, the spot diameter was measured by a burn pattern technique. A thermal paper (Edmund optics, ZAP-IT15-526) was the sample. Fig. 3.3-5 (a) shows an example of the spot diameter measured by the burn pattern technique on the focus offsets. In Fig. 3.3-5, 0.00 mm focus offset is the focal plane position, a negative offset is the in-focus position, and a positive offset is the out-focus position.

The fluence is the laser pulse energy per unit irradiation spot area and a fluence per single pulse is the single pulse energy per unit irradiation spot area. A spot area was calculated by the area formula of a circle using the spot diameter measured by a digital microscope (Dino-lite, AM7115MZT). A laser energy was measured by a laser energy meter (Gentec, QE50LP-S-MB-D0). Eq. 3.3-1 presents the expression of a fluence per single pulse. Fig. 3.3-5 (b) shows an example of a fluence per single pulse on a focus offset. The fluence per single pulse was the highest in the focal plane as the spot diameter was the smallest at the focal plane. In the same laser pulse energy, the fluence per single pulse decreased at the in-focus and the out-focus position due to the large spot diameter than that of the focal plane.

$$\text{Fluence per single pulse} = \frac{\text{Laser energy per pulse}}{\text{Irradiation spot area}} \text{ [J/cm}^2\text{]} \quad \text{Eq. 3.3-1}$$

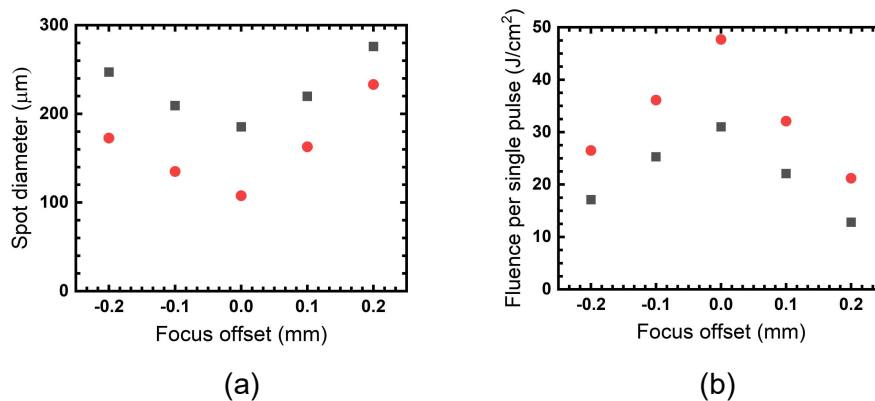


Fig. 3.3-5 Example of a spot diameter and a fluence per single pulse at the various focus offsets of a focusing lens with a focal length of 12.7 mm. 0.00 mm is the focal plane. A negative offset is the in-focus position, and a positive offset is the out-focus position. The gas pressure was 3.2 kPa in a 1:2 mixture of CO₂/N₂ and a repetition rate was 200 Hz. Red color symbol represents a central-peak-intensity beam with a beam quality factor M² of 7.0 at an optical cavity length of 150 cm. Black color symbol represents a flat-top beam with a beam quality factor M² of 13.5 at an optical cavity length of 60 cm. (a) Spot diameter. (b) Fluence per single pulse.

The total irradiation fluence is the product of a fluence per single pulse and a number of pulses is expressed by the Eq. 3.3-2. In this thesis, a percussion drilling method that is a number of pulses were irradiated on the same spot in a sample was used. The position of the focusing lens and the sample was fixed during the percussion drilling as shown in Fig. 3.3-6.

$$\text{Total irradiation fluence} = \text{Number of pulse} \times \text{Fluence per single pulse [J/cm}^2\text{]} \quad \text{Eq. 3.3-2}$$

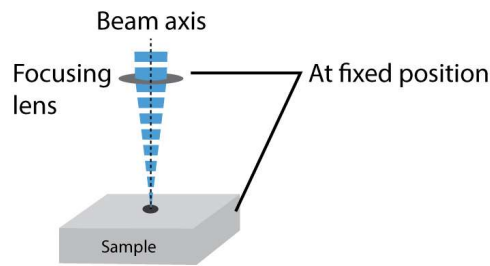


Fig. 3.3-6 Schematic of a percussion drilling method.

3.4 Material properties

In this thesis, a crown glass with a high thermal expansion coefficient of $94 \times 10^{-7} /\text{K}$ and a low melting point of 724°C was used as a sample to realize the microfabrication without an extra treatment by a short-pulse CO_2 laser with tunable laser parameters. Table 3.4-1 shows the basic properties of a crown glass sample.

Table 3.4-1 Basic properties of a crown glass [139,140].

Thermal expansion coefficient	$94 \times 10^{-7} /\text{K}$
Melting point	724°C
Thermal conductivity	1.3 W/mK
Heat capacity	800 J/kgK
Density	2560 kg/m^3
Thickness	$1150 \mu\text{m}$
Manufacturer	Matsunami Glass Ind., Ltd.
Model No.	S-1127

3.5 Result analysis methodologies

In this thesis, a hole with cracks or without cracks, a hole shape, and the drilling characteristics that are the dependence of a hole depth, a hole volume, a drilling efficiency, a surface hole diameter, a ratio of a surface hole diameter to an irradiation diameter, a surface HAZ diameter, a ratio of a surface HAZ diameter to an irradiation diameter, a taper angle of a conical hole, an aspect ratio of a cylindrical hole, a ratio of

a waist diameter to an surface hole diameter of a biconical hole and a ratio of a waist depth to a hole depth of a biconical hole on system parameters, process parameters and material properties were analyzed. Fig. 3.5-1 shows the summary of the considered parameters. The considered system parameters included the focal length of a focusing lens, the focus offset and the numerical aperture. The considered process parameters included the beam profiles, the beam quality factor M^2 , the laser pulse waveform, the energy ratio of the spike pulse part to the pulse tail part, the fluence per single pulse, the total irradiation fluence and the repetition rate. The considered material properties included the thermal expansion coefficient and the melting point. Table 3.5-1 shows the values of the system parameters, the process parameters and the material properties parameters that were used in Sections 4.1, 4.2 and 4.3 in Chapter 4.

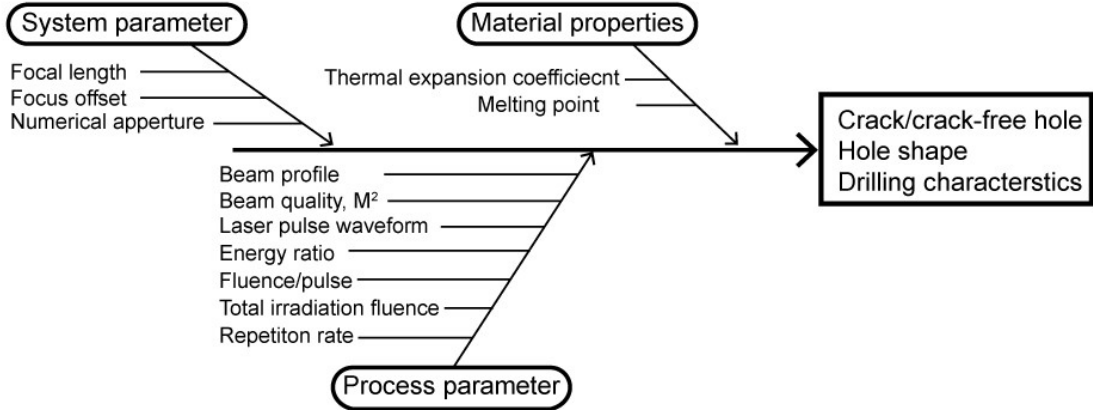


Fig. 3.5-1 Considered system parameters, process parameters and material properties.

Table 3.5-1 Values of the system parameters, the process parameters and the material properties that were used in the chapter 4.

Parameters	Section in chapter 4		
	4.1	4.2	4.3
Wavelength	10.6 μm	10.6 μm	10.6 μm
Beam type	Circular	Circular	Circular
Beam polarization	Random polarization	Random polarization	Random polarization
Beam profile	Doughnut-like and central-peak-intensity with large shoulders	Flat-top	Flat-top and central-peak-intensity
Beam quality, M^2	3.1 to 7.9	13.5	13.5 and 7.0
Focal length	38.1 mm	12.7 mm	12.7 mm
Focus offset	0.00 mm	-0.20 mm to +0.40 mm	-0.20 mm to +0.20 mm
Numerical aperture	0.16	0.49	0.49
Rayleigh length	150 μm	188 μm	188 μm
Laser pulse waveform	Short-pulse with a spike pulse and a pulse tail	Short-pulse with a spike pulse and a pulse tail	Short-pulse with a spike pulse and a pulse tail
Spike pulse width	250 ns	276 ns	276 ns
Pulse tail length	31.4 μs to 134.7 μs	56.9 μs	56.9 μs
Energy ratio	1:7 to 1:92	1:20	1:20
Fluence per single pulse	6.0 J/cm^2 to 37.9 J/cm^2	3.7 J/cm^2 to 46.8 J/cm^2	12.8 J/cm^2 to 47.7 J/cm^2
Total irradiation fluence	238 J/cm^2 to 1305 J/cm^2	110 J/cm^2 to 4209 J/cm^2	383 J/cm^2 to 4296 J/cm^2
Repetition rate	1 Hz to 400 Hz	200 Hz	200 Hz
Thermal expansion coefficient	$94 \times 10^{-7}/\text{K}$	$94 \times 10^{-7}/\text{K}$	$94 \times 10^{-7}/\text{K}$
Melting point	724 $^{\circ}\text{C}$	724 $^{\circ}\text{C}$	724 $^{\circ}\text{C}$
Thickness	1150 μm	1150 μm	1150 μm

3.5.1 Crack and crack-free hole

Cracks and cracks-free hole was identified by a digital microscope (Dino-lite, AM7115MZT). Fig. 3.5-2 (a) shows a sample image of a hole with cracks and Fig. 3.5-2 (b) shows a sample image of cracks-free hole.

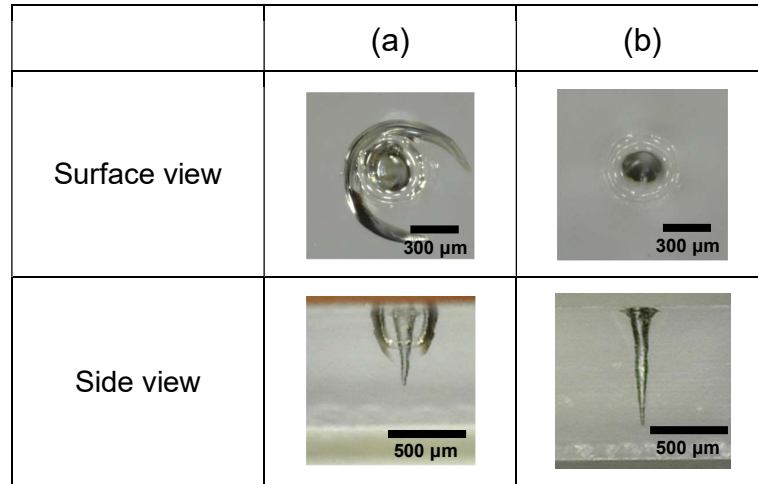


Fig. 3.5-2 Sample hole images. (a) Hole with crack. (b) Crack-free hole.

3.5.2 Shape of hole

In this thesis, the side views of the hole were conical, cylindrical and biconical shape. A conical hole had a larger hole diameter at the surface than at the hole bottom. A cylindrical shape hole had the same hole diameter at the surface and the hole bottom. A biconical shape hole had a larger hole diameter at the surface than at the hole bottom.

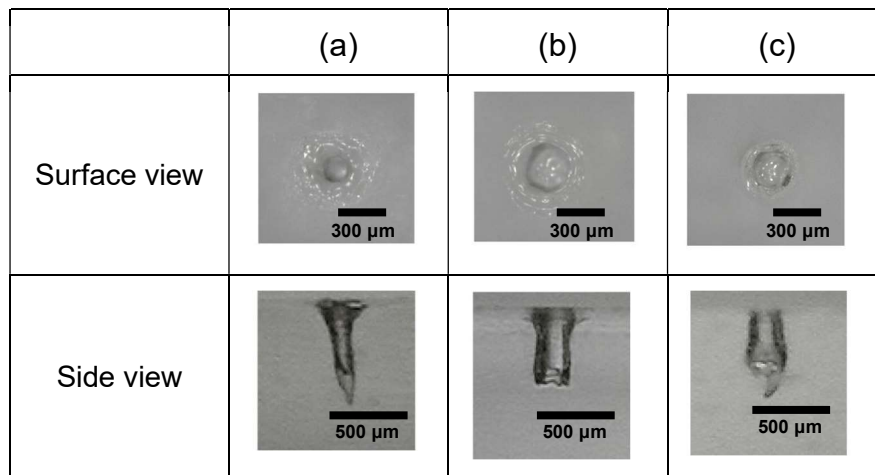


Fig. 3.5-3 Sample hole shape images. (a) Conical hole. (b) Cylindrical hole. (c) Biconical hole.

A biconical hole had a wider waist diameter than the hole diameter at the surface and the hole bottom. Fig. 3.5-3 (a), (b) and (c) shows a sample image of a conical hole, a cylindrical hole and a biconical hole.

3.5.3 Surface hole diameter and ratio of surface hole diameter to irradiation diameter

Fig. 3.5-4 shows an image of a surface hole diameter on the glass surface. Eq. 3.5-1 shows an expression of a ratio of a surface hole diameter to an irradiation diameter.

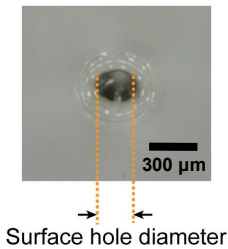


Fig. 3.5-4 Image of a surface hole diameter.

$$\text{Ratio} = \frac{\text{Surface Hole diameter}}{\text{Irradiation diameter}} \qquad \text{Eq. 3.5-1}$$

3.5.4 Surface HAZ diameter and ratio of surface HAZ diameter to irradiation diameter

Fig. 3.5-5 shows an image of a surface HAZ diameter on the glass surface. Eq. 3.5-2 shows an expression of a ratio of a surface HAZ diameter to an irradiation diameter.

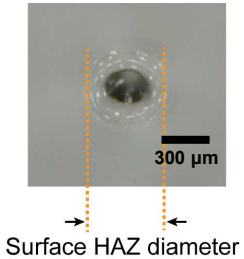


Fig. 3.5-5 Image of a surface HAZ diameter.

$$\text{Ratio} = \frac{\text{Surface HAZ diameter}}{\text{Irradiation diameter}} \quad \text{Eq. 3.5-2}$$

3.5.5 Hole depth and hole volume

Fig. 3.5-6 shows an image of a hole in a glass. The hole depth was measured from the top of the surface to the end of the hole. The hole shape was like a conical shape. To measure the hole volume in the conical hole, the volume formula of a cone was considered and is expressed by the Eq. 3.5-3. Where, h is the hole depth [μm], and r is the radius [μm] of the hole at the surface.

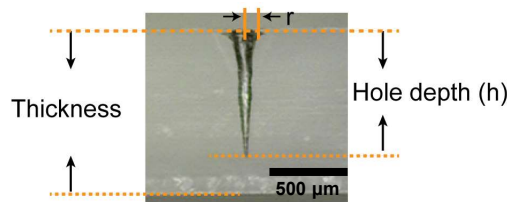


Fig. 3.5-6 Image of a conical hole depth.

$$\text{Hole volume} = \pi r^2 \frac{h}{3} [\mu\text{m}^3] \quad \text{Eq. 3.5-3}$$

3.5.6 Drilling efficiency

The drilling efficiency that is a hole depth per a total irradiation fluence is expressed by the Eq. 3.5-4. The total irradiation fluence is the product of the fluence per single pulse and the number of pulses.

$$\text{Drilling efficiency} = \frac{\text{Hole depth}}{\text{Total irradiation fluence}} [\mu\text{m}/(\text{J}/\text{cm}^2)] \quad \text{Eq. 3.5-4}$$

3.5.7 Taper angle

The taper angle in a conical hole is defined as the angle formed between the side wall of the hole and the axis or the central line of the hole as shown in Fig. 3.5-7. A taper angle of 0 degree correspond to a straight hole with parallel side walls that is a cylindrical hole, while a large taper angle means the hole is more conical. The taper angle is expressed by the Eq. 3.5-5.

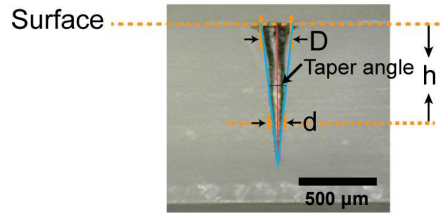


Fig. 3.5-7 Image of a taper angle in a conical hole.

$$\text{Taper angle} = 2 \times \tan^{-1} \frac{D-d}{2h} \times \frac{180}{\pi} \text{ [Degree]} \quad \text{Eq. 3.5-5}$$

Where, D is the diameter [μm] at surface hole, d is the diameter [μm] inside the hole on the side view of the hole, h is the depth [μm] of the hole where the d is measured.

3.5.8 Aspect ratio

The aspect ratio of a cylindrical hole as shown in Fig. 3.5-8 is a dimensionless quantity that represents the ratio of the hole depth to the surface hole diameter and is expressed by the Eq. 3.5-6.

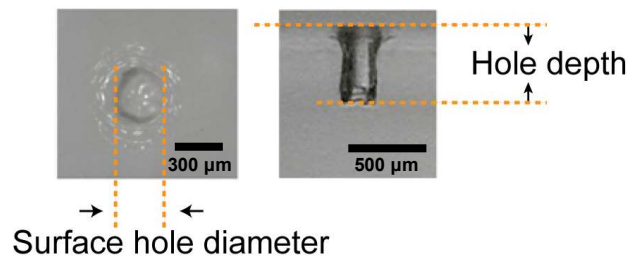


Fig. 3.5-8 Image of a surface hole diameter and hole depth in a cylindrical hole.

3.5.9 Waist diameter and ratio of waist diameter to surface hole diameter

$$\text{Aspect ratio} = \frac{\text{Hole depth}}{\text{Surface hole diameter}} \quad \text{Eq. 3.5-6}$$

The waist diameter is the hole diameter inside the hole at the waist of the biconical hole as shown in Fig. 3.5-9. Eq. 3.5-7 shows an expression of a ratio of a waist diameter to a surface hole diameter.

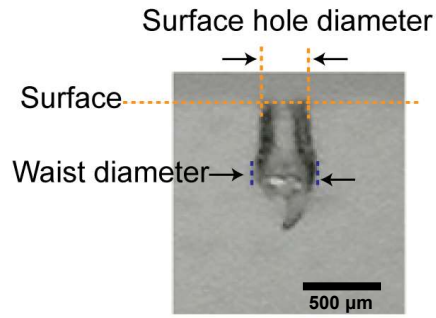


Fig. 3.5-9 Image of a waist diameter and a surface hole diameter.

$$\text{Ratio} = \frac{\text{Waist diameter}}{\text{Surface hole diameter}} \quad \text{Eq. 3.5-7}$$

3.5.10 Waist depth and ratio of waist depth to hole depth

The waist depth of a biconical hole that is the depth of the hole where the hole waist diameter becomes the largest as shown in Fig. 3.5-10. Eq. 3.5-8 shows an expression of a ratio of a waist depth to a hole depth.

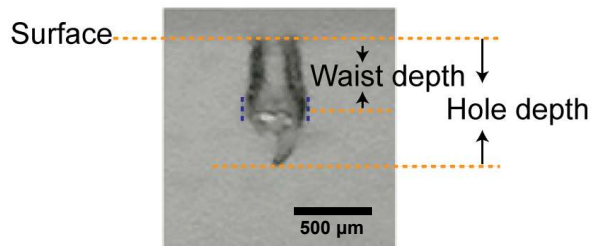


Fig. 3.5-10 Image of a waist depth and a hole depth in a biconical hole.

$$\text{Ratio} = \frac{\text{Waist depth}}{\text{Hole depth}} \quad \text{Eq. 3.5-8}$$

CHAPTER 4

Result and discussions

CHAPTER 4

Result and discussions

4.1 CO₂ laser parameters for crack-free holes in crown glass

4.1.1 Introduction

In this experiment, to investigate the required laser parameters that will produce crack-free holes in a crown glass with a high CTE of 94×10^{-7} /K and a low MP of 724°C without an extra treatment and to investigate the influence of a laser pulse waveform, short laser pulses with a spike pulse width of 250 ns, a pulse tail length of 31.4 μ s to 135 μ s, an energy ratio of a spike pulse to a pulse tail of 1:7.1 to 1:92 and a fluence per single pulse of 6.01 J/cm² to 38.1 J/cm² were irradiated on a sample at a repetition rate of 1 Hz to 400 Hz. The laser beam was a doughnut-like beam with a beam quality factor M² of 3.4 to 7.9 at a repetition rate of 1 Hz to 50 Hz and a central-peak-intensity with large-shoulders beam with a beam quality factor M² of 3.1 to 6.7 at a repetition rate of 50 Hz to 400 Hz. The short laser pulses were irradiated by a focusing lens with a focal length of 38.1 mm at a focus offset of 0.00 mm. The Rayleigh length was 116 μ m to 146 μ m. The short laser pulses produced crack-free holes regardless of the energy of the pulse tail at a repetition rate of 150 Hz to 400 Hz. The drilling characteristics such as the dependence of a hole depth, a hole volume and a drilling efficiency that is a hole depth per a total irradiation fluence, a surface hole diameter, a ratio of a surface hole diameter to an irradiation diameter, a surface HAZ diameter and a ratio of a surface HAZ diameter to an irradiation diameter on a laser pulse waveform, a fluence per single pulse, a total irradiation fluence and a repetition rate were investigated.

4.1.2 Experimental set-up

Fig. 4.1-1 shows the schematic set-up of the processing system using a longitudinally excited CO₂ laser [25–28,30,141]. In this experiment, the laser pulse waveform was controllable at a repetition rate of 1 Hz to 400 Hz. The short-pulse CO₂ laser produced a short pulse with a spike pulse width of about 250 ns, a pulse tail length

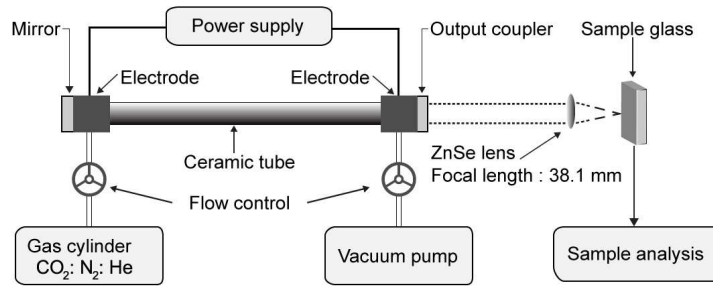


Fig. 4.1-1 Schematic set-up of a laser processing system using a longitudinally excited CO₂ laser.

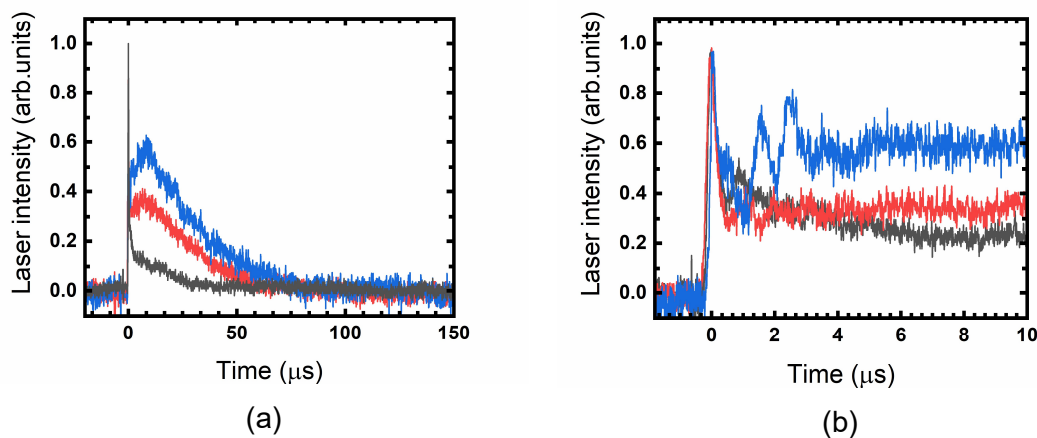


Fig. 4.1-2 Examples of laser pulse waveforms at a repetition rate of 200 Hz. Laser intensity was normalized to the maximum value of the spike pulse. Black, red, and blue lines represent laser pulse waveforms with energy ratios of 1:10, 1:25, and 1:45 respectively. (a) Overall waveform. (b) Magnified timescale of spike pulse.

of 31.4 μs to 135 μs and an energy ratio of a spike pulse to a pulse tail of 1:7.1 to 1:92. Fig. 4.1-2 shows examples of laser pulse waveforms at a repetition rate of 200 Hz. The laser pulse waveform in black line had a spike pulse with a pulse width of 245 ns, a pulse tail with a length of 43.4 μs , and an energy ratio of a spike pulse to a pulse tail of 1:10. The laser pulse waveform in red line had a spike pulse with a pulse width of 255 ns, a pulse tail with a length of 67.7 μs , and an energy ratio of a spike pulse to a pulse tail of 1:25. The laser waveform in blue line had a spike pulse with a pulse width of 235 ns, a pulse tail with a length of 84.8 μs , and an energy ratio of a spike pulse to a pulse tail of 1:45. The laser beam was a doughnut-like beam at a repetition rate of 1 Hz to 50 Hz and a central-peak-intensity with large-shoulders beam at a repetition rate of 50 Hz to 400 Hz. Fig. 4.1-3 (a) shows an example of the doughnut-like beam profile at a

repetition rate of 1 Hz. Fig. 4.1-3 (b) shows an example of the central-peak-intensity with large-shoulders beam profile at a repetition rate of 200 Hz. The beam quality factor M^2 was 3.1 to 7.9 and a beam diameter was 11.5 mm to 13.5 mm at a repetition rate of 1 Hz to 400 Hz. A ZnSe focusing lens with a focal length of 38.1 mm was used to focus the laser beam on the sample surface without changing the focus offset that is at the 0.00 mm focus offset. An NA was 0.15 to 0.18, a DOF was 232 μm to 292 μm and a Rayleigh length was 116 μm to 146 μm . An irradiation diameter was 236 μm to 309 μm . A percussion laser drilling process was used in which multiple laser pulses were radiated at the same spot on the sample. The sample was a crown glass (Matsunami, S1127) with a CTE of $94 \times 10^{-7} / \text{K}$, an MP of 724°C and a thickness of 1150 μm .

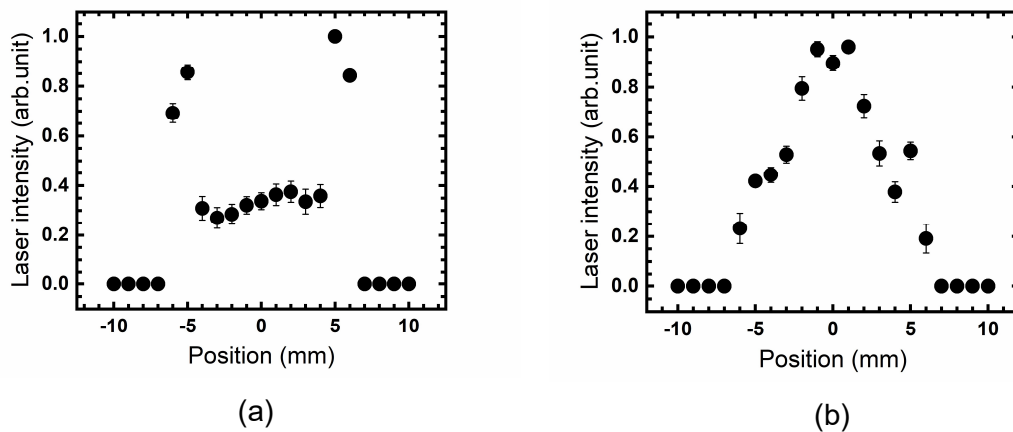


Fig. 4.1-3 Laser beam profiles. (a) Doughnut-like beam. (b) Central-peak-intensity with large shoulders beam.

4.1.3 Results and discussions

4.1.3.1 Investigation of crack-free hole drilling condition

To investigate a crack-free hole drilling in a crown glass without an extra treatment, short laser pulses were irradiated at a repetition rate of 1 Hz to 400 Hz. The following sections will describe the details of the laser pulses and the surface conditions that is crack or crack-free hole.

4.1.3.1.1 Drilling with laser pulses at a repetition rate of 1 Hz

Table 4.1-1 shows the irradiated laser pulses and the surface conditions at a repetition rate of 1 Hz. The short laser pulses had a spike pulse with a pulse width of about 239 ns, a pulse tail with a length of 47.4 μs to 94.2 μs and an energy ratio of a spike pulse to a pulse tail of 1:14 to 1:40. The fluence per single pulse was 6.20 J/cm^2 to 14.0 J/cm^2 . All the laser pulses in Table 4.1-1 produced holes with cracks at a repetition rate of 1 Hz. Fig. 4.1-4 shows an example of a glass surface after irradiating 50 laser pulses with an energy ratio of 1:25 and a fluence per single of 13.9 J/cm^2 at a repetition rate of 1 Hz.

Table 4.1-1 Laser pulses and the surface conditions at a repetition rate of 1 Hz.

Energy ratio	Spike pulse width (ns)	Pulse tail length (μs)	Fluence /pulse (J/cm^2)	No. of pulses	Total irradiation fluence (J/cm^2)	Beam quality: M^2	NA	Spot diameter (μm)	Surface condition
1:14	245	47.4	6.20	50	310	6.11	0.18	260	Crack
1:16	280	58.0	8.60	50	430	4.53	0.18	226	Crack
1:22	255	50.2	7.12	50	356	5.33	0.18	344	Crack
1:25	215	67.1	13.9	50	695	7.28	0.18	316	Crack
1:33	260	76.7	11.4	50	570	6.62	0.18	331	Crack
1:33	210	76.5	11.8	50	590	7.89	0.18	336	Crack
1:40	210	94.2	14.0	50	700	7.63	0.18	323	Crack

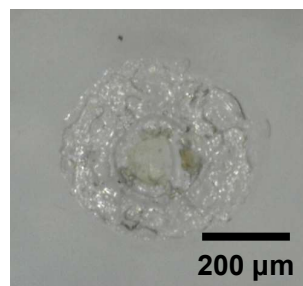


Fig. 4.1-4 Image of a glass surface with cracks after irradiation of 50 laser pulses with an energy ratio of 1:25 and a fluence per single of 13.9 J/cm^2 at a repetition rate of 1 Hz.

4.1.3.1.2 Drilling with laser pulses at a repetition rate of 50 Hz

Table 4.1-2 shows the irradiated laser pulses and the surface conditions at a repetition rate of 50 Hz. The short laser pulses had a spike pulse with a pulse width of about 238 ns, a pulse tail with a length of 61.7 μs to 98.7 μs and an energy ratio of a

spike pulse to a pulse tail of 1:16 to 1:60. The fluence per single pulse was 7.41 J/cm² to 14.3 J/cm². All the laser pulses in Table 4.1-2 produced holes with cracks at a repetition rate of 50 Hz. Fig. 4.1-5 shows an example of a glass surface after irradiating 50 laser pulses with an energy ratio of 1:35 and a fluence per single of 14.3 J/cm² at a repetition rate of 50 Hz.

Table 4.1-2 Laser pulses and the surface conditions at a repetition rate of 50 Hz.

Energy ratio	Spike pulse width (ns)	Pulse tail length (μs)	Fluence /pulse (J/cm ²)	No. of pulses	Total irradiation fluence (J/cm ²)	Beam quality: M ²	NA	Spot diameter (μm)	Surface condition
1:16	315	45.2	7.41	50	370	3.42	0.17	219	Crack
1:23	245	38.6	13.3	50	665	7.29	0.17	311	Crack
1:35	235	61.7	14.3	50	715	7.01	0.17	311	Crack
1:48	240	78.3	7.71	50	385	6.46	0.17	328	Crack
1:55	200	98.1	10.6	50	530	6.46	0.17	331	Crack
1:56	200	98.7	13.0	50	650	7.26	0.17	315	Crack
1:60	235	105	14.3	50	715	3.42	0.17	219	Crack

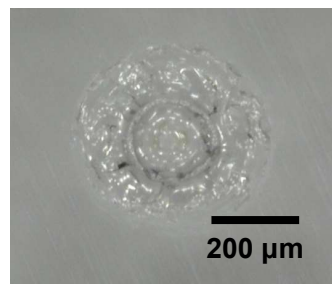


Fig. 4.1-5 Image of a glass surface with cracks after irradiation of 50 laser pulses with an energy ratio of 1:35 and a fluence per single of 14.3 J/cm² at a repetition rate of 50 Hz.

4.1.3.1.3 Drilling with laser pulses at a repetition rate of 100 Hz

Table 4.1-3 shows the irradiated laser pulses and the surface conditions at a repetition rate of 100 Hz. The short laser pulses had a spike pulse with a pulse width of about 241 ns, a pulse tail with a length of 64.4 μs to 110 μs and an energy ratio of a spike pulse to a pulse tail of 1:27 to 1:70. The fluence per single pulse was 8.8 J/cm² to 22 J/cm². Laser pulses in Table 4.1-3 produced holes with cracks and holes without cracks at a repetition rate of 100 Hz. Fig. 4.1-6 shows an example of a glass surface

after irradiating 50 laser pulses with an energy ratio of 1:30 and 1:70, and a fluence per single pulse of 8.81 J/cm² and 22.1 J/cm² at a repetition rate of 100 Hz.

Table 4.1-3 Laser pulses and the surface conditions at a repetition rate of 100 Hz.

Energy ratio	Spike pulse width (ns)	Pulse tail length (μs)	Fluence /pulse (J/cm ²)	No. of pulses	Total irradiation fluence (J/cm ²)	Beam quality: M ²	NA	Spot diameter (μm)	Surface condition
1:27	250	78.3	8.81	50	440	3.44	0.18	204	Crack
1:30	245	88.7	8.81	50	440	5.55	0.18	321	Crack
1:44	235	64.4	21.8	50	1090	4.53	0.18	252	Crack-free
1:50	250	92.2	12.1	50	605	5.70	0.18	313	Crack
1:64	240	110	18.9	50	945	5.37	0.18	293	Crack
1:70	230	110	22.1	50	1105	6.47	0.18	260	Crack-free

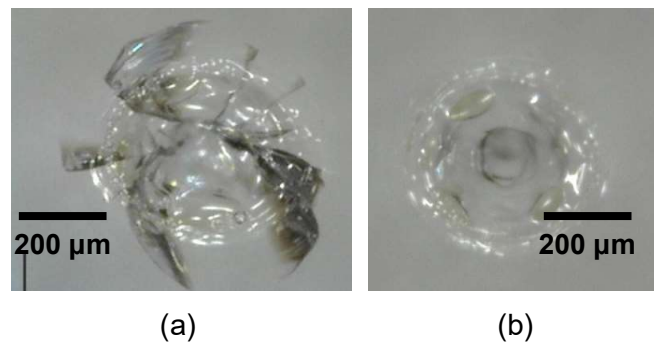


Fig. 4.1-6 Image of a glass surface with cracks and without cracks at a repetition rate of 100 Hz. (a) Hole with cracks after irradiation of 50 laser pulses with an energy ratio of 1:30 and a fluence per single of 8.81 J/cm². (b) Hole without cracks after irradiation of 50 laser pulses with an energy ratio of 1:70 and a fluence per single of 22.1 J/cm².

4.1.3.1.4 Drilling with laser pulses at a repetition rate of 150 Hz

Table 4.1-4 shows the irradiated laser pulses and the surface conditions at a repetition rate of 150 Hz. The short laser pulses had a spike pulse with a pulse width of about 244 ns, a pulse tail with a length of 38.4 μs to 91.6 μs and an energy ratio of a spike pulse to a pulse tail of 1:15 to 1:57. The fluence per single pulse was 8.91 J/cm² to 25.2 J/cm². All the laser pulses in Table 4.1-4 produced holes without cracks at a repetition rate of 150 Hz. Fig. 4.1-7 shows an example of a glass surface after irradiating 50 laser pulses with an energy ratio of 1:25 and a fluence per single of 12.0 J/cm² at a repetition rate of 150 Hz.

Table 4.1-4 Laser pulses and the surface conditions at a repetition rate of 150 Hz.

Energy ratio	Spike pulse width (ns)	Pulse tail length (μ s)	Fluence /pulse (J/cm^2)	No. of pulses	Total irradiation fluence (J/cm^2)	Beam quality: M^2	NA	Spot diameter (μ m)	Surface condition
1:15	230	38	8.91	50	445	6.72	0.16	311	Crack-free
1:25	265	78	12.0	50	600	4.95	0.16	286	Crack-free
1:33	251	86	18.0	50	900	3.91	0.16	289	Crack-free
1:41	235	78	23.0	50	1150	5.79	0.16	278	Crack-free
1:57	240	91	25.2	50	1260	5.79	0.16	278	Crack-free

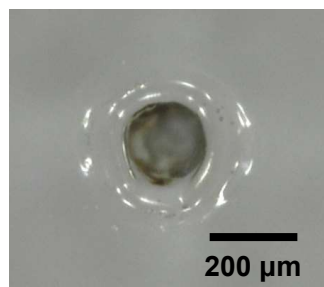


Fig. 4.1-7 Image of a glass surface without cracks after irradiation of 50 laser pulses with an energy ratio of 1:25 and a fluence per single of $12.0 J/cm^2$ at a repetition rate of 150 Hz.

4.1.3.1.5 Drilling with laser pulses at a repetition rate of 200 Hz

Table 4.1-5 shows the irradiated laser pulses and the surface conditions at a repetition rate of 200 Hz. The short laser pulses had a spike pulse with a pulse width of about 243 ns, a pulse tail with a length of 38.1μ s to 135μ s and an energy ratio of a spike pulse to a pulse tail of 1:7.1 to 1:92. The fluence per single pulse was 10.1 to $38.0 J/cm^2$. All the laser pulses in Table 4.1-5 produced crack-free holes at a repetition rate of 200 Hz. Fig. 4.1-8 shows an example of a glass surface after irradiating 50 laser pulses with an energy ratio of 1:18 and a fluence per single of $33.1 J/cm^2$ at a repetition rate of 200 Hz.

Table 4.1-5 Laser pulses and the surface conditions at a repetition rate of 200 Hz.

Energy ratio	Spike pulse width (ns)	Pulse tail length (μ s)	Fluence /pulse (J/cm^2)	No. of pulses	Total irradiation fluence (J/cm^2)	Beam quality: M^2	NA	Spot diameter (μ m)	Surface condition
1:12	270	38.1	10.1	50	505	4.38	0.16	213	Crack-free
1:18	265	43.3	33.1	50	1655	4.15	0.16	241	Crack-free
1:32	245	61.4	36.8	50	1840	5.33	0.16	236	Crack-free
1:38	255	73.1	33.3	50	1665	4.11	0.16	242	Crack-free
1:41	235	83.7	37.9	50	1895	4.21	0.16	239	Crack-free
1:51	235	97.1	28.0	50	1400	3.99	0.16	244	Crack-free
1:92	200	135	34.4	50	1720	3.96	0.16	241	Crack-free

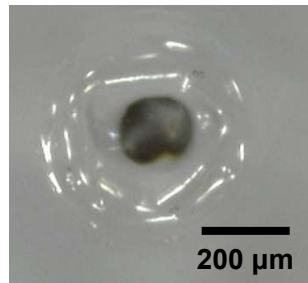


Fig. 4.1-8 Image of a glass surface without cracks after irradiation of 50 laser pulses with an energy ratio of 1:18 and a fluence per single of $33.1 J/cm^2$ at a repetition rate of 200 Hz.

4.1.3.1.6 Drilling with laser pulses at a repetition rate of 400 Hz

Table 4.1-6 shows the irradiated laser pulses and the surface conditions at a repetition rate of 400 Hz. The short laser pulses had a spike pulse with a pulse width of about 278 ns, a pulse tail with a length of 34.1μ s to 55.4μ s and an energy ratio of a spike pulse to a pulse tail was 1:9.2 to 1:25. The fluence per single pulse was 10.7 to $18.4 J/cm^2$. All the laser pulses in Table 4.1-6 produced crack-free holes at a repetition rate of 400 Hz. Fig. 4.1-9 shows an example of a glass surface after irradiating 50 laser pulses with an energy ratio of 1:25 and a fluence per single of $16.9 J/cm^2$ at a repetition rate of 400 Hz.

Table 4.1-6 Laser pulses and the surface conditions at a repetition rate of 400 Hz.

Energy ratio	Spike pulse width (ns)	Pulse tail length (μ s)	Fluence /pulse (J/cm^2)	No. of pulses	Total irradiation fluence (J/cm^2)	Beam quality: M^2	NA	Spot diameter (μ m)	Surface condition
1:9.1	260	34.1	18.4	50	920	4.11	0.16	242	Crack-free
1:9.2	275	41.8	17.4	50	870	4.25	0.16	249	Crack-free
1:11	285	36.4	10.7	50	535	3.46	0.16	221	Crack-free
1:14	278	34.1	13.1	50	655	4.37	0.16	242	Crack-free
1:25	295	55.4	16.9	50	845	4.68	0.16	241	Crack-free

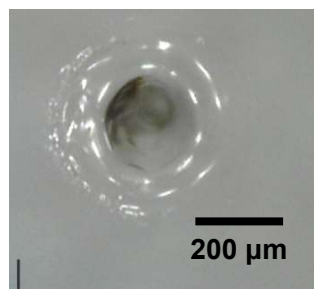
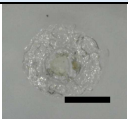
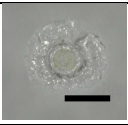
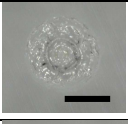
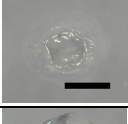
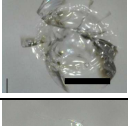
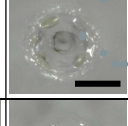
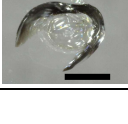
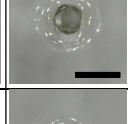
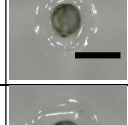
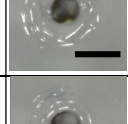
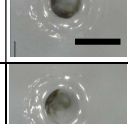
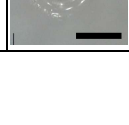


Fig. 4.1-9 Image of a glass surface without cracks after irradiation of 50 laser pulses with an energy ratio of 1:25 and a fluence per single of $16.9 J/cm^2$ at a repetition rate of 400 Hz.

4.1.3.1.7 Summary of crack and crack-free condition

Table 4.1-7 shows the summary of the crack and crack-free conditions with the laser pulses with an energy ratio of 1:7.1 to 1:92 and a fluence per single pulse of $6.01 J/cm^2$ to $37.9 J/cm^2$ at a repetition rate of 1 Hz to 400 Hz. At a repetition rate of 1 Hz to 90 Hz, laser pulses did not produce crack-free holes on the crown glass surface. At a repetition rate of 100 Hz to 140 Hz, laser pulses produced crack and crack-free holes. At a repetition rate of 150 Hz to 400 Hz, laser pulses produced crack-free holes. The crack and crack-free condition may depend on the storage heat generated by each laser pulse. At a small repetition rate, the generated heat dissipates or relaxes before the next pulse irradiation. At a high repetition rate, the generated heat does not dissipate and increases the storage heat and helps to produce crack-free holes.

Table 4.1-7 Presence and absence of cracks in the crown glass depending on the CO₂ laser parameters. The number of pulses was 50. The length of the scale bar is 200 μm in all images.

Rept. rate (Hz)	Energy ratio	Fluence/pulse (J/cm ²)	Beam Quality: M ²	Avg. Spot diameter (μm)	Avg. NA	Crack or Crack-free	Image of a hole with crack	Image of cracks-free hole
1	1:14 - 1:40	6.21 - 14.0	4.5 - 7.9	309	0.18	Crack		×
10	1:12 - 1:57	6.01 - 17.1	4.9 - 7.1	288	0.17	Crack		×
50	1:16 - 1:60	7.44 - 14.3	3.4 - 7.3	308	0.17	Crack		×
90	1:14 - 1:51	7.47 - 14.5	4.6 - 6.7	299	0.17	Crack		×
100	1:27 - 1:70	8.81 - 22.1	3.4 - 6.5	282	0.18	Both		
140	1:12 - 1:65	7.33 - 22.9	4.5 - 6.3	288	0.17	Both		
150	1:15 - 1:57	8.90 - 25.2	4.8 - 6.7	288	0.17	Crack-free	×	
200	1:7 - 1:92	10.1 - 37.9	4.0 - 5.3	236	0.16	Crack-free	×	
300	1:12 - 1:44	17.4 - 28.9	3.1 - 4.7	236	0.16	Crack-free	×	
400	1:9 - 1:25	10.7 - 18.4	3.5 - 4.7	240	0.16	Crack-free	×	

4.1.3.2 Investigation of the dependence of drilling characteristics on laser parameters

Fig. 4.1-10 shows a top and side view of the crown glass sample irradiated by 30 pulses of the CO₂ laser short pulse with a spike pulse width of 255 ns, a pulse tail length of 75.6 μs, an energy ratio of the spike pulse to the pulse tail of 1:25, a fluence per single pulse of 34.1 J/cm², a total irradiation fluence of 1023 J/cm², an irradiation diameter of 250 μm and a repetition rate of 200 Hz. The drilled hole did not have any cracks. The surface hole diameter was 122 μm and was 0.48 times the irradiation diameter. The surface HAZ diameter of the sample surface was 362 μm and was 1.51 times the irradiation diameter. The hole depth was 923 μm, and the estimated hole volume was about $3.61 \times 10^6 \mu\text{m}^3$.

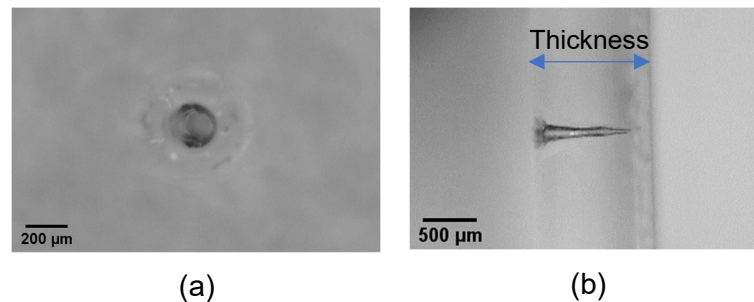


Fig. 4.1-10 Top and side views of the crown glass sample irradiated by 30 pulses of the CO₂ laser short pulse with an energy ratio of 1:25, a fluence per single pulse of 34.1 J/cm², a total irradiation fluence of 1023 J/cm² and a repetition rate of 200 Hz. (a) Top view. (b) Side view.

4.1.3.2.1 Hole depth, hole volume and drilling efficiency

Fig. 4.1-11 shows the dependence of a hole depth and an estimated hole volume on a laser pulse waveform, a fluence per single pulse and a total irradiation fluence at a repetition rate of 200 Hz. The hole depth and the estimated hole volume increased with the increase of the total irradiation fluence which is a natural phenomenon of laser drilling. Table 4.1-8 is the slopes of Fig. 4.1-11 shows the drilling efficiency that is a hole depth per the total irradiation fluence and an estimated hole volume per the total irradiation fluence. At the same fluence per single pulse the drilling efficiency was high in a laser pulse waveform with a high energy ratio of a spike pulse to a pulse tail. However, in the master's thesis of Yoshihito Baba in 2022 at University of Yamanashi, a short pulse with an energy ratio of 1:7 gave a deeper depth and a higher drilling

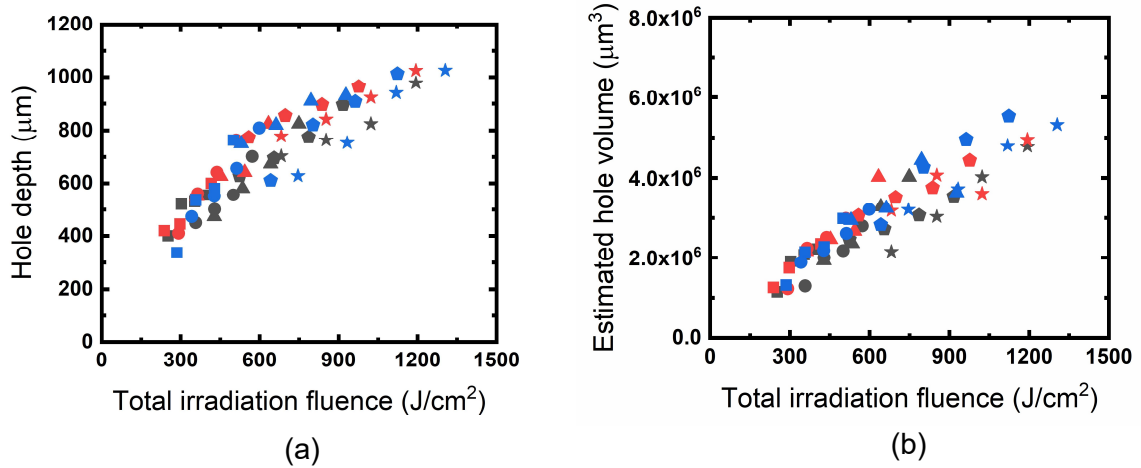


Fig. 4.1-11 Dependence of hole depth and estimated hole volume on laser pulse waveforms, fluence per single pulse and total irradiation fluence at a repetition rate of 200 Hz. (a) Hole depth. (b) Estimated hole volume. Legend is in the Table 4.1-8.

Table 4.1-8 Dependence of a hole depth and an estimated hole volume per a total irradiation fluence on a laser pulse waveform and a fluence per single pulse at a repetition rate of 200 Hz. The hole depth and the estimated hole volume per the total irradiation fluence are the slopes of Fig. 4.1-11 (a) and (b), respectively.

Symb ol in Fig. 4.1-11	Laser pulse wavefor m	Spike pulse width (ns)	Pulse tail length (μs)	Fluence/ pulse (J/cm ²)	Beam quality : M ²	NA	Rayleig h length (μm)	Hole depth/total irradiation fluence (μm/J/cm ²)	Estimated hole volume/total irradiation fluence (μm ³ /J/cm ²)
■	1:7.1	265	38.2	10.1	4.4	0.15	144	1.54	5.55×10^3
●	1:7.1	310	39.7	14.3	4.4	0.15	144	1.19	4.37×10^3
▲	1:10	275	44.3	21.4	4.4	0.15	144	1.07	4.85×10^3
◆	1:10	275	54.1	26.2	4.4	0.15	144	1.06	4.15×10^3
★	1:10	255	45.5	34.1	4.4	0.15	144	0.89	3.66×10^3
■	1:25	275	85.6	11.9	4.2	0.16	125	1.56	5.70×10^3
●	1:25	275	85.6	14.6	4.2	0.16	144	1.48	5.48×10^3
▲	1:23	275	77.4	18.1	4.2	0.16	144	1.35	5.66×10^3
◆	1:25	285	69.2	27.9	4.2	0.16	125	1.17	4.89×10^3
★	1:25	255	75.6	34.1	4.1	0.16	125	0.99	4.33×10^3
■	1:49	235	101	14.3	5.3	0.16	125	1.39	5.46×10^3
●	1:49	235	120	17.1	5.3	0.16	125	1.37	5.27×10^3
▲	1:45	245	95.4	26.5	4.5	0.16	125	1.20	4.99×10^3
◆	1:45	255	111	32.1	4.0	0.16	125	0.95	4.95×10^3
★	1:41	245	95.1	37.3	4.2	0.16	125	0.82	4.16×10^3

efficiency than a short pulse with an energy ratio of 1:31 at the same fluence per single pulse of 21.5 J/cm^2 , the total irradiation fluence of 10000 J/cm^2 or less, a repetition rate of 200 Hz and four types of glass that is a crown glass with a CTE of $94 \times 10^{-7} /\text{K}$ and an MP of 724°C , a soda-lime glass with a CTE of $87 \times 10^{-7} /\text{K}$ and an MP of 740°C , a borosilicate glass with a CTE of $33 \times 10^{-7} /\text{K}$ and an MP of 820°C and a synthetic quartz glass with a CTE of $5.5 \times 10^{-7} /\text{K}$ and an MP of 1600°C [138,142]. In experiments by Yoshihito Baba, an attenuator was used to control the fluence per single pulse without changing the laser pulse waveform. In my experiment, because the laser pulse waveform and the fluence per single pulse were not unified and the dependence of the drilling efficiency on the laser pulse waveform and the fluence per single pulse could not describe accurately. Therefore, to get the dependence of drilling efficiency on the laser pulse waveform, more combination of data is required.

On the other hand, a smaller fluence per single pulse tended to give a higher drilling efficiency. The fact can have two possible reasons. One possible reason is, when a laser pulse is irradiated with a small fluence per single pulse, the molten particles flow in small amounts that may have a small shielding effect on next pulses. At a high fluence per single pulse, the molten particle flows in a large amount, which may have a large shielding effect on the subsequent pulses, thereby resulting in a small drilling efficiency. Another possible reason is, the storage heat is high in a small fluence per single pulse and compared to the storage heat in a high fluence per single pulse in a same total irradiation fluence because a small fluence per single pulse has larger number of pulses than a high fluence per single pulse. In other words, irradiation of a large number of pulses in the same total irradiation fluence may have a pre-heating effect. Therefore, the measurement of the spatial-time distribution of the temperature can give the solution to the question. In addition, to get the dependence of the drilling efficiency on the laser pulse waveform and the fluence per single pulse, using an attenuator is effective to control the fluence per single pulse without changing the laser pulse waveform.

Furthermore, repetition rates of 200 Hz, 300 Hz and 400 Hz were considered to realize the dependence of the hole depth and the estimated hole volume per the total irradiation fluence on the repetition rate. Table 4.1-9 shows the dependence of the drilling characteristics on the repetition rates of 200 Hz, 300 Hz and 400 Hz. The hole depth and the estimated hole volume per the total irradiation fluence increased with the

repetition rate. The drilling efficiency was higher at 400 Hz than 300 Hz but slightly lower than 200 Hz at the same fluence per single pulse. A further high repetition rate could be considered to find the high scale differences. Therefore, under the various irradiation conditions, the hole depth and the estimated hole volume per the total irradiation fluence depended on the laser pulse waveform with the energy ratio of a spike pulse to a pulse tail of 1:10 to 1:45, the fluence per single pulse and the repetition rate.

Table 4.1-9 Dependence of a hole depth and an estimated hole volume per a total irradiation fluence of 50 pulses at a repetition rate of 200 Hz, 300 Hz and 400 Hz.

Rept. rate (Hz)	Laser pulse waveform	Spike pulse width (ns)	Pulse tail length (μ s)	Fluence/pulse (J/cm^2)	Beam quality : M^2	NA	Rayleigh length (μ m)	Surface hole diameter (μ m)	Hole depth (μ m)	Hole depth/total irradiation fluence (μ m/ J/cm^2)	Estimated hole volume/total irradiation fluence (μ m ³ / J/cm^2)
200	1:25	255	75.1	14.2	4.4	0.15	144	122	778	1.09	4.32×10^3
200	1:40	235	95.3	16.4	4.4	0.15	144	123	901	1.10	4.35×10^3
200	1:37	245	86.5	18.8	4.4	0.15	144	122	910	0.97	3.82×10^3
200	1:35	245	72.2	19.4	4.2	0.17	125	122	901	0.93	3.67×10^3
300	1:27	280	67.4	14.1	4.0	0.17	125	122	801	1.13	4.43×10^3
300	1:21	250	56.6	16.2	4.3	0.17	125	128	816	1.01	3.95×10^3
300	1:16	225	35.2	18.3	4.0	0.17	124	122	790	0.86	3.37×10^3
300	1:22	205	40.3	19.4	3.8	0.16	129	128	845	0.87	3.75×10^3
400	1:11	267	41.4	14.1	3.5	0.15	145	122	802	1.14	4.44×10^3
400	1:10	265	35.2	16.4	3.5	0.15	145	122	842	1.03	4.01×10^3
400	1:10	265	35.2	18.2	4.4	0.15	145	122	801	0.88	3.44×10^3
400	1:21	310	44.7	19.1	4.7	0.17	125	125	830	0.87	3.51×10^3

4.1.3.2.2 Surface hole diameter and ratio of a surface hole diameter to an irradiation diameter

Fig. 4.1-12 shows the dependence of a surface hole diameter and a ratio of a surface hole diameter to an irradiation diameter on a laser pulse waveform, a fluence per single pulse and a total irradiation fluence at a repetition rate of 200 Hz. Table 4.1-10 shows the legend of the Fig. 4.1-12. The surface hole diameter and the ratio of the surface hole diameter to the irradiation diameter did not depend on the fluence per single pulse and the laser pulse waveform. The surface hole diameter and the ratio of a

surface hole diameter to an irradiation diameter initially increased with the total irradiation fluence until about 750 J/cm^2 , then saturated with the total irradiation fluence. Table 4.1-11 and Table 4.1-12 shows the surface hole diameter and the ratio of a surface hole diameter to an irradiation diameter at a total irradiation fluence of about 500 J/cm^2 and 1000 J/cm^2 , respectively. The average surface hole diameter was $122 \text{ }\mu\text{m}$ and $130 \text{ }\mu\text{m}$, and the average ratio of a surface hole diameter to an irradiation diameter was 0.45 and 0.50 at a total irradiation fluence of about 500 J/cm^2 and 1000 J/cm^2 , respectively. Therefore, under various irradiation conditions, the surface hole diameter and the ratio of a surface hole diameter to an irradiation diameter did not depend on the laser pulse waveform and the fluence per single pulse, and initially may depend on a total irradiation fluence but later saturated. Additionally, the ratio of a surface hole diameter to an irradiation diameter showed that the surface hole diameter was smaller than the irradiation diameter. A small irradiation diameter will give a small surface hole diameter. To produce a small surface hole diameter an investigation using a high-quality gaussian beam and a high NA could be useful. For example, a CO_2 laser with a wavelength of $10.6 \text{ }\mu\text{m}$, a high-quality gaussian beam with a beam quality factor M^2 of 1.0, an f/D of 1.73 with a focal length f of 38.1 mm and a diameter D of 22.0 mm expected to give an irradiation diameter of $23.3 \text{ }\mu\text{m}$, thus a hole diameter of about $10 \text{ }\mu\text{m}$ can be possible to produce by a direct CO_2 laser irradiation.

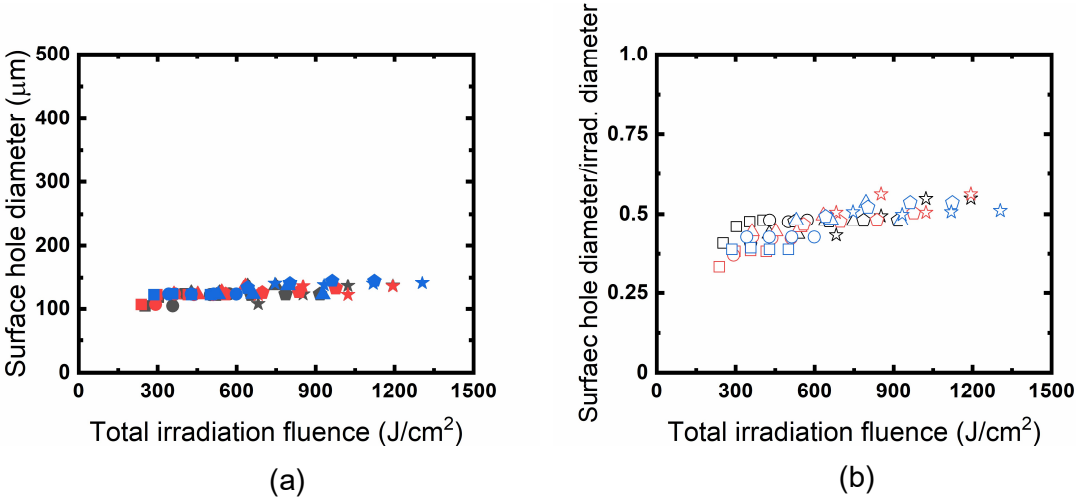


Fig. 4.1-12 Dependence of a surface hole diameter and a ratio of a surface hole diameter to an irradiation diameter on a laser pulse waveform, a fluence per single pulse and a total irradiation fluence at a repetition rate of 200 Hz. (a) Surface hole diameter. (b) Ratio of a surface hole diameter to an irradiation diameter. Legend is in the Table 4.1-10.

Table 4.1-10 Legend of Fig. 4.1-12.

Symbol in Fig. 4.1-12	Laser pulse waveform	Spike pulse width (ns)	Pulse tail length (μs)	Fluence/pulse (J/cm^2)	NA	Rayleigh length (μm)	Irradiation diameter (μm)
■	1:7	265	38.2	10.1	0.15	144	256
●	1:7	310	39.7	14.3	0.15	144	256
▲	1:10	275	44.3	21.4	0.15	144	285
◆	1:10	275	54.1	26.2	0.15	144	255
★	1:10	255	45.5	34.1	0.15	144	250
■	1:25	275	85.6	11.9	0.16	125	319
●	1:25	275	85.6	14.6	0.16	144	288
▲	1:23	275	77.4	18.1	0.16	144	275
◆	1:25	285	69.2	27.9	0.16	125	263
★	1:25	255	75.6	34.1	0.16	125	241
■	1:49	235	101	14.3	0.16	125	314
●	1:49	235	120	17.1	0.16	125	288
▲	1:45	245	95.4	26.5	0.16	125	255
◆	1:45	255	111	32.1	0.16	125	270
★	1:41	245	95.1	37.3	0.16	125	275

Table 4.1-11 The ratio of a surface hole diameter to an irradiation diameter at a total irradiation fluence of $500 \text{ J}/\text{cm}^2$.

Symbol in Fig. 4.1-12	Laser pulse waveform	Spike pulse width (ns)	Pulse tail length (μs)	Fluence/pulse (J/cm^2)	Total irradiation fluence of about $500 \text{ J}/\text{cm}^2$	
					Surface hole diameter (μm)	Ratio of surface hole diameter to irradiation diameter
●	1:7	310	39.7	14.3	123	0.48
◆	1:10	275	54.1	26.2	122	0.47
●	1:25	275	85.6	14.6	122	0.42
◆	1:25	285	69.2	27.9	122	0.46
■	1:49	235	101	14.3	122	0.38
▲	1:45	245	95.4	26.5	123	0.47
					Avg. = 122	Avg. = 0.45

Table 4.1-12 The ratio of a surface hole diameter to an irradiation diameter at a total irradiation fluence of 1000 J/cm².

Symbol in Fig. 4.1-12	Laser pulse waveform	Spike pulse width (ns)	Pulse tail length (μs)	Fluence/pulse (J/cm ²)	Total irradiation fluence of about 1000 J/cm ²	
					Surface hole diameter (μm)	Ratio of surface hole diameter to irradiation diameter
◆	1:10	275	54.1	26.2	122	0.48
★	1:10	255	45.5	34.1	136	0.54
◆	1:25	285	69.2	27.9	132	0.50
★	1:25	255	75.6	34.1	132	0.56
▲	1:45	245	95.4	26.5	122	0.47
◆	1:45	255	111	32.1	139	0.49
					Avg. = 130	Avg. = 0.50

4.1.3.2.3 Surface HAZ diameter and ratio of a surface HAZ diameter to an irradiation diameter

Fig. 4.1-13 shows the dependence of a surface HAZ diameter and a ratio of a surface HAZ diameter to an irradiation diameter on a laser pulse waveform, a fluence per single pulse and a total irradiation fluence at a repetition rate of 200 Hz. The ratio of a surface HAZ diameter to an irradiation diameter did not depend on the laser pulse waveform. For example, at the total irradiation fluence of about 600 J/cm², a laser pulse waveform with an energy ratio of 1:10, 1:25 and 1:45 produced a ratio of a surface HAZ diameter to an irradiation diameter of 1.55, 1.47 and 1.55, respectively, that are almost same. However, in the master's thesis of Yoshihito Baba in 2022 at University of Yamanashi, a short pulse with an energy ratio of 1:7 gave a smaller HAZ than a short pulse with an energy ratio of 1:31 at the same fluence per single pulse of 21.5 J/cm², the total irradiation fluence of 2000 J/cm² to 10000 J/cm², a repetition rate of 200 Hz and two types of glass that is a crown glass with a CTE of 94×10^{-7} /K and an MP of 724°C and a soda-lime glass with a CTE of 87×10^{-7} /K and an MP of 740°C [138,142]. In a borosilicate glass with a CTE of 33×10^{-7} /K and an MP of 820°C and a synthetic quartz glass with a CTE of 5.5×10^{-7} /K and an MP of 1600°C, the short pulse with an energy ratio of 1:7 produced a same HAZ diameter as that of 1:31 [138,142].

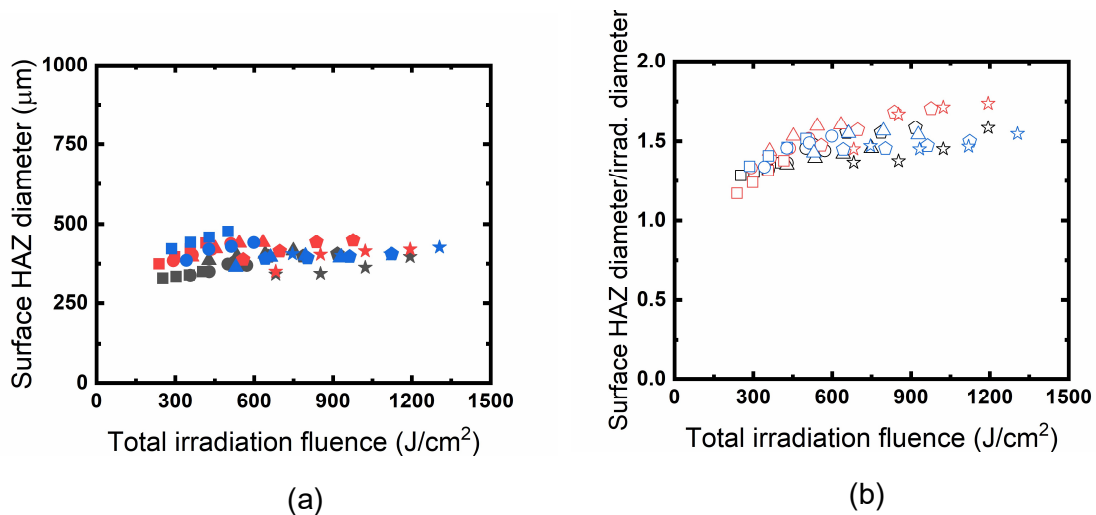


Fig. 4.1-13 Dependence of a surface HAZ diameter and a ratio of a surface HAZ diameter to an irradiation diameter on a laser pulse waveform, a fluence per single pulse and a total irradiation fluence at a repetition rate of 200 Hz. (a) Surface HAZ diameter. (b) Ratio of a surface HAZ diameter to an irradiation diameter. Legend is in the Table 4.1-13.

On the other hand, the ratio of a surface HAZ diameter to an irradiation diameter did not depend on the fluence per single pulse. The ratio of a surface HAZ diameter to an irradiation diameter increased with the total irradiation fluence until the total irradiation fluence of about 600 J/cm² and after that the ratio was saturated. Table 4.1-14 and Table 4.1-15 shows the surface HAZ diameter and the ratio of a surface HAZ diameter to an irradiation diameter at the total irradiation fluence of about 500 J/cm² and 1000 J/cm², respectively. The average surface HAZ diameter and the average ratio of a surface HAZ diameter to an irradiation diameter was 384 μm and 410 μm, and 1.41 and 1.58 at a total irradiation fluence of about 500 J/cm² and 1000 J/cm², respectively. Therefore, a surface HAZ diameter and a ratio of a surface HAZ diameter to an irradiation diameter was high in a high total irradiation fluence. The heat during the processing below the vaporization temperature but higher than the MP gives the HAZ. The HAZ depends on the heat distribution in the laser beam and the laser pulse. The control of the heat distribution is important to reduce the HAZ and that can be achieved by controlling the laser beam profile and the laser pulse.

Table 4.1-13 Legend of Fig. 4.1-13.

Symbol in Fig. 4.1-13	Laser pulse waveform	Spike pulse width (ns)	Pulse tail length (μ s)	Fluence/pulse (J/cm^2)	NA	Rayleigh length (μ m)	Irradiation diameter (μ m)
■	1:7	265	38.2	10.1	0.15	144	256
●	1:7	310	39.7	14.3	0.15	144	256
▲	1:10	275	44.3	21.4	0.15	144	285
◆	1:10	275	54.1	26.2	0.15	144	255
★	1:10	255	45.5	34.1	0.15	144	250
■	1:25	275	85.6	11.9	0.16	125	319
●	1:25	275	85.6	14.6	0.16	144	288
▲	1:23	275	77.4	18.1	0.16	144	275
◆	1:25	285	69.2	27.9	0.16	125	263
★	1:25	255	75.6	34.1	0.16	125	241
■	1:49	235	101	14.3	0.16	125	314
●	1:49	235	120	17.1	0.16	125	288
▲	1:45	245	95.4	26.5	0.16	125	255
◆	1:45	255	111	32.1	0.16	125	270
★	1:41	245	95.1	37.3	0.16	125	275

Table 4.1-14 The ratio of a surface HAZ diameter to an irradiation diameter at a total irradiation fluence of $500 J/cm^2$.

Symbol in Fig. 4.1-13	Laser pulse waveform	Spike pulse width (ns)	Pulse tail length (μ s)	Fluence/pulse (J/cm^2)	Total irradiation fluence of about $500 J/cm^2$	
					Surface HAZ diameter (μ m)	Ratio of surface HAZ diameter to irradiation diameter
●	1:7	310	39.7	14.3	373	1.44
◆	1:10	275	54.1	26.2	380	1.48
●	1:25	275	85.6	14.6	384	1.47
◆	1:25	285	69.2	27.9	387	1.33
■	1:49	235	101	14.3	421	1.34
▲	1:45	245	95.4	26.5	364	1.42
					Avg. = 384	Avg. = 1.41

Table 4.1-15 The ratio of a surface HAZ diameter to an irradiation diameter at a total irradiation fluence of 1000 J/cm².

Symbol in Fig. 4.1-13	Laser pulse waveform	Spike pulse width (ns)	Pulse tail length (μs)	Fluence/pulse (J/cm ²)	Total irradiation fluence of about 1000 J/cm ²	
					Surface HAZ diameter (μm)	Ratio of surface HAZ diameter to irradiation diameter
◆	1:10	275	54.1	26.2	405	1.55
★	1:10	255	45.5	34.1	396	1.58
◆	1:25	285	69.2	27.9	448	1.70
★	1:25	255	75.6	34.1	414	1.71
▲	1:45	245	95.4	26.5	393	1.54
◆	1:45	255	111	32.1	404	1.42
					Avg. = 410	Avg. = 1.58

4.1.4 Summary

In this experiment, short-pulse CO₂ laser drilling in a crown glass with a high CTE of 94×10^{-7} /K and a low MP of 724°C was investigated. The short-pulse CO₂ laser had a spike pulse width of about 250 ns, a pulse tail length of 31.4 μs to 135 μs, an energy ratio of a spike pulse to a pulse tail of 1:7.1 to 1:92, and a fluence per single pulse of 6.01 J/cm² to 37.9 J/cm² at a repetition rate of 1 Hz to 400 Hz. The short-pulse CO₂ laser with a tunable pulse tail operating at a repetition rate of 150 Hz to 400 Hz produced crack-free holes without any kind of cooling system in the processing area. In contrast, cracks were produced at a repetition rate of 90 Hz or less. The ratio of a surface hole diameter to an irradiation diameter did not depend on the laser pulse waveform and the fluence per single pulse, and the ratio was initially increased then was almost the same with the total irradiation fluence. The ratio of a surface HAZ diameter to an irradiation diameter did not depend on the laser pulse waveforms with an energy ratio of a spike pulse to a pulse tail of 1:10 to 1:45 and the fluence per single pulse. The ratio increased with the total irradiation fluence that is a natural phenomenon. The drilling efficiency that is the hole depth and the estimated hole volume per the total irradiation fluence depended on the laser pulse waveform with an energy ratio of a spike pulse to a pulse tail of 1:10 to 1:45, the fluence per single pulse and the repetition rate.

4.2 Cylindrical hole drilling in crown glass by a short-pulse CO₂ laser with a flat-top beam

4.2.1 Introduction

In this experiment, cylindrical hole drilling and the drilling characteristics in a crown glass with a high CTE of $94 \times 10^{-7} /K$ and a low MP of 724°C using a short-pulse CO₂ laser with a flat-top beam was investigated. The short laser pulse consisted of a spike pulse with a pulse width of 276 ns, a pulse tail with a length of 56.9 μs and an energy ratio of a spike pulse to a pulse tail of 1:20 at a repetition rate of 200 Hz. The laser beam had a flat-top profile with a beam quality factor M^2 of 13.5 and a diameter of 12.5 mm before a focusing lens. The flat-top beam was focused by the focusing lens with a focal length of 12.7 mm on the glass surface at a focus offset of -0.20 mm to +0.40 mm. The Rayleigh length was 188 μm. The flat-top beam produced conical holes at the focus offsets of -0.20 mm to +0.00 mm and produced cylindrical holes at the focus offsets of +0.20 mm to +0.40 mm. The drilling characteristics such as the dependence of a hole shape, a hole depth, a surface hole diameter, a ratio of a surface hole diameter to an irradiation diameter, a surface HAZ diameter, a ratio of a surface HAZ diameter to an irradiation diameter and properties of a cylindrical hole on a focus offset, a fluence per single pulse and a total irradiation fluence were investigated.

4.2.2 Experimental set-up

Fig. 4.2-1 shows the glass drilling set-up with a longitudinally excited CO₂ laser that has an adjustable optical cavity for producing a flat-top beam [25,28,30,141]. The longitudinally excited CO₂ laser produced a short pulse with a flat-top beam at a repetition rate of 200 Hz and a wavelength of 10.6 μm. Fig. 4.2-2 shows the laser pulse waveform. In the short pulse, a spike pulse width was 276 ns, and a pulse tail length was 56.9 μs. The energy ratio of a pulse spike to a pulse tail was 1:20. Fig. 4.2-3 shows a flat-top beam profile measured before the focusing lens. The flat-top beam had a diameter of 13.0 mm at $1/e^2$ of the peak intensity and 12.5 mm at 50% of the peak intensity. The beam diameter was 13.2 mm at 10% of the peak intensity and 10.1 mm at 90% of the peak intensity. The ratio of the beam diameter at 90% of the peak intensity

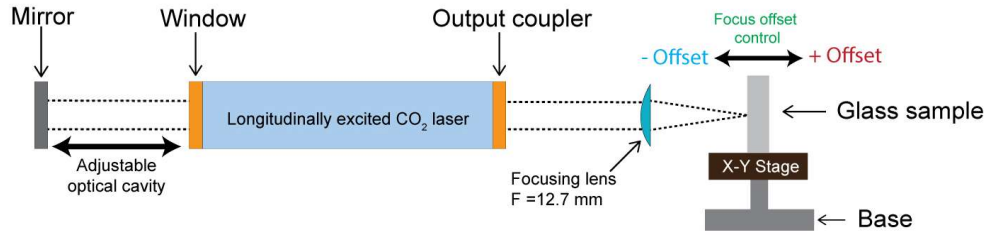


Fig. 4.2-1 Glass drilling set-up with longitudinally excited CO₂ laser.

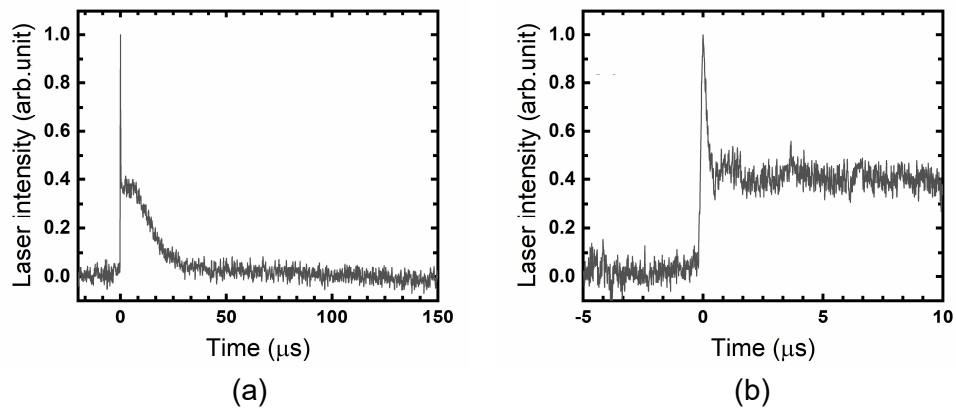


Fig. 4.2-2 Laser pulse waveform. Laser intensity was normalized to the maximum value of the spike pulse. (a) Overall waveform. (b) Magnified timescale of spike pulse.

to 10% of the peak intensity was 0.77. The correlation factor was 0.96 with a unit rectangular function. The estimated beam quality factor M^2 was 13.5. A ZnSe aspherical focusing lens with a focal length of 12.7 mm was used to focus the laser beam. An NA was 0.49, a DOF was 376 μm and a Rayleigh length was 188 μm . Fig. 4.2-4 shows the spot diameter and the fluence per single pulse at the focus offsets of -0.20 mm to +0.40 mm, where the minus sign and the plus sign indicate an in-focus and an out-of-focus offset, respectively. At the same focus offset with almost the same spot diameter, variable fluences were produced by changing the irradiation laser energy. In this study, a percussion drilling process in which a number of pulses were radiated at the same surface position of the sample glass, was used. A crown glass (Matsunami, S1127) with a high CTE of $94.0 \times 10^{-7} /\text{K}$, a low MP of 724°C and a thickness of 1150 μm was used as the sample. The sample was adjusted at the focus offsets of -0.20 mm to +0.40 mm by an X-Y stage, as shown in Fig. 4.2-1.

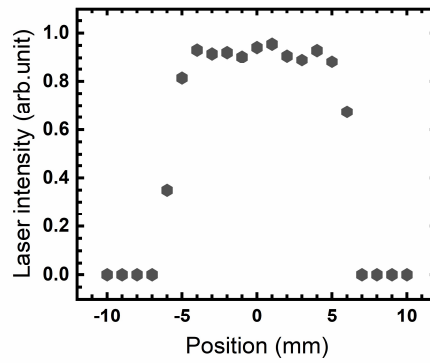


Fig. 4.2-3 Flat-top beam profile.

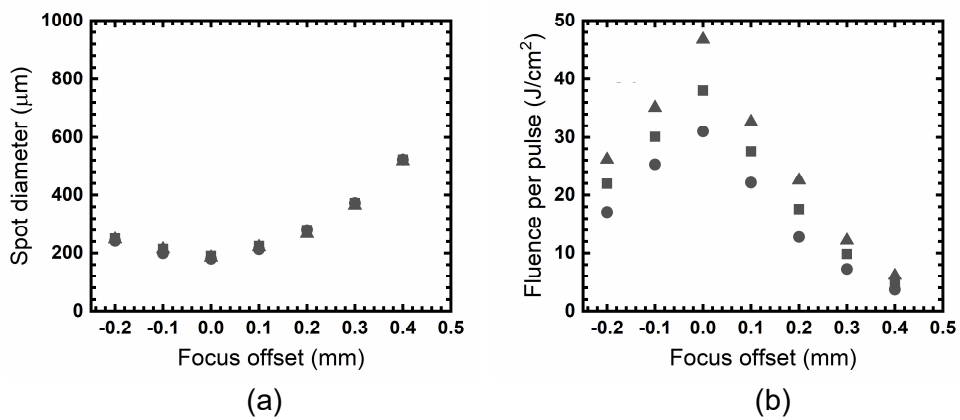


Fig. 4.2-4 Dependence of the spot diameter and the fluence per single pulse on the focus offset. (a) Spot diameter. (b) Fluence per single pulse. Circle, square and triangle symbols represent fluences per pulse of $31.0 \text{ J}/\text{cm}^2$, $38.0 \text{ J}/\text{cm}^2$ and $46.8 \text{ J}/\text{cm}^2$ at a focus offset of 0.00 mm .

4.2.3 Results and discussions

4.2.3.1 Investigation of cylindrical hole drilling

Fig. 4.2-5 shows top and side views of a sample glass irradiated by a flat-top beam at the focus offsets of -0.20 mm to $+0.40 \text{ mm}$, a number of pulses of 30 and a repetition rate of 200 Hz. Fig. 4.2-5 shows that the hole images depended on the focus offset. The focus offsets of -0.20 mm to 0.00 mm produced a conical hole. The focus offsets of $+0.20 \text{ mm}$ to $+0.40 \text{ mm}$ produced a cylindrical hole. The recovered flat-top beam at the focus offset of $+0.20 \text{ mm}$ to $+0.40 \text{ mm}$ produced the cylindrical hole.

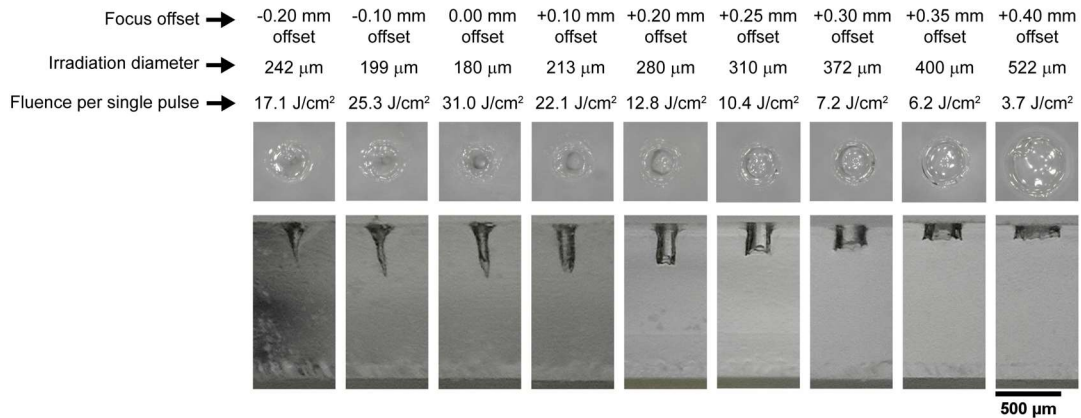


Fig. 4.2-5 Top and side views of a sample glass irradiated by a flat-top beam at the focus offsets of -0.20 mm to +0.40 mm, a number of pulses of 30 and a repetition rate of 200 Hz.

4.2.3.2 Investigation of the dependence of drilling characteristics on irradiation parameters

4.2.3.2.1 Hole depth and hole volume

Fig. 4.2-6 (a) shows the dependence of the hole depth on the focus offset, the fluence per single pulse and the total irradiation fluence, which is the product of the number of pulses and the fluence per single pulse. The hole depth depended on the focus offset and the total irradiation fluence. The hole depth was maximum at the focus offset of 0.00 mm and decreased toward the focus offsets of -0.20 mm and +0.40. At the same focus offset, the hole depth increased with the total irradiation fluence and became saturated. Because, when the hole depth increased, the heat generation at the bottom of the hole decreased. Fig. 4.2-6 (b) shows the dependence of the hole depth with the respective focus offset distance on the focus offset, the fluence per single pulse and the total irradiation fluence. The Fig. 4.2-6 (b) shows that the summation of the hole depth with the respective focus offset distance had the almost same average saturation hole depth of 585 μm . For example, the saturation hole depth was 564 μm at the focus offset of 0.00 mm with the fluence per single pulse of 46.8 J/cm² and the total irradiation fluence of 4209 J/cm², and the saturation hole depth was 577 μm at the focus offset of +0.40 mm with the fluence per single pulse of 3.7 J/cm² and the total irradiation fluence of 331 J/cm². In addition, the total irradiation fluence that reached at the average saturation hole depth of 585 μm was 2157 J/cm², 2896 J/cm², 3858 J/cm², 2698 J/cm², 1859 J/cm², 915 J/cm² and 500 J/cm² at a focus offset of -0.20 mm, -0.10

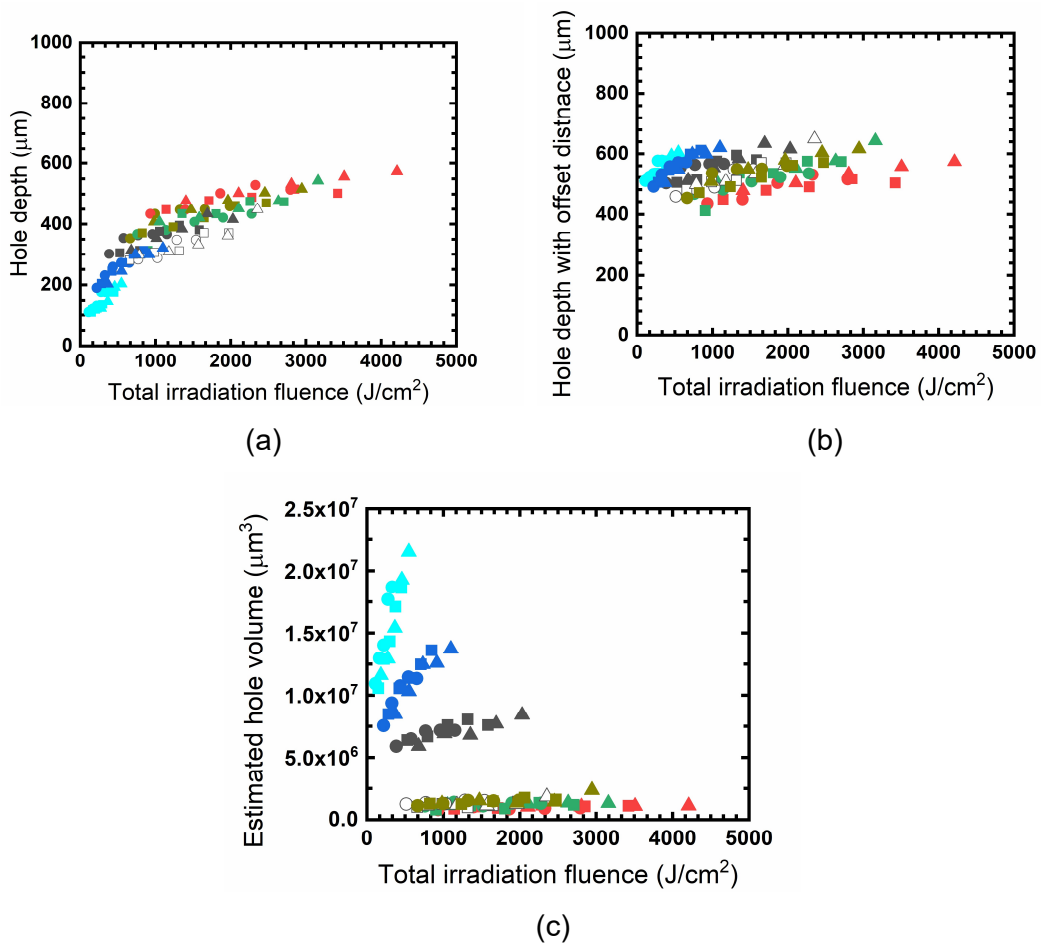


Fig. 4.2-6 Dependence of the hole depth and the hole depth with respective focus offset distance on the focus offset, the fluence per single pulse and the total irradiation fluence. (a) Hole depth. (b) Hole depth with respective focus offset distance. (c) Estimated hole volume. Symbol colors white, green, red, yellow, black, blue and cyan represent focus offsets of -0.20 mm, -0.10 mm, 0.00 mm, +0.10 mm, +0.20 mm, +0.30 mm and +0.40 mm, respectively. Table 4.2-1 presents the legend of Fig. 4.2-6 (a), (b) and (c).

Table 4.2-1 Legend of Fig. 4.2-6 (a), (b) and (c). The irradiation diameter for circle, square and triangle symbols at each focus offset corresponds to Fig. 4.2-4 (a).

	-0.20 mm	-0.10 mm	0.00 mm	+0.10 mm	+0.20 mm	+0.30 mm	+0.40 mm
	Fluence per single pulse	Fluence per single pulse	Fluence per single pulse	Fluence per single pulse	Fluence per single pulse	Fluence per single pulse	Fluence per single pulse
Circle	17.1 J/cm ²	25.3 J/cm ²	31.0 J/cm ²	22.1 J/cm ²	12.8 J/cm ²	7.2 J/cm ²	3.7 J/cm ²
Square	21.9 J/cm ²	30.1 J/cm ²	38.0 J/cm ²	27.5 J/cm ²	17.6 J/cm ²	9.4 J/cm ²	5.0 J/cm ²
Triangle	26.1 J/cm ²	35.1 J/cm ²	46.8 J/cm ²	32.7 J/cm ²	22.5 J/cm ²	12.2 J/cm ²	6.1 J/cm ²

mm, 0.00 mm, +0.10 mm, +0.20 mm, +0.30 mm and +0.40 mm. Fig. 4.2-6 (c) shows the dependence of the estimated hole volume on the focus offset, the fluence per single pulse and the total irradiation fluence. The estimated hole volume depended on the focus offset and the total irradiation fluence. Table 4.2-2 and Table 4.2-3 show the slope of the Fig. 4.2-6 (a) and (c) that is the hole depth and the estimated hole volume per the total irradiation fluence. The hole depth and the estimated hole volume per the total irradiation fluence was influenced by the focus offset and the fluence per single pulse. The hole depth and the estimated hole volume per the total irradiation fluence was higher at the focus offset of +0.40 mm than that at the focus offset of 0.00 mm. The hole depth and the estimated hole volume per the total irradiation fluence increased from the focus offset of 0.00 mm to the focus offset of -0.20 mm and +0.40 mm. A small fluence per single pulse results in a high drilling efficiency that is the same phenomena that was observed in Section 4.1.3.2.1 in Chapter 4.

Table 4.2-2 Slope of the Fig. 4.2-6 (a).








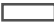






	-0.20 mm 	-0.10 mm 	0.00 mm 	+0.10 mm 	+0.20 mm 	+0.30 mm 	+0.40 mm 
	Hole depth/total irradiation fluence ($\mu\text{m}/\text{J}/\text{cm}^2$)	Hole depth/total irradiation fluence ($\mu\text{m}/\text{J}/\text{cm}^2$)	Hole depth/total irradiation fluence ($\mu\text{m}/\text{J}/\text{cm}^2$)	Hole depth/total irradiation fluence ($\mu\text{m}/\text{J}/\text{cm}^2$)	Hole depth/total irradiation fluence ($\mu\text{m}/\text{J}/\text{cm}^2$)	Hole depth/total irradiation fluence ($\mu\text{m}/\text{J}/\text{cm}^2$)	Hole depth/total irradiation fluence ($\mu\text{m}/\text{J}/\text{cm}^2$)
Circle	0.32	0.29	0.29	0.36	0.51	0.61	0.70
Square	0.27	0.25	0.24	0.28	0.37	0.51	0.51
Triangle	0.24	0.24	0.21	0.26	0.31	0.40	0.45

Table 4.2-3 Slope of the Fig. 4.2-6 (c).

	-0.20 mm 	-0.10 mm 	0.00 mm 	+0.10 mm 	+0.20 mm 	+0.30 mm 	+0.40 mm 
	Estimated hole volume/total irradiation fluence ($\mu\text{m}^3/\text{J}/\text{cm}^2$)	Estimated hole volume/total irradiation fluence ($\mu\text{m}^3/\text{J}/\text{cm}^2$)	Estimated hole volume/total irradiation fluence ($\mu\text{m}^3/\text{J}/\text{cm}^2$)	Estimated hole volume/total irradiation fluence ($\mu\text{m}^3/\text{J}/\text{cm}^2$)	Hole Estimated hole volume/total irradiation fluence ($\mu\text{m}^3/\text{J}/\text{cm}^2$)	Estimated hole volume/total irradiation fluence ($\mu\text{m}^3/\text{J}/\text{cm}^2$)	Estimated hole volume/total irradiation fluence ($\mu\text{m}^3/\text{J}/\text{cm}^2$)
Circle	1.54×10^3	0.94×10^3	0.56×10^3	1.17×10^3	9.93×10^3	25.4×10^3	72.3×10^3
Square	1.01×10^3	0.65×10^3	0.51×10^3	1.00×10^3	7.73×10^3	21.8×10^3	52.6×10^3
Triangle	0.92×10^3	0.69×10^3	0.42×10^3	0.88×10^3	5.86×10^3	17.0×10^3	47.0×10^3

4.2.3.2.2 Surface hole diameter and ratio of surface hole diameter to irradiation diameter

Fig. 4.2-7 (a) shows the dependence of the surface hole diameter on the focus offset, the fluence per single pulse and the total irradiation fluence. The surface hole diameter depended on the focus offset and did not depend on the fluence per single pulse and the total irradiation fluence. Fig. 4.2-7 (b) shows the dependence of the ratio of the surface hole diameter to the irradiation diameter on the focus offset, the fluence per single pulse and the total irradiation fluence. The ratio depended on the focus offset and did not depend on the fluence per single pulse and the total irradiation fluence. In the conical holes at the focus offsets of -0.20 mm to 0.00 mm, the ratio was 0.47 to 0.53 ; that is on an average 50% of the irradiation diameter contributed to the hole formation. In the cylindrical holes at the focus offsets of $+0.20$ mm, $+0.30$ mm and $+0.40$ mm, the ratios were 0.60 , 0.63 and 0.70 , respectively. Therefore, in the cylindrical holes at an out-of-focus offset, the drilling conditions provided a high ratio of the surface hole diameter to the irradiation diameter. The ratio of the surface hole diameter to the irradiation diameter at the focus offset of 0.00 mm was lower than that at the focus offset of $+0.20$ mm to $+0.40$ mm. At the focus offsets of 0.00 mm to $+0.20$ mm, the laser beam was estimated to be the gaussian-like beam that has a higher

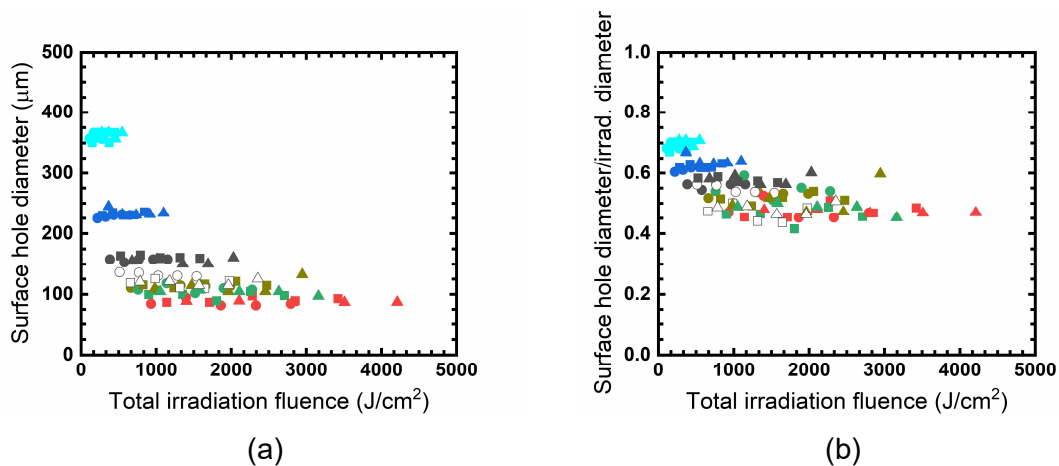









Fig. 4.2-7 Dependence of the surface hole diameter and the ratio of the surface hole diameter to the irradiation diameter on the focus offset, the fluence per single pulse and the total irradiation fluence. (a) Surface hole diameter. (b) Ratio of the surface hole diameter to the irradiation diameter. Symbol colors white, green, red, yellow, black, blue and cyan represent focus offsets of -0.20 mm, -0.10 mm, 0.00 mm, $+0.10$ mm, $+0.20$ mm, $+0.30$ mm and $+0.40$ mm, respectively. Table 4.2-4 presents the legend of Fig. 4.2-7 (a) and (b).

Table 4.2-4 Legend of Fig. 4.2-7 (a) and (b). The irradiation diameter for circle, square and triangle symbols at the each focus offset corresponds to Fig. 4.2-4 (a).

	-0.20 mm	-0.10 mm	0.00 mm	+0.10 mm	+0.20 mm	+0.30 mm	+0.40 mm
							
	Fluence per single pulse	Fluence per single pulse	Fluence per single pulse	Fluence per single pulse	Fluence per single pulse	Fluence per single pulse	Fluence per single pulse
Circle	17.1 J/cm ²	25.3 J/cm ²	31.0 J/cm ²	22.1 J/cm ²	12.8 J/cm ²	7.2 J/cm ²	3.7 J/cm ²
Square	21.9 J/cm ²	30.1 J/cm ²	38.0 J/cm ²	27.5 J/cm ²	17.6 J/cm ²	9.4 J/cm ²	5.0 J/cm ²
Triangle	26.1 J/cm ²	35.1 J/cm ²	46.8 J/cm ²	32.7 J/cm ²	22.5 J/cm ²	12.2 J/cm ²	6.1 J/cm ²

intensity in the center compared to the edges. At the focus offsets of +0.20 mm to +0.40 mm, the laser beam reformed as the flat-top beam that has the absence of the low intensity edges. Therefore, the focus offsets of +0.20 mm to +0.40 mm produced a high ratio of the surface hole diameter to the irradiation diameter due to maybe the absence of the low intensity edges in the flat-top beam.

4.2.3.2.3 Taper angle

Fig. 4.2-8 shows the dependence of the taper angle on the focus offset, the fluence per single pulse and the total irradiation fluence. The taper angle depended on the focus offset and did not depend on the fluence per single pulse and the total irradiation fluence. At the focus offset of +0.20 mm the average taper angle was 0.50°,

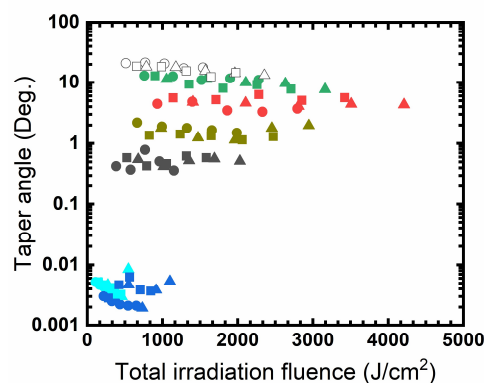









Fig. 4.2-8 Dependence of the taper angle on the focus offset, the fluence per single pulse and the total irradiation fluence. Symbol colors white, green, red, yellow, black, blue and cyan represent focus offsets of -0.20 mm, -0.10 mm, 0.00 mm, +0.10 mm, +0.20 mm, +0.30 mm and +0.40 mm, respectively. Table 4.2-5 presents the legend of Fig. 4.2-8.

Table 4.2-5 Legend of Fig. 4.2-8. The irradiation diameter for circle, square and triangle symbols at each focus offset corresponds to Fig. 4.2-4 (a).

	-0.20 mm 	-0.10 mm 	0.00 mm 	+0.10 mm 	+0.20 mm 	+0.30 mm 	+0.40 mm 
	Fluence per single pulse	Fluence per single pulse	Fluence per single pulse	Fluence per single pulse	Fluence per single pulse	Fluence per single pulse	Fluence per single pulse
Circle	17.1 J/cm ²	25.3 J/cm ²	31.0 J/cm ²	22.1 J/cm ²	12.8 J/cm ²	7.2 J/cm ²	3.7 J/cm ²
Square	21.9 J/cm ²	30.1 J/cm ²	38.0 J/cm ²	27.5 J/cm ²	17.6 J/cm ²	9.4 J/cm ²	5.0 J/cm ²
Triangle	26.1 J/cm ²	35.1 J/cm ²	46.8 J/cm ²	32.7 J/cm ²	22.5 J/cm ²	12.2 J/cm ²	6.1 J/cm ²

and at the focus offsets of +0.30 mm and +0.40 mm the average taper angle was 0.003°. Therefore, the produced holes at the focus offsets of +0.20 mm to +0.40 mm were cylindrical holes.

4.2.3.2.4 Aspect ratio and surface hole diameter relation with hole depth in cylindrical hole

Fig. 4.2-9 (a) shows the dependence of the aspect ratio, defined as the ratio of the hole depth to the surface hole diameter, of a cylindrical hole on the focus offset, the fluence per single pulse and the total irradiation fluence. The aspect ratio depended on

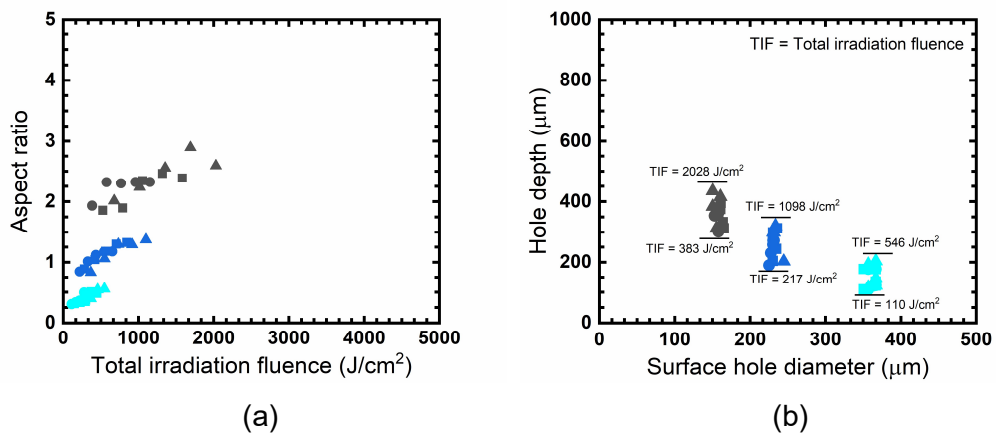





Fig. 4.2-9 Dependence of the aspect ratio of a cylindrical hole on the focus offset, the fluence per single pulse and the total irradiation fluence and the relation between the hole depth and the surface hole diameter in a cylindrical hole. (a) Aspect ratio. (b) Hole depth vs. surface hole diameter of a cylindrical hole. Symbol colors black, blue and cyan represent focus offsets of +0.20 mm, +0.30 mm and +0.40 mm, respectively. Table 4.2-6 presents the legend of Fig. 4.2-9 (a) and (b).

Table 4.2-6 Legend of Fig. 4.2-9 (a) and (b). The irradiation diameter for circle, square and triangle symbols at each focus offset corresponds to Fig. 4.2-4 (a).

	+0.20 mm 	+0.30 mm 	+0.40 mm 
	Fluence per single pulse	Fluence per single pulse	Fluence per single pulse
Circle	12.8 J/cm ²	7.2 J/cm ²	3.7 J/cm ²
Square	17.6 J/cm ²	9.4 J/cm ²	5.0 J/cm ²
Triangle	22.5 J/cm ²	12.2 J/cm ²	6.1 J/cm ²

the focus offset and the total irradiation fluence. In this study, the aspect ratio was from 0.30 to 2.89. Fig. 4.2-9 (b) shows the relation between the hole depth and the surface hole diameter in a cylindrical hole at the focus offsets of +0.20 mm to +0.40 mm. The depth of the cylindrical hole decreased as the surface hole diameter increased. To control the surface hole diameter and the hole depth of a cylindrical hole, an investigation using a variable-NA system will be required.

4.2.3.2.5 Surface HAZ diameter and ratio of surface HAZ diameter to irradiation diameter

Fig. 4.2-10 (a) shows the dependence of the surface HAZ diameter on the focus offset, the fluence per single pulse and the total irradiation fluence. The surface HAZ diameter depended on the focus offset and the total irradiation fluence and did not depend on the fluence per single pulse. Fig. 4.2-10 (b) shows the dependence of the ratio of the surface HAZ diameter to the irradiation diameter on the focus offset, the fluence per single pulse and the total irradiation fluence. The ratio depended on the focus offset and the total irradiation fluence and did not depend on the fluence per single pulse. In the conical holes at the focus offsets of -0.20 mm to 0.00 mm, the ratio was 1.50 to 2.04. In the cylindrical holes at the focus offsets of +0.20 mm to +0.40 mm, the ratio was 0.86 to 1.42. The ratio of the surface HAZ diameter to the irradiation diameter at the focus offset of 0.00 mm was higher than that at the focus offsets of +0.20 mm to +0.40 mm due to the role of the beam profile at the focus offsets as described in Section 4.2.3.2.2.

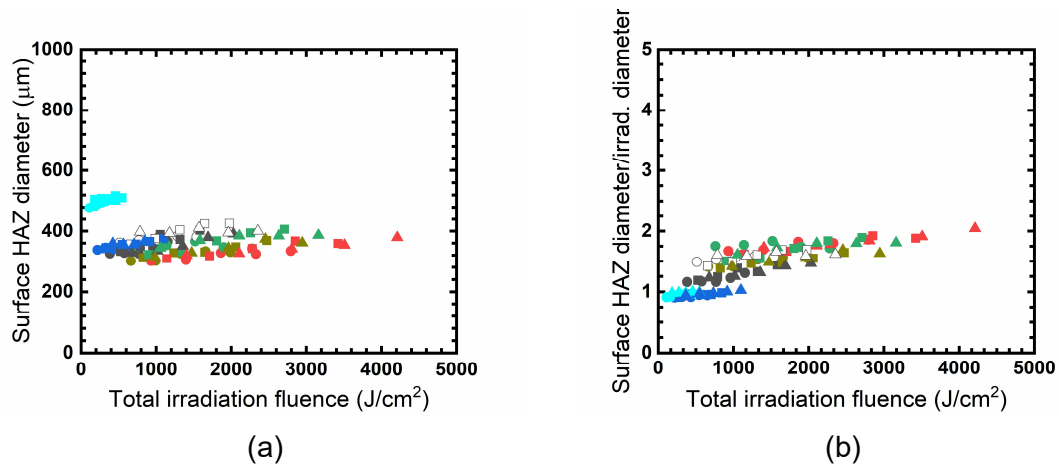


Fig. 4.2-10 Dependence of the surface HAZ diameter and the ratio of the surface HAZ diameter to the irradiation diameter on the focus offset, the fluence per single pulse and the total irradiation fluence. (a) Surface HAZ diameter. (b) Ratio of surface HAZ diameter to irradiation diameter. Symbol colors white, green, red, yellow, black, blue and cyan represent focus offsets of -0.20 mm, -0.10 mm, 0.00 mm, +0.10 mm, +0.20 mm, +0.30 mm and +0.40 mm, respectively. Table 4.2-7 presents the legend of Fig. 4.2-10 (a) and (b).

Table 4.2-7 Legend of Fig. 4.2-10 (a) and (b). The irradiation diameter for circle, square and triangle symbols at each focus offset corresponds to Fig. 4.2-4 (a).

	-0.20 mm	-0.10 mm	0.00 mm	+0.10 mm	+0.20 mm	+0.30 mm	+0.40 mm
	Fluence per single pulse	Fluence per single pulse	Fluence per single pulse	Fluence per single pulse	Fluence per single pulse	Fluence per single pulse	Fluence per single pulse
Circle	17.1 J/cm ²	25.3 J/cm ²	31.0 J/cm ²	22.1 J/cm ²	12.8 J/cm ²	7.2 J/cm ²	3.7 J/cm ²
Square	21.9 J/cm ²	30.1 J/cm ²	38.0 J/cm ²	27.5 J/cm ²	17.6 J/cm ²	9.4 J/cm ²	5.0 J/cm ²
Triangle	26.1 J/cm ²	35.1 J/cm ²	46.8 J/cm ²	32.7 J/cm ²	22.5 J/cm ²	12.2 J/cm ²	6.1 J/cm ²

4.2.4 Summary

In this experiment, cylindrical hole drilling in a crown glass with a high CTE of $94 \times 10^{-7} /K$ and a low MP of 724°C using a short-pulse CO₂ laser with a flat-top beam profile was investigated. The CO₂ laser produced a short laser pulse with a spike pulse width of 276 ns, a pulse tail length of 56.9 μs, an energy ratio of a spike pulse to a pulse tail of 1:20 and a flat-top beam with a diameter of 12.5 mm and a beam quality factor M² of 13.5 at a repetition rate of 200 Hz. The CO₂ laser produced cylindrical holes in the glass at the focus offsets of +0.20 mm to +0.40 mm, corresponding to the out-of-focus positions from the focal plane of a focusing lens with a focal length of 12.7 mm.

The Rayleigh length was 188 μm . In the cylindrical holes, the hole depth was 109 μm to 434 μm , the surface hole diameter was 152 μm to 366 μm , and the aspect ratio, defined as the ratio of the hole depth to the surface hole diameter, was 0.30 to 2.89. The hole depth depended on the focus offset and the total irradiation fluence. At the same focus offset, the hole depth increased with the total irradiation fluence and became saturated. The saturation hole depth did not depend on the total irradiation fluence and the average saturated hole depth with the respective focus offset distance was 585 μm . The taper angle and the ratio of the surface hole diameter to the irradiation diameter depended on the focus offset and did not depend on the fluence per single pulse and the total irradiation fluence. The ratio of the surface HAZ diameter to the irradiation diameter depended on the focus offset and the total irradiation fluence and did not depend on the fluence per single pulse.

4.3 Comparison of a crown glass drilling characteristics in a short-pulse CO₂ laser with two different beam profiles

4.3.1 Introduction

In this experiment, the drilling characteristics of a crown glass with a high CTE of $94 \times 10^{-7} /\text{K}$ and a low MP of 724°C by a short-pulse CO₂ laser with a central-peak-intensity beam and a flat-top beam were investigated. The CO₂ laser produced a short pulse with a spike pulse width of 276 ns, a pulse tail length of 56.9 μs , an energy ratio of a spike pulse to a pulse tail of 1:20 and a central-peak-intensity beam or a flat-top beam at a repetition rate of 200 Hz. In the central-peak-intensity beam and the flat-top beam, a beam diameter before a focusing lens was 12.5 mm and a beam quality factor M^2 was 7.6 and 13.5, respectively. The laser beam was focused by a focusing lens with a focal length of 12.7 mm on the glass surface at the focus offsets of -0.20 mm to +0.20 mm. The central-peak-intensity beam produced conical holes at the focus offsets of -0.20 mm to -0.10 mm and produced biconical holes with a wide waist diameter at the focus offsets of 0.00 mm to +0.20 mm. The flat-top beam produced conical holes at the focus offsets of -0.20 mm to +0.10 mm and produced a cylindrical hole at the focus offset of +0.20 mm. The drilling characteristics such as the dependence of a hole shape, a hole depth, a surface hole diameter, a ratio of a surface hole diameter to an irradiation diameter, a surface HAZ diameter, a ratio of a surface HAZ diameter to an irradiation diameter and properties of a biconical hole on a beam profile, a focus offset, a fluence per single pulse and a total irradiation fluence were investigated.

4.3.2 Experimental set-up

Fig. 4.3-1 shows the glass drilling set-up with a longitudinally excited CO₂ laser with an adjustable optical cavity for producing a central-peak-intensity beam that is not a gaussian and a flat-top beam [25,28,30,141]. The longitudinally excited CO₂ laser produced a short pulse with a central-peak-intensity beam or a flat-top beam at a repetition rate of 200 Hz and a wavelength of 10.6 μm . Fig. 4.3-2 shows the laser pulse waveform. In the short pulse, a spike pulse width was 276 ns, and a pulse tail length was 56.9 μs . The energy ratio of a spike pulse to a pulse tail was 1:20. Fig. 4.3-3 (a) and (b) show the central-peak-intensity beam and the flat-top beam profile measured before the focusing lens, respectively. The central-peak-intensity beam had a diameter

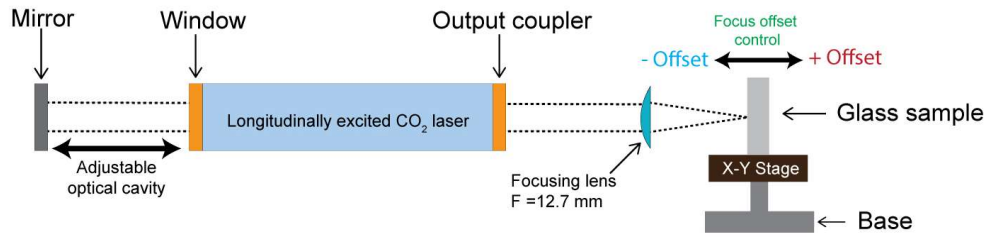


Fig. 4.3-1 Glass drilling set-up with longitudinally excited CO₂ laser.

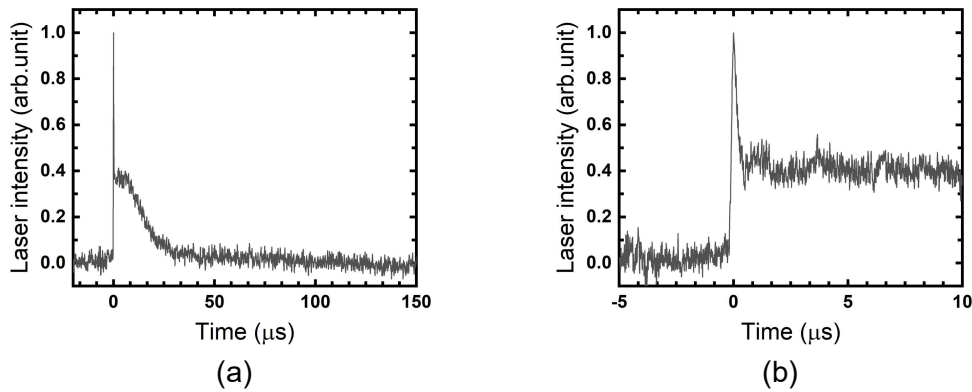


Fig. 4.3-2 Laser pulse waveform. The laser intensity was normalized to the maximum value of the spike pulse. (a) Overall waveform. (b) Magnified timescale of spike pulse.

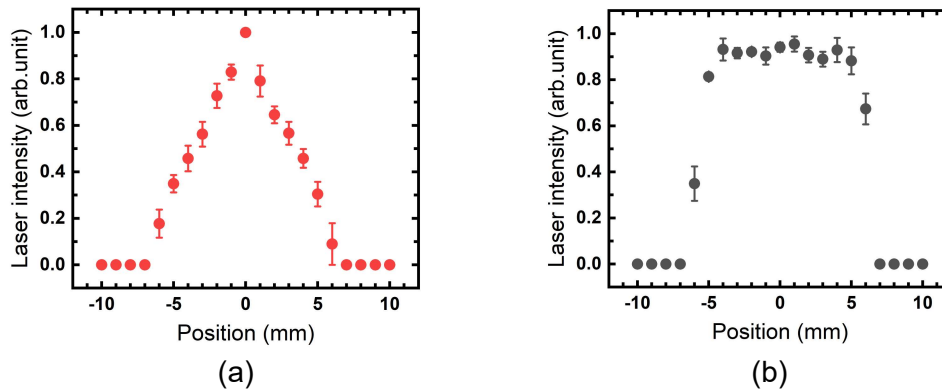


Fig. 4.3-3 Laser beam profiles. (a) Central-peak-intensity beam. (b) Flat-top beam.

of 12.5 mm at $1/e^2$ that is at 13.5% of the peak intensity. The estimated beam quality factor M^2 was 7.60. The flat-top beam had a diameter of 13.0 mm at $1/e^2$ of the peak intensity and 12.5 mm at 50% of the peak intensity. The beam diameter was 13.2 mm at 10% of the peak intensity and 10.1 mm at 90% of the peak intensity. The ratio of the beam diameter at 90% of the peak intensity to 10% of the peak intensity was 0.77. The

estimated beam quality factor M^2 was 13.5. A ZnSe aspherical focusing lens with a focal length of 12.7 mm was used to focus the laser beam. An NA was 0.49. A DOF was 212 μm and 376 μm in the central-peak-intensity beam and the flat-top beam, respectively. A Rayleigh length was 106 μm and 188 μm in the central-peak-intensity beam and the flat-top beam, respectively.

Fig. 4.3-4 (a) and (b) show a spot diameter and a fluence per single pulse at the focus offsets of -0.20 mm to +0.20 mm in the central-peak-intensity beam and the flat-top beam, respectively. At the same focus offset in the central-peak-intensity beam and the flat-top beam, the fluence per single pulse was controlled by changing the irradiation laser energy. In this study, a percussion drilling method was performed at a focus offset of -0.20 mm to +0.20 mm. A crown glass (Matsunami, S1127) with a CTE of $94 \times 10^{-7} /\text{K}$, an MP of 724°C and a thickness of 1150 μm was used as the sample. The sample was adjusted at the focus offsets of -0.20 mm to +0.20 mm by an X-Y stage as shown in Fig. 4.3-1.

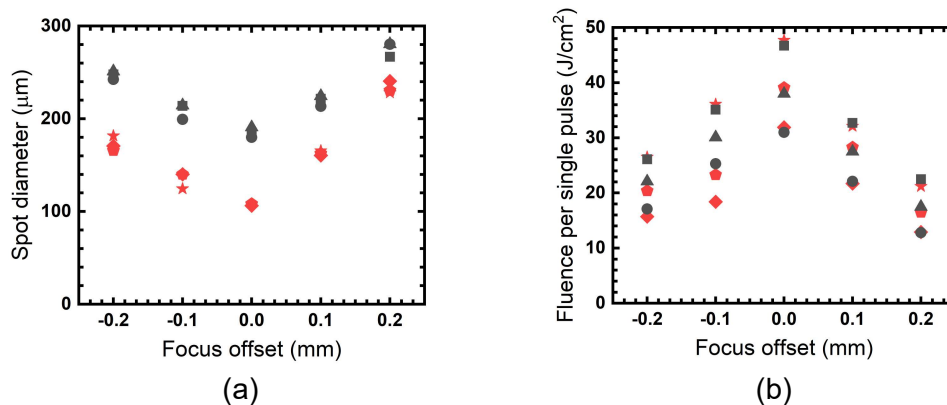
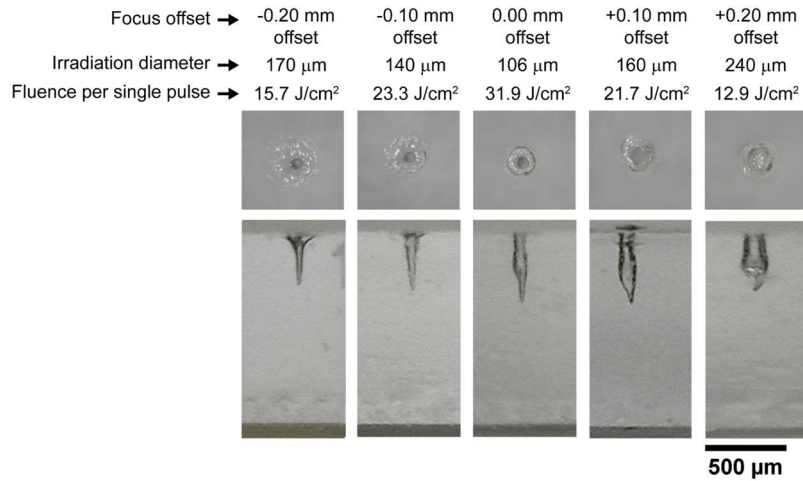


Fig. 4.3-4 Dependence of a spot diameter and a fluence per single pulse on a focus offset. Red and black symbols represent the central-peak-intensity beam and the flat-top beam, respectively. (a) Spot diameter. (b) Fluence per single pulse.

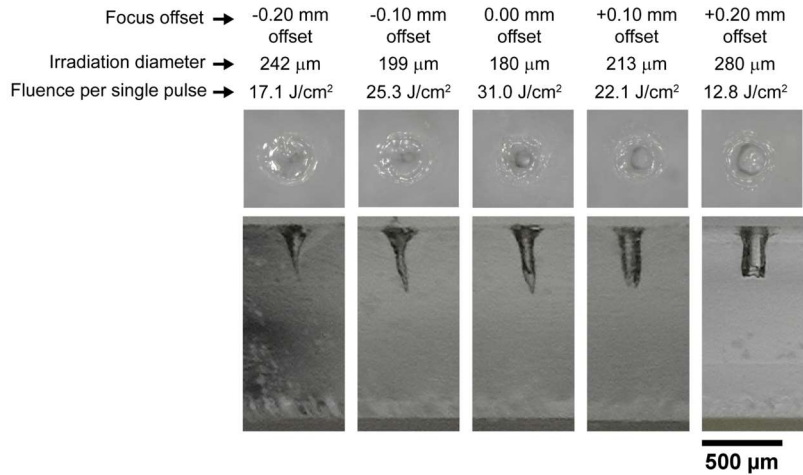
4.3.3 Results and discussions

4.3.3.1 Investigation of a hole shape

Fig. 4.3-5 (a) and (b) shows top and side views of a sample glass irradiated by the central-peak-intensity beam and the flat-top beam at the focus offsets of -0.20 mm to +0.20 mm, a number of pulses of 30 and a repetition rate of 200 Hz. Fig. 4.3-5 shows that the hole images depended on the focus offset and a beam profile. The incident



(a)



(b)

Fig. 4.3-5 Top and side views of a sample glass irradiated by the central-peak-intensity beam and the flat-top beam at focus offsets of -0.20 mm to +0.20 mm, a number of pulses of 30 and a repetition rate of 200 Hz. (a) Top and side views of a sample glass in the central-peak-intensity beam. (b) Top and side views of a sample glass in the Flat-top beam.

central-peak-intensity beam produced a conical hole at the focus offset of -0.20 mm to -0.10 mm and produced a biconical hole with a wide waist diameter at the focus offset of 0.00 mm to +0.20 mm. The biconical hole was produced by the central-peak-intensity beam irradiation with a short focal length of the focusing lens. The laser beam intensity may be absorbed by the side walls in the hole resulting a wide waist and the hole bottom got narrow down as the beam propagated inside the hole. The incident flat-top beam produced a conical hole at a focus offset of -0.20 mm to +0.10 mm and

produced a cylindrical hole at a focus offset of +0.20 mm. The cylindrical hole was produced by the recovered flat-top beam at the focus offset of +0.20 mm to +0.40 mm.

4.3.3.2 Comparison of the dependence of drilling characteristics

4.3.3.2.1 Hole depth and hole volume

Fig. 4.3-6 (a) and (b) show the dependence of the hole depth on the focus offset, the fluence per single pulse and the total irradiation fluence that is the product of the number of pulses and the fluence per single pulse in the central-peak-intensity beam and the flat-top beam, respectively. The hole depth depended on the focus offset and the total irradiation fluence and did not depend on the beam profile. At the same focus offset, the hole depth increased with the total irradiation fluence and became saturated. The reason for this is that, when the hole depth increased, the heat generation at the bottom of the hole decreased. The hole depth was maximum at the focus offset of 0.00 mm and decreased toward the focus offsets of -0.20 mm and +0.20. Fig. 4.3-6 (c) and (d) show the dependence of the estimated hole volume on the focus offset, the fluence per single pulse and the total irradiation fluence in the central-peak-intensity beam and the flat-top beam, respectively. The estimated hole volume depended on the focus offset and the total irradiation fluence. Table 4.3-2 and Table 4.3-3 show the slope of the Fig. 4.3-6 (a) and (b) and Fig. 4.3-6 (c) and (d) that is the hole depth and the estimated hole volume per the total irradiation fluence in the central-peak-intensity beam and the flat-top beam, respectively. The hole depth and the estimated hole volume per the total irradiation fluence was influenced by the focus offset and the fluence per single pulse. The hole depth and the estimated hole volume per the total irradiation fluence increased from the focus offset of 0.00 mm to the focus offset of -0.20 mm and +0.20 mm in the central-peak-intensity beam and the flat-top beam. The hole depth and the estimated hole volume per the total irradiation fluence was higher at the focus offset of +0.20 mm than that at the focus offset of 0.00 mm in the central-peak-intensity beam and the flat-top beam. A small fluence per single pulse results in a high drilling efficiency that is the same phenomena that was observed in the previous experimented results described in Section 4.1.3.2.1 and Section 4.2.3.2.1.

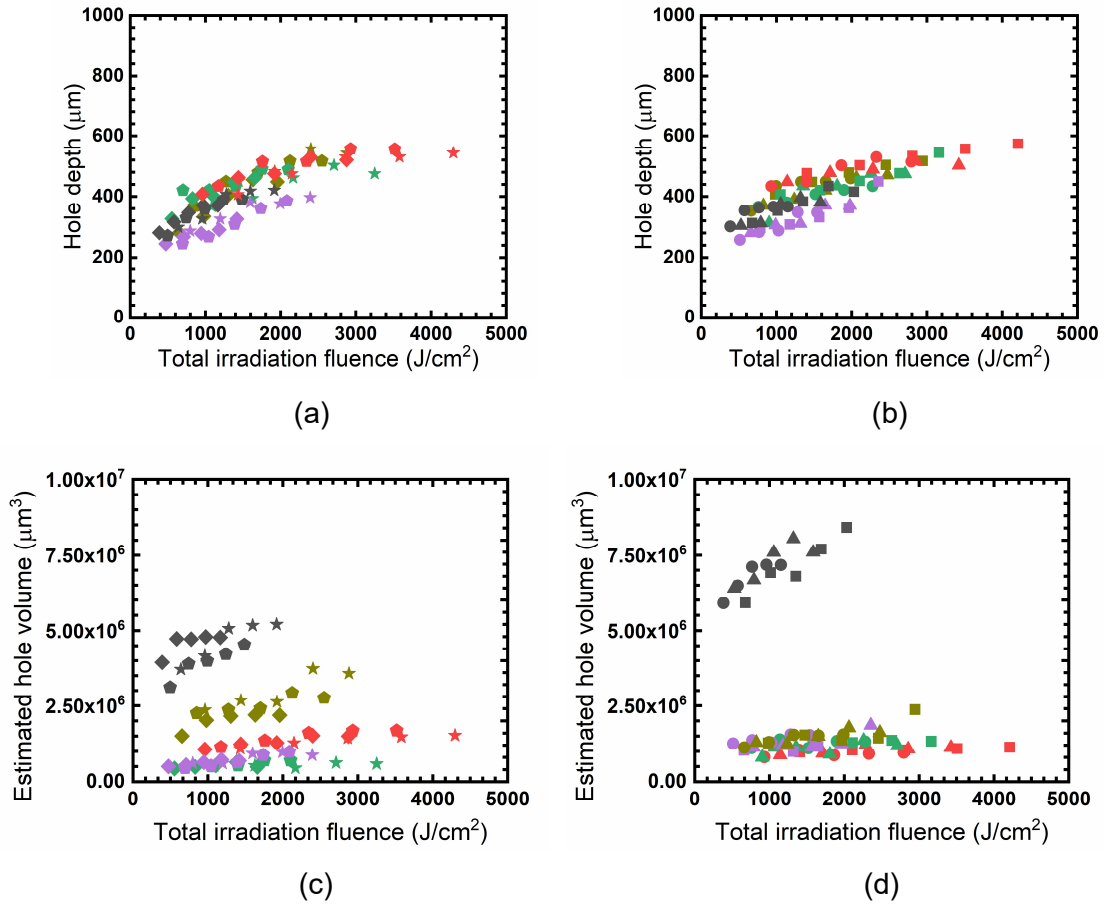


Fig. 4.3-6 Dependence of the hole depth and the estimated hole volume on the beam profile, the focus offset, the fluence per single pulse and the total irradiation fluence. (a) and (b) Hole depth in the central-peak-intensity beam and the flat-top beam, respectively. (c) and (d) Estimated hole volume in the central-peak-intensity beam and the flat-top beam, respectively. Symbol colors purple, green, red, yellow and black represent focus offsets of -0.20 mm, -0.10 mm, 0.00 mm, +0.10 mm and +0.20 mm, respectively. Table 4.3-1 presents the legend of Fig. 4.3-6 (a) to (d).

Table 4.3-1 Legend of Fig. 4.3-6 (a) to (d). The irradiation diameter for diamond, pentagon, star, circle, triangle and square symbols at each focus offset corresponds to Fig. 4.3-4 (a).






		-0.20 mm 	-0.10 mm 	0.00 mm 	+0.10 mm 	+0.20 mm 
		Fluence per single pulse	Fluence per single pulse	Fluence per single pulse	Fluence per single pulse	Fluence per single pulse
Central-peak-intensity beam	Diamond	15.7 J/cm ²	18.4 J/cm ²	31.9 J/cm ²	21.7 J/cm ²	12.9 J/cm ²
	Pentagon	23.1 J/cm ²	23.3 J/cm ²	39.1 J/cm ²	28.3 J/cm ²	16.5 J/cm ²
	Star	26.5 J/cm ²	36.1 J/cm ²	47.7 J/cm ²	32.1 J/cm ²	21.2 J/cm ²
Flat-top beam	Circle	17.1 J/cm ²	25.3 J/cm ²	31.0 J/cm ²	22.1 J/cm ²	12.8 J/cm ²
	Triangle	21.9 J/cm ²	30.1 J/cm ²	38.0 J/cm ²	27.5 J/cm ²	17.6 J/cm ²
	Square	26.1 J/cm ²	35.1 J/cm ²	46.8 J/cm ²	32.7 J/cm ²	22.5 J/cm ²

Table 4.3-2 Slopes of Fig. 4.3-6 (a) and (b).











		-0.20 mm 	-0.10 mm 	0.00 mm 	+0.10 mm 	+0.20 mm 
		Hole depth/total irradiation fluence (μm/J/cm ²)	Hole depth/total irradiation fluence (μm/J/cm ²)	Hole depth/total irradiation fluence (μm/J/cm ²)	Hole depth/total irradiation fluence (μm/J/cm ²)	Hole depth/total irradiation fluence (μm/J/cm ²)
Central-peak-intensity beam	Diamond	0.33	0.40	0.27	0.31	0.48
	Pentagon	0.24	0.36	0.24	0.30	0.38
	Star	0.24	0.22	0.19	0.27	0.32
Flat-top beam	Circle	0.32	0.29	0.29	0.36	0.51
	Triangle	0.27	0.25	0.24	0.28	0.37
	Square	0.24	0.24	0.21	0.26	0.31

Table 4.3-3 Slopes of Fig. 4.3-6 (c) and (d).

		-0.20 mm 	-0.10 mm 	0.00 mm 	+0.10 mm 	+0.20 mm 
		Estimated hole volume/total irradiation fluence ($\mu\text{m}^3/\text{J}/\text{cm}^2$)	Estimated hole volume/total irradiation fluence ($\mu\text{m}^3/\text{J}/\text{cm}^2$)	Estimated hole volume/total irradiation fluence ($\mu\text{m}^3/\text{J}/\text{cm}^2$)	Estimated hole volume/total irradiation fluence ($\mu\text{m}^3/\text{J}/\text{cm}^2$)	Estimated hole volume/total irradiation fluence ($\mu\text{m}^3/\text{J}/\text{cm}^2$)
Central-peak-intensity beam	Diamond	0.72×10^3	0.52×10^3	0.75×10^3	1.70×10^3	6.69×10^3
	Pentagon	0.52×10^3	0.46×10^3	0.69×10^3	1.68×10^3	4.41×10^3
	Star	0.54×10^3	0.28×10^3	0.52×10^3	1.65×10^3	4.02×10^3
Flat-top beam	Circle	1.54×10^3	0.94×10^3	0.56×10^3	1.17×10^3	9.93×10^3
	Triangle	1.01×10^3	0.65×10^3	0.51×10^3	1.00×10^3	7.73×10^3
	Square	0.92×10^3	0.69×10^3	0.42×10^3	0.88×10^3	5.86×10^3

4.3.3.2.2 Surface hole diameter and ratio of surface hole diameter to irradiation diameter

Fig. 4.3-7 (a) and (b) show the dependence of the surface hole diameter on the focus offset, the fluence per single pulse and the total irradiation fluence in the central-peak-intensity beam and the flat-top beam, respectively. The surface hole diameter depended on the beam profile and the focus offset, and did not depend on fluence per single pulse and the total irradiation fluence. For example, in the central-peak-intensity beam at a focus offset of 0.00 mm with a fluence per single pulse of $31.9 \text{ J}/\text{cm}^2$, $39.1 \text{ J}/\text{cm}^2$ and $47.7 \text{ J}/\text{cm}^2$, the average surface hole diameter was $55.0 \mu\text{m}$, $58.4 \mu\text{m}$ and $56.1 \mu\text{m}$, respectively. In a flat-top beam at a focus offset of 0.00 mm with a fluence per single pulse of $31.0 \text{ J}/\text{cm}^2$, $38.0 \text{ J}/\text{cm}^2$, and $46.7 \text{ J}/\text{cm}^2$, the average surface hole diameter was $85.2 \mu\text{m}$, $90.4 \mu\text{m}$ and $87.5 \mu\text{m}$, respectively. The surface hole diameter by the central-peak-intensity beam was small because of the small irradiation diameter that is natural phenomena of laser drilling. Fig. 4.3-7 (c) and (d) show the dependence of the ratio of the surface hole diameter to the irradiation diameter on the focus offset, the fluence per single pulse and the total irradiation fluence in the central-peak-intensity beam and the flat-top beam, respectively. The ratio did not depend on the fluence per single pulse and the total irradiation fluence. The ratio depended on the focus offset. At various irradiation conditions, at the focus offset of -0.20 mm to 0.00 mm in the central-peak-intensity beam and the flat-top beam, the average ratio was

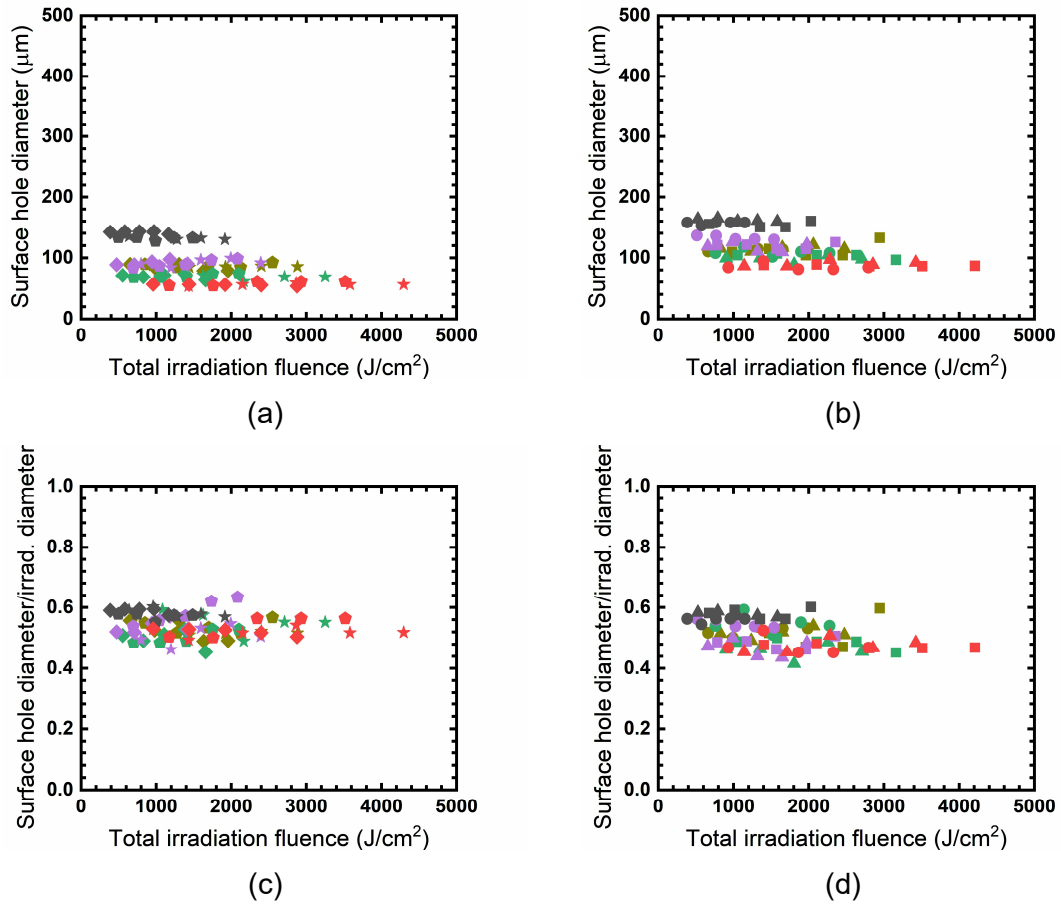







Fig. 4.3-7 Dependence of the surface hole diameter and the ratio of the surface hole diameter to the irradiation diameter on the beam profile, the focus offset, the fluence per single pulse and the total irradiation fluence. (a) and (b) Surface hole diameter in the central-peak-intensity beam and the flat-top beam, respectively. (c) and (d) Ratio of the surface hole diameter to the irradiation diameter in the central-peak-intensity beam and the flat-top beam, respectively. Symbol colors purple, green, red, yellow and black represent focus offsets of -0.20 mm, -0.10 mm, 0.00 mm, +0.10 mm and +0.20 mm, respectively. Table 4.3-4 presents the legend of Fig. 4.3-7 (a) to (d).

Table 4.3-4 Legend of Fig. 4.3-7 (a) to (d). The irradiation diameter for diamond, pentagon, star, circle, triangle and square symbols at each focus offset corresponds to Fig. 4.3-4 (a).

		-0.20 mm 	-0.10 mm 	0.00 mm 	+0.10 mm 	+0.20 mm 
		Fluence per single pulse	Fluence per single pulse	Fluence per single pulse	Fluence per single pulse	Fluence per single pulse
Central-peak-intensity beam	Diamond	15.7 J/cm ²	18.4 J/cm ²	31.9 J/cm ²	21.7 J/cm ²	12.9 J/cm ²
	Pentagon	23.1 J/cm ²	23.3 J/cm ²	39.1 J/cm ²	28.3 J/cm ²	16.5 J/cm ²
	Star	26.5 J/cm ²	36.1 J/cm ²	47.7 J/cm ²	32.1 J/cm ²	21.2 J/cm ²
Flat-top beam	Circle	17.1 J/cm ²	25.3 J/cm ²	31.0 J/cm ²	22.1 J/cm ²	12.8 J/cm ²
	Triangle	21.9 J/cm ²	30.1 J/cm ²	38.0 J/cm ²	27.5 J/cm ²	17.6 J/cm ²
	Square	26.1 J/cm ²	35.1 J/cm ²	46.8 J/cm ²	32.7 J/cm ²	22.5 J/cm ²

0.50 that is 50% of the irradiation diameter contributed to the hole creation. At the focus offset of +0.20 mm in the central-peak-intensity beam and the flat-top beam, the average ratio was 0.58 that is 58% of the irradiation diameter contributed to the hole creation. The ratio of the surface hole diameter to the irradiation diameter at the focus offset of 0.00 mm was lower than that at the focus offset of +0.20 mm. At the focus offsets of 0.00 mm, the laser beams were estimated to be the gaussian-like beam that has a higher intensity in the center compared to the edges. At the focus offsets of +0.20 mm, the flat-top beam reformed as the flat-top beam that has the absence of the low intensity edges. Therefore, the focus offsets of +0.20 mm produced a high ratio of the surface hole diameter to the irradiation diameter due to maybe the absence of the low intensity edges in the flat-top beam.

4.3.3.2.3 Ratio of a waist diameter to surface hole diameter and ratio of a waist depth to hole depth in biconical hole

Fig. 4.3-8 (a) shows the dependence of the ratio of the waist diameter to the surface hole diameter on the focus offset, the fluence per single pulse and the total irradiation fluence in the biconical hole. The ratio of the waist diameter to the surface hole diameter was depended on the focus offset and did not depend on the fluence per single pulse and the total irradiation fluence. The average ratio of the waist diameter to the surface hole diameter was 1.46, 1.32 and 1.17 at the focus offset of 0.00 mm, +0.10 mm and +0.20 mm, respectively. Fig. 4.3-8 (b) shows the dependence of the ratio of a

waist depth to the hole depth on the focus offset, the fluence per single pulse and the total irradiation fluence. The ratio of the waist depth to the hole depth slightly depended on the focus offset and did not depend on the fluence per single pulse and the total irradiation fluence. The average ratio of the waist depth to the hole depth was 0.48, 0.51 and 0.55 at the focus offset of 0.00 mm, +0.10 mm and +0.20 mm, respectively that is the waist depth was almost at the half of the hole depth.

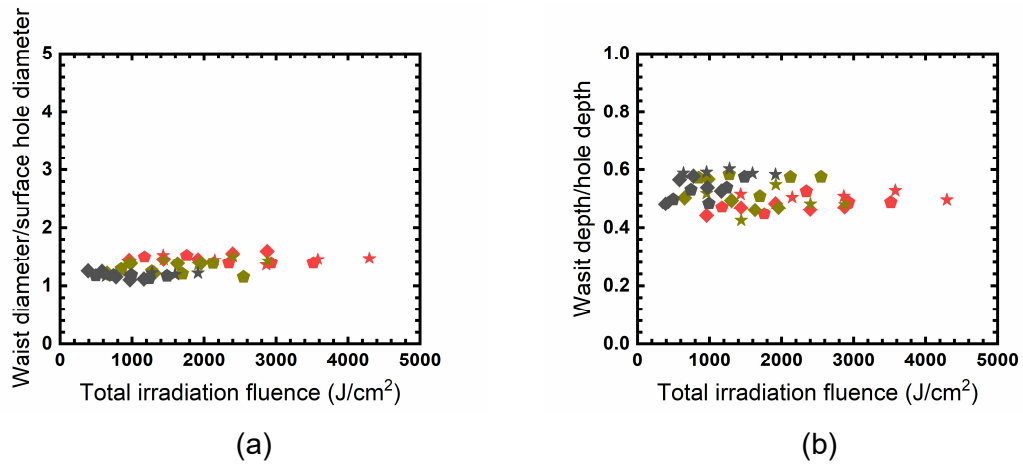





Fig. 4.3-8 Dependence of the ratio of a waist diameter to the surface hole diameter and the ratio of the waist depth to the hole depth in a biconical hole. (a) Ratio of the waist diameter to the surface hole diameter. (b) Ratio of the waist depth to the hole depth. Symbol colors red, yellow and black represent focus offsets of 0.00 mm, +0.10 mm and +0.20 mm, respectively. Table 4.3-5 presents the legend of Fig. 4.3-8 (a) and (b).

Table 4.3-5 Legend of Fig. 4.3-8 (a) and (b). The irradiation diameter for diamond, pentagon and star symbols at each focus offset corresponds to Fig. 4.3-4 (a).

		0.00 mm	+0.10 mm	+0.20 mm
				
		Fluence per single pulse	Fluence per single pulse	Fluence per single pulse
Central-peak-intensity beam	Diamond	31.9 J/cm ²	21.7 J/cm ²	12.9 J/cm ²
	Pentagon	39.1 J/cm ²	28.3 J/cm ²	16.5 J/cm ²
	Star	47.7 J/cm ²	32.1 J/cm ²	21.2 J/cm ²

4.3.3.2.4 Surface HAZ diameter and ratio of surface HAZ diameter to irradiation diameter

Fig. 4.3-9 (a) and (b) show the dependence of the surface HAZ diameter on the focus offset, the fluence per single pulse and the total irradiation fluence in the central-peak-intensity beam and the flat-top beam, respectively. The surface HAZ diameter depended on the beam profile, the focus offset and the total irradiation fluence and did not depend on the fluence per single pulse. Fig. 4.3-9 (c) and (d) show the dependence of the ratio of the surface HAZ diameter to the irradiation diameter on the focus offset,

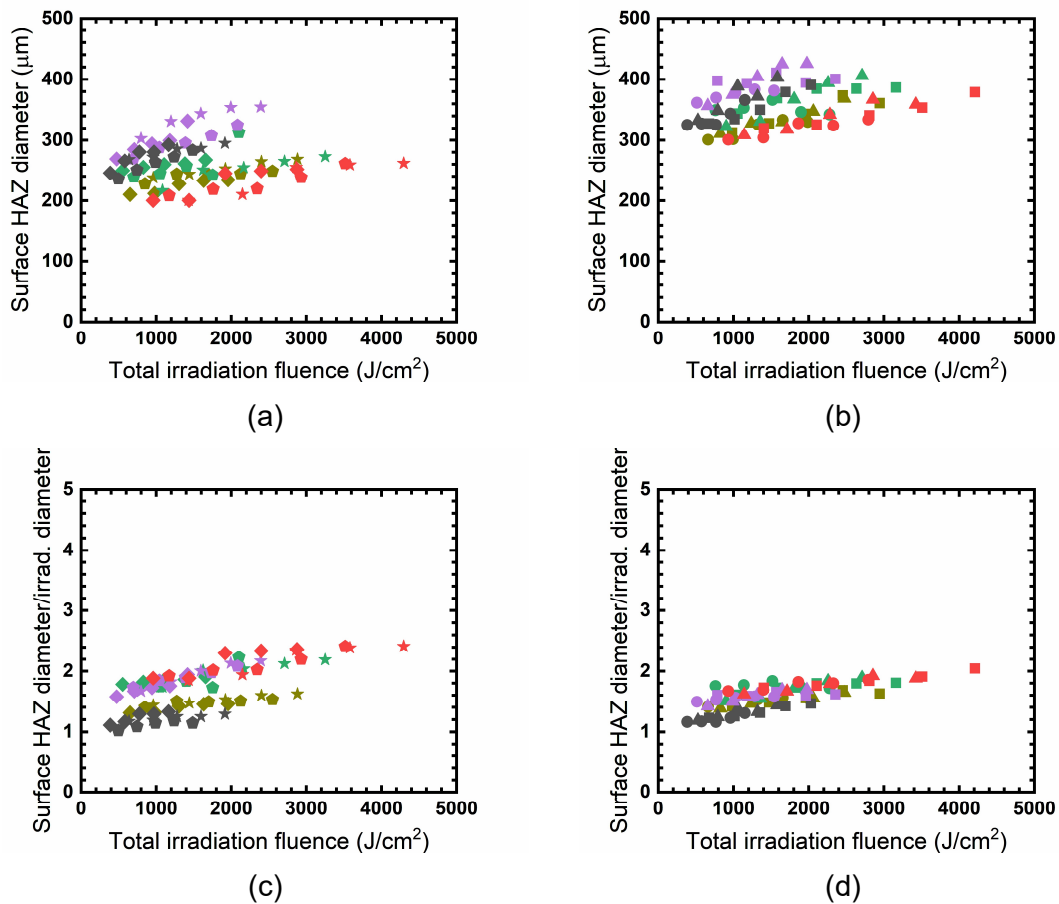







Fig. 4.3-9 Dependence of a ratio of a surface HAZ diameter to an irradiation diameter on a beam profile, a focus offset, a fluence per single pulse and a total irradiation fluence. (a) and (b) Surface HAZ diameter in the central-peak-intensity beam and the flat-top beam, respectively. (c) and (d) Ratio of a surface HAZ diameter to an irradiation diameter in the central-peak-intensity beam and the flat-top beam, respectively. Symbol colors purple, green, red, yellow and black represent focus offsets of -0.20 mm, -0.10 mm, 0.00 mm, +0.10 mm and +0.20 mm, respectively. Table 4.3-6 presents the legend of Fig. 4.3-9 (a) to (d).

Table 4.3-6 Legend of Fig. 4.3-9 (a) to (d). The irradiation diameter for cross, pentagon, star, circle, triangle and square symbols at each focus offset corresponds to Fig. 4.3-4 (a).

		-0.20 mm 	-0.10 mm 	0.00 mm 	+0.10 mm 	+0.20 mm 
		Fluence per single pulse	Fluence per single pulse	Fluence per single pulse	Fluence per single pulse	Fluence per single pulse
Central-peak-intensity beam	Diamond	15.7 J/cm ²	18.4 J/cm ²	31.9 J/cm ²	21.7 J/cm ²	12.9 J/cm ²
	Pentagon	23.1 J/cm ²	23.3 J/cm ²	39.1 J/cm ²	28.3 J/cm ²	16.5 J/cm ²
	Star	26.5 J/cm ²	36.1 J/cm ²	47.7 J/cm ²	32.1 J/cm ²	21.2 J/cm ²
Flat-top beam	Circle	17.1 J/cm ²	25.3 J/cm ²	31.0 J/cm ²	22.1 J/cm ²	12.8 J/cm ²
	Triangle	21.9 J/cm ²	30.1 J/cm ²	38.0 J/cm ²	27.5 J/cm ²	17.6 J/cm ²
	Square	26.1 J/cm ²	35.1 J/cm ²	46.8 J/cm ²	32.7 J/cm ²	22.5 J/cm ²

the fluence per single pulse and the total irradiation fluence in the central-peak-intensity beam and the flat-top beam, respectively. The ratio depended on the beam profile, the focus offset and the total irradiation fluence and did not depend on the fluence per single pulse. At the focus offsets of -0.20 mm to 0.00 mm, the ratio of a surface HAZ diameter to the irradiation diameter was smaller in the flat-top beam than the central-peak-intensity beam and at the focus offsets of +0.10 mm and +0.20 mm the ratio was almost the same. For example, at the focus offsets of 0.00 mm with a total irradiation fluence of about 1000 J/cm² the ratio was 1.92 and 1.67 in the central-peak-intensity beam and the flat-top beam, respectively. At the focus offset of +0.20 mm with a total irradiation fluence of about 1000 J/cm² the ratio was 1.10 and 1.16 in the central-peak-intensity beam and the flat-top beam, respectively. Therefore, at the focus offset of +0.20 mm the ratio of the surface HAZ diameter to the irradiation diameter was smaller compared to the focus offset of 0.00 mm. At the focus offsets of 0.00 mm, the laser beams were estimated to be the gaussian-like beam that has a higher intensity in the center compared to the edges. At the focus offsets of +0.20 mm, the flat-top beam reformed as the flat-top beam that has the absence of the low intensity edges. Therefore, the focus offsets of +0.20 mm produced a small ratio of the surface HAZ diameter to the irradiation diameter due to maybe the absence of the low intensity edges in the flat-top beam. However, the central-peak-intensity beam also exhibited a small ratio of the surface HAZ diameter to the irradiation diameter at the focus offset of +0.20. Because in the central-peak-intensity beam, the peak intensity at the focus offset

of +0.20 mm is smaller and the size of the beam was broader than that at the focus offset of 0.00 mm.

4.3.4 Summary

The drilling characteristics of a crown glass with a high CTE of $94 \times 10^{-7} /K$ and a low MP of $724^{\circ}C$ by a short-pulse CO_2 laser with a central-peak-intensity beam and a flat-top beam were investigated. The CO_2 laser produced a short laser pulse with a spike pulse width of 276 ns, a pulse tail length of 56.9 μs , an energy ratio of a spike pulse to a pulse tail of 1:20 and a laser beam of a central-peak-intensity beam or a flat-top beam at a repetition rate of 200 Hz. In the central-peak-intensity beam and the flat-top beam, a beam quality factor M^2 was 7.6 and 13.5, respectively. The laser beam was focused by a focusing lens with a focal length of 12.7 mm on the glass surface at the focus offsets of -0.20 mm to +0.20 mm. The central-peak-intensity beam produced conical holes at the focus offsets of -0.20 mm to -0.10 mm and produced biconical holes with a wide waist diameter at the focus offsets of 0.00 mm to +0.20 mm. The flat-top beam produced conical holes at the focus offsets of -0.20 mm to +0.10 mm and produced a cylindrical hole at the focus offset of +0.20 mm. The hole shape that is a conical hole, a biconical hole and a cylindrical hole formation depended on the beam profile and the focus offset. The hole depth depended on the focus offset and the total irradiation fluence. The ratio of the surface hole diameter to the irradiation diameter depended on the focus offset and did not depend on the fluence per single pulse and the total irradiation fluence. The ratio of the surface HAZ diameter to an irradiation diameter depended on the beam profile, the focus offset and the total irradiation fluence and did not depend on the fluence per single pulse. The ratio of the waist diameter to the surface hole diameter and the ratio of the waist depth to the hole depth depended on the focus offset and did not depend on the fluence per single pulse and the total irradiation fluence.

CHAPTER 5

Conclusion

CHAPTER 5

Conclusion

5.1 Conclusion

In this thesis, a crown glass with a high CTE of $94 \times 10^{-7} /K$ and a low MP of $724^{\circ}C$ was drilled by a short-pulse CO_2 laser with tunable laser parameters without an extra treatment that enabled a simple and cost-effective glass processing. Firstly, the objective was to find the required laser parameters to produce a crack-free hole and to investigate the dependence of the drilling characteristics on laser parameters. Secondly, the objective was to produce a cylindrical hole with an easy approach by using a flat-top beam rather than the complex set-up. Lastly, the objective was to investigate drilling characteristics in two types of laser beam that is a central-peak-intensity beam and a flat-top beam. By finding the CO_2 laser parameters that affect the drilling characteristics of a crown glass, this thesis aims to improve the quality, efficiency, and cost-effectiveness of CO_2 laser drilling of glass. Furthermore, this thesis seeks to pave the way to produce various hole shapes such as a conical hole, a cylindrical hole and a biconical hole that is a critical requirement in many industrial applications.

Firstly, the required short-pulse CO_2 laser parameters that produced crack-free holes in a crown glass without an extra treatment in the processing area and the influence of the short-pulse CO_2 laser parameters on drilling characteristics was investigated. The short-pulse CO_2 laser had a spike pulse with a pulse width of 250 ns, a pulse tail length of 31.4 μs to 135 μs , an energy ratio of a spike pulse to a pulse tail of 1:7.1 to 1:92. A number of pulses was 20 to 50, a fluence per single pulse was 6.01 J/cm^2 to 37.9 J/cm^2 , a total irradiation fluence was 238 J/cm^2 to 1305 J/cm^2 and a repetition rate was 1 Hz to 400 Hz. The laser beam was a doughnut-like beam with a beam quality factor M^2 of 3.4 to 7.9 at a repetition rate of 1 Hz to 50 Hz. The laser beam was a central-peak-intensity with large-shoulders beam with a beam quality factor M^2 of 3.1 to 6.7 at a repetition rate of 50 Hz to 400 Hz. The short laser pulses were irradiated by a focusing lens with a focal length of 38.1 mm at a focus offset of 0.00 mm. The Rayleigh length was 116 μm to 146 μm . The short laser pulses produced crack-free holes regardless of the energy of the pulse tail at a repetition rate of 150 Hz to 400 Hz. The short laser pulse irradiation realized a high drilling efficiency that is the

hole depth per the total irradiation fluence of $1.56 \mu\text{m}/\text{J}/\text{cm}^2$ in the laser pulse waveform with the energy ratio of a spike pulse to a pulse tail of 1:25, the fluence per single pulse of $11.9 \text{ J}/\text{cm}^2$, the total irradiation fluence of $937 \text{ J}/\text{cm}^2$ and the repetition rate of 200 Hz. In this experiment with the restrictive conditions, the drilling efficiency that is the hole depth per the total irradiation fluence depended on the laser pulse waveform, the fluence per single pulse and the repetition rate. The ratio of a surface hole diameter to an irradiation diameter did not influence by the laser pulse waveform and the fluence per single pulse, and the ratio was initially increased then almost same with the total irradiation fluence. Additionally, the ratio showed that the surface hole diameter was on average 47.7% smaller than the irradiation diameter. To produce a small surface hole diameter an investigation using a high-quality gaussian beam and a high NA could be useful. For example, a CO_2 laser with a wavelength of $10.6 \mu\text{m}$, a high-quality gaussian beam with a beam quality factor M^2 of 1.0, an f/D of 1.73 with a focal length f of 38.1 mm and a beam diameter D of 22.0 mm expected to give an irradiation diameter of $23.3 \mu\text{m}$, thus a hole diameter of $10.9 \mu\text{m}$ can be possible to produce by direct CO_2 laser irradiation. In this experiment with the above irradiation conditions and with the low total irradiation fluence, the laser pulse waveform and the fluence per single pulse did not influence the ratio of HAZ diameter to an irradiation diameter although the ratio was increased with the total irradiation fluence that is a natural phenomenon.

Secondly, a cylindrical hole was realized in a crown glass with a high CTE of $94 \times 10^{-7} /\text{K}$ and a low MP of 724°C using a short-pulse CO_2 laser with a flat-top beam profile. The CO_2 laser had a short laser pulse with a spike pulse width of 276 ns, a pulse tail length of $56.9 \mu\text{s}$, an energy ratio of a spike pulse to a pulse tail of 1:20 and a flat-top beam with a diameter of 12.5 mm and a beam quality factor M^2 of 13.5 at a repetition rate of 200 Hz. The flat-top beam was focused by the focusing lens with a focal length of 12.7 mm on the glass surface at the focus offsets of -0.20 mm to +0.40 mm. Cylindrical holes were produced in the glass at the focus offsets of +0.20 mm to +0.40 mm. The number of pulses were 30 to 90 and the total irradiation fluence was $110 \text{ J}/\text{cm}^2$ to $4209 \text{ J}/\text{cm}^2$. The Rayleigh length was $188 \mu\text{m}$. The cylindrical hole was produced by the recovered flat-top beam that was found after the Rayleigh length. In the cylindrical holes, the hole depth was $109 \mu\text{m}$ to $434 \mu\text{m}$, the surface hole diameter was $152 \mu\text{m}$ to $366 \mu\text{m}$, and the aspect ratio, defined as the ratio of the hole depth to the

surface hole diameter, was 0.30 to 2.89. The hole depth increased with the total irradiation fluence and became saturated. The saturation hole depth did not depend on the total irradiation fluence and the average saturated hole depth with the respective focus offset distance was 585 μm . To control the surface hole diameter and hole depth of a cylindrical hole, an investigation using a variable-NA system could be useful. The taper angle and the ratio of the surface hole diameter to the irradiation diameter depended on the focus offset and did not depend on the fluence per single pulse and the total irradiation fluence. The ratio of the surface HAZ diameter to the irradiation diameter depended on the focus offset and the total irradiation fluence and did not depend on the fluence per single pulse.

Lastly, a comparison of the drilling characteristics of a crown glass with a high CTE of $94 \times 10^{-7} /\text{K}$ and a low MP of 724°C by a short-pulse CO_2 laser with a central-peak-intensity beam and a flat-top beam were investigated. The CO_2 laser had a short laser pulse with a spike pulse width of 276 ns, a pulse tail length of 56.9 μs , an energy ratio of a spike pulse to a pulse tail of 1:20 and a laser beam of a central-peak-intensity beam or a flat-top beam at a repetition rate of 200 Hz. In the central-peak-intensity beam and the flat-top beam, a beam quality factor M^2 was 7.6 and 13.5, respectively. The laser beam was focused by a focusing lens with a focal length of 12.7 mm on the glass surface at the focus offsets of -0.20 mm to +0.20 mm. The number of pulses were 30 to 90 and the total irradiation fluence was 383 J/cm^2 to 4296 J/cm^2 . The Rayleigh length was 106 μm and 188 μm at the central-peak-intensity beam and the flat-top beam, respectively. The central-peak-intensity beam produced conical holes at the focus offsets of -0.20 mm to -0.10 mm and produced biconical holes with a wide waist diameter at the focus offsets of 0.00 mm to +0.20 mm. The biconical hole was produced due to the central-peak-intensity beam irradiation with a short focal length of the focusing lens. The laser beam intensity may be absorbed by the side walls in the hole resulting a wide waist and the hole bottom got narrow down as the beam propagated inside the hole. To control the size of the biconical hole a variable-NA system could be useful. The flat-top beam produced conical holes at the focus offsets of -0.20 mm to +0.10 mm and produced a cylindrical hole at a focus offset of +0.20 mm. The hole shape that is a conical hole, a cylindrical hole and a biconical hole depended on the beam profile and the focus offset. The hole depth depended on the focus offset and the total irradiation fluence. The ratio of the surface hole diameter to the irradiation

diameter depended on the focus offset and did not depend on the beam profile and the fluence per single pulse. The ratio of the surface HAZ diameter to the irradiation diameter depended on the beam profile, the focus offset and the total irradiation fluence and did not depend on the fluence per single pulse. The ratio of the waist diameter to the surface hole diameter and the ratio of the waist depth to the hole depth in the biconical hole depended on the focus offset and did not depend on the fluence per single pulse and the total irradiation fluence.

The summary of the findings is pointed out in the below Fig. 5.1-1. Crack-free various holes such as a conical hole, a biconical hole and a cylindrical hole drilling in a glass with a high CTE of $94 \times 10^{-7} /K$ and a low MP of $724^{\circ}C$ without an extra treatment was realized by a short-pulse CO_2 laser with tunable laser parameters. In these experiments, the hole shape that is the conical hole, the biconical hole and the cylindrical hole formation depended on the beam profile and the focus offset. The drilling efficiency was depended on the laser pulse waveform, the fluence per single pulse and the repetition rate.

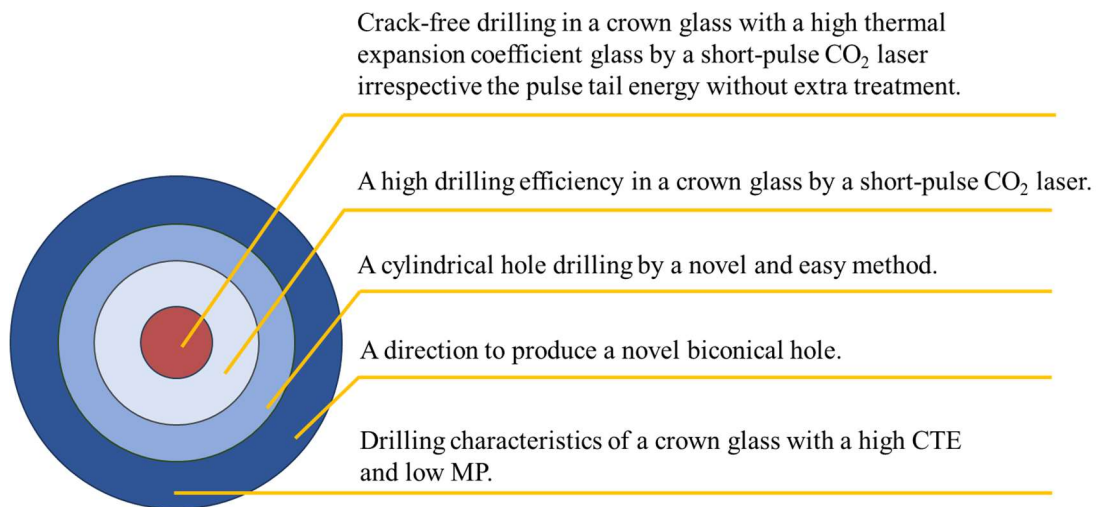


Fig. 5.1-1 Summary of the key findings.

In the next works, a small hole diameter close to $10 \mu m$ will be investigated by a short-pulse CO_2 laser with a high-quality gaussian beam with a beam quality factor M^2 of 1.0 and a high NA of about 0.80. To reduce HAZ, an investigation by a tail-free short pulse and a controlled laser beam profile is required. To improve the work speed, an investigation by a short-pulse CO_2 laser at a repetition rate of 1 kHz is required. The short-pulse CO_2 laser parameters such as a high fluence per single pulse and a high

total irradiation fluence will be considered. A CO₂ laser with an azimuthal and a radial beam polarization will also be considered to improve processing efficiency. Additionally, a glass with a CTE of $5.5 \times 10^{-7} /K$ to $94 \times 10^{-7} /K$ and an MP of 724°C to 1600°C and a thickness of 10 μm to 5000 μm will be considered. The investigation of cutting and grooving is also important. In the future, by measuring the temperature at various points at the sample surface, a predictive model can be developed that can lead to develop an AI (Artificial intelligence) tool for a sustainable and simple laser-based processing for industrial applications.

List of publications:

Journal articles:

1. M. E. Rahaman and K. Uno, "Crown glass drilling by short-Pulse CO₂ laser with tunable pulse tail," *Lasers Manuf. Mater. Process.*, 9, 72-80, (2022).
2. M. E. Rahaman and K. Uno, "Drilling of cylindrical holes in Crown glass by a short-pulse flat-top CO₂ laser beam," *Laser Phys.*, 33, 096004, (2023).

Conference Presentations:

1. M. E. Rahaman and K. Uno, "Drilling characteristics of glass with large thermal expansion coefficient by short-pulse CO₂ laser," SLPC2022 (The 4th Smart Laser Processing Conference), SLPC5-04, Pacifico Yokohama, Kanagawa, Japan, April 20 (2022).
2. M. E. Rahaman and K. Uno, "Crack-free crown-glass drilling by short-pulse CO₂ laser", COLA2021/2022 (16th International Conference on Laser Ablation), P-71-Tu, Kunibiki Messe, Matsue, Japan, April 26 (2022).

List of Abbreviations:

- AI** (Artificial intelligence)
- CW** (Continuous wave)
- CTE** (Thermal expansion coefficient)
- DOF** (Depth of focus)
- FHG** (Fourth harmonic generation)
- HAZ** (Heat affected zone)
- LCD** (Liquid crystal display)
- LG** (Laguerre-Gaussian)
- MP** (Melting point)
- MEMS** (Microelectromechanical systems)
- NA** (Numerical aperture)
- PDMS** (Polydimethylsiloxane)
- RF** (Radio frequency)
- SHG** (Second harmonic generation)
- TE** (Transversely excited)
- TEA** (Transversely excited atmospheric)
- TEM** (Transverse electromagnetic)
- TFT** (Thin film transistor)
- THG** (Third harmonic generation)
- UV** (Ultraviolet)

References

- [1] L. A. Hof and J. A. Ziki, "Micro-hole drilling on glass substrates-A review," *Micromachines*, 8, 1–23, (2017).
- [2] P. K. Gupta, "Non-crystalline solids: glasses and amorphous solids," *J. Non. Cryst. Solids*, 195, 158–164, (1996).
- [3] G. N. Greaves and S. Sen, "Inorganic glasses, glass-forming liquids and amorphizing solids," *Adv. Phys.*, 56, 1–166, (2007).
- [4] A. Maini, "Lasers and optoelectronics: fundamentals, devices and applications," Book, John Wiley & Sons., (2013).
- [5] H. K. Choi, M. S. Ahsan, D. Yoo, I. B. Sohn, Y. C. Noh, J. T. Kim, D. Jung, J. H. Kim, and H. M. Kang, "Formation of cylindrical micro-lens array on fused silica glass surface using CO₂ laser assisted reshaping technique," *Opt. Laser Technol.*, 75, 63–70, (2015).
- [6] H. Ogura and Y. Yoshida, "Hole drilling of glass substrates with a CO₂ laser," *Jpn. J. Appl. Phys.*, 42, 2881–2886, (2003).
- [7] M. Wakaki, Y. Komachi, G. Kanai, H. Fukumoto, and S. Kawabata, "Fabrication of microlenses and microlens arrays using local melting of glass plate by CO₂ laser," *Second Int. Symp. Laser Precis. Microfabr.*, 4426, 120, (2002).
- [8] D. Hunger, C. Deutsch, R. J. Barbour, R. J. Warburton, and J. Reichel, "Laser micro-fabrication of concave, low-roughness features in silica," *AIP Adv.*, 2, 012119, (2012).
- [9] R. Irawan, T. Swee Chuan, T. Chia Meng, and T. Khay Ming, "Rapid constructions of microstructures for optical fiber sensors using a commercial CO₂ Laser system," *Open Biomed. Eng. J.*, 2, 28–35, (2008).
- [10] M. Yang, Y. Li, and D. N. Wang, "Long-period fiber gratings fabricated by use of defocused CO₂ laser beam for polarization-dependent loss enhancement," *J. Opt. Soc. Am. B*, 26, 1203, (2009).
- [11] S. Oh, K. R. Lee, U.-C. Paek, and Y. Chung, "Fabrication of helical long-period

- fiber gratings by use of a CO₂ laser,” *Opt. Lett.*, 29, 1464, (2004).
- [12] M. Gu, X. Li, and Y. Cao, “Optical storage arrays: a perspective for future big data storage,” *Light Sci. Appl.*, 3, 177, (2014).
- [13] P. G. Kazansky, Y. Lei, L. Wang, Y. Yu, H. Wang, A. Corres, N. Spivack, and B. Sarao, “Eternal 5d data storage by ultrafast laser writing in glass,” *Proc. AIAA*, 9736, 97360U, (2020).
- [14] A. Schorderet, E. Deghilage, and K. Agbeviade, “Tool type and hole diameter influence in deep ultrasonic drilling of micro-holes in glass,” *Procedia CIRP*, 6, 565–570, (2013).
- [15] H. Nouraei, K. Kowsari, J. K. Spelt, and M. Papini, “Surface evolution models for abrasive slurry jet micro-machining of channels and holes in glass,” *Wear*, 309, 65–73, (2014).
- [16] C. Weingarten, E. Uluz, A. Schmickler, K. Braun, E. Willenborg, A. Temmler, and S. Heidrich, “Glass processing with pulsed CO₂ laser radiation,” *Appl. Opt.*, 56, 777, (2017).
- [17] K. Uno, T. Yamamoto, M. Watanabe, T. Akitsu, and T. Jitsuno, “SiO₂-glass drilling by short-pulse CO₂ laser with controllable pulse-tail energy,” *Proc. SPIE*, 9735, 973519, (2016).
- [18] A. Salleo, T. Sands, and F. Y. Génin, “Machining of transparent materials using an IR and UV nanosecond pulsed laser,” *Appl. Phys. A Mater. Sci. Process.*, 71, 601–608, (2000).
- [19] S. Mishra, N. Sridhara, A. Mitra, B. Yougandar, S. K. Dash, S. Agarwal, and A. Dey, “CO₂ laser cutting of ultra thin (75 μm) glass based rigid optical solar reflector (OSR) for spacecraft application,” *Opt. Lasers Eng.*, 90, 128–138, (2017).
- [20] P. Gečys, D. Juozas, and G. Račiukaitis, “Nanosecond laser processing of soda-lime glass,” *J. Laser Micro Nanoeng.*, 10, 254–258, (2015).
- [21] S. Mishra and V. Yadava, “Laser beam micro machining (LBMM)-A review,” *Opt. Lasers Eng.*, 73, 89–122, (2015).

- [22] C. Shi, M. L. Ermold, G. E. Oulundsen, and L. A. Newman, "CO₂ and CO laser comparison of glass and ceramic processing," *Proc. SPIE*, 10911, 109110M, (2019).
- [23] K. Okazaki, S. Torii, T. Makimura, H. Niino, K. Murakami, D. Nakamura, A. Takahashi, and T. Okada, "Sub-wavelength micromachining of silica glass by irradiation of CO₂ laser with Fresnel diffraction," *Appl. Phys. A Mater. Sci. Process.*, 104, 593–599, (2011).
- [24] A. K. Nath, T. Reghu, C. P. Paul, M. O. Ittoop, and P. Bhargava, "High-power transverse flow CW CO₂ laser for material processing applications," *Opt. Laser Technol.*, 37, 329–335, (2005).
- [25] K. Sakamoto, K. Uno, and T. Jitsuno, "Longitudinally excited CO₂ laser with a spike pulse width of 100 ns to 300 ns," *Proc. SPIE*, 10898, 108980U, (2019).
- [26] K. Uno and T. Jitsuno, "Control of laser pulse waveform in longitudinally excited CO₂ laser by adjustment of excitation circuit," *Opt. Laser Technol.*, 101, 195–201, (2018).
- [27] K. Uno and T. Jitsuno, "Control of laser pulse waveform in longitudinally excited CO₂ laser by adjustment of gas medium," *Proc. SPIE*, 10811, 108111, (2018).
- [28] K. Uno, J. Li, H. Goto, and T. Jitsuno, "Longitudinally excited CO₂ laser with short laser pulse and high quality beam," *Proc. SPIE*, 10518, 105181Y, (2018).
- [29] K. Uno, K. Dobashi, T. Akitsu, and T. Jitsuno, "Longitudinally excited CO₂ laser with tail-free short pulse," *Proc. SPIE*, 9266, 92661U, (2014).
- [30] K. Uno, K. Yanai, S. Watarai, Y. Kodama, K. Yoneya, and T. Jitsuno, "1 kHz Oscillation of short-pulse CO₂ laser pumped by longitudinal discharge without pre-ionization," *Opt. Laser Technol.*, 152, 108174, (2022).
- [31] C. Zhang, L. Zhang, X. Jiang, B. Jia, W. Liao, R. Dai, J. Chen, X. Yuan, and X. Jiang, "Influence of pulse length on heat affected zones of evaporatively-mitigated damages of fused silica optics by CO₂ laser," *Opt. Lasers Eng.*, 125, 105857, (2020).
- [32] F. Guignard, M. L. Autric, and V. Baudinaud, "Temperature and residual stress

- evolution in CO₂-laser-irradiated glass,” Proc. SPIE, 3343, 534–545, (1998).
- [33] L. Brusberg, M. Queisser, C. Gentsch, H. Schröder, and K. D. Lang, “Advances in CO₂-laser drilling of glass substrates,” Phys. Procedia, 39, 548–555, (2012).
- [34] C. K. Chung, S. L. Lin, H. Y. Wang, T. K. Tan, K. Z. Tu, and H. F. Lung, “Fabrication and simulation of glass micromachining using CO₂ laser processing with PDMS protection,” Appl. Phys. A Mater. Sci. Process., 113, 501–507, (2013).
- [35] C. K. Chung and S. L. Lin, “CO₂ laser micromachined crackless through holes of Pyrex 7740 glass,” Int. J. Mach. Tools Manuf., 50, 961–968, (2010).
- [36] R. Nakamura, T. Katsura, and T. Kojima, “Cutting complex shape in glass substrate with pulsed CO₂ laser,” Rev. Laser Eng., 43, 28–30, (2015).
- [37] I. B. W. and K. P. N. A. Wairimu G., “CO₂ laser machining of wood, perspex and glass with and without use of assist gas,” Int. J. Sci. Res. Innov. Technol., 2, 128–133, (2015).
- [38] P. E. Dyer, I. Waldeck, and G. C. Roberts, “Fine-hole drilling in Upilex polyimide and glass by TEA laser ablation,” J. Phys. D. Appl. Phys., 30, L19–L21, (1997).
- [39] D. Ashkenasi, T. Kaszemeikat, N. Mueller, R. Dietrich, H. J. Eichler, and G. Illing, “Laser trepanning for industrial applications,” Phys. Procedia, 12, 323–331, (2011).
- [40] H. M. Lee, J. H. Choi, and S. J. Moon, “Determining the machining parameters for femtosecond laser helical drilling of aluminosilicate glass substrate,” Int. J. Precis. Eng. Manuf., 18, 923–930, (2017).
- [41] S. Takahashi, K. Horiuchi, K. Tatsukoshi, M. Ono, N. Imajo, and T. Mobely, “Development of through glass via (TGV) formation technology using electrical discharging for 2.5/3D integrated packaging,” IEEE 63rd Electron. Components Technol. Conf., 348–352, (2013).
- [42] C. Iliescu, F. E. H. Tay, and J. Miao, “Strategies in deep wet etching of Pyrex glass,” Sens. Actuators A Phys., 133, 395–400, (2007).

- [43] K. Kolari, V. Saarela, and S. Franssila, "Deep plasma etching of glass for fluidic devices with different mask materials," *J. Micromech. Microeng.*, 18, 064010, (2008).
- [44] A. A. Tseng, Y. T. Chen, C. L. Chao, K. J. Ma, and T. P. Chen, "Recent developments on microablation of glass materials using excimer lasers," *Opt. Lasers Eng.*, 45, 975–992, (2007).
- [45] V. P. Veiko, G. K. Kostyuk, N. V. Nikonorov, A. N. Rachinskaya, E. B. Yakovlev, and D. V. Orlov, "Fast and reversible phase-structure modifications of glass-ceramic materials under CO₂-laser action," *Proc. SPIE*, 6606, 66060Q, (2007).
- [46] C. Iliescu, B. Chen, and J. Miao, "On the wet etching of Pyrex glass," *Sens. Actuators A Phys.*, 143, 154–161, (2008).
- [47] R. Wüthrich, "Micromachining using electrochemical discharge phenomenon," Book, Elsevier, (2015).
- [48] S.-T. Chen, Z.-H. Jiang, Y.-Y. Wu, and H.-Y. Yang, "Development of a grinding–drilling technique for holing optical grade glass," *Int. J. Mach. Tools Manuf.*, 51, 95–103, (2011).
- [49] A. K. Jain and P. M. Pandey, "Study of Peck drilling of borosilicate glass with μ RUM process for MEMS," *J. Manuf. Process.*, 22, 134–150, (2016).
- [50] A. Ghobeity, H. Getu, M. Papini, and J. K. Spelt, "Surface evolution models for abrasive jet micromachining of holes in glass and polymethylmethacrylate (PMMA)," *J. Micromech. Microeng.*, 17, 2175–2185, (2007).
- [51] K. Kowsari, H. Nouraei, D. F. James, J. K. Spelt, and M. Papini, "Abrasive slurry jet micro-machining of holes in brittle and ductile materials," *J. Mater. Process. Technol.*, 214, 1909–1920, (2014).
- [52] J. Chae, J. M. Giachino, and K. Najafi, "Fabrication and characterization of a wafer-level MEMS vacuum package with vertical feedthroughs," *J. Microelectromech. Syst.*, 17, 193–200, (2008).
- [53] V. S. Kondratenko, V. V. Kadomkin, L. Hung-Tu, A. S. Naumov, and I. E. Velikovskii, "Laser drilling of microholes in glass," *Glas. Ceram.*, 77, 39–42,

(2020).

- [54] C. A. McNally, J. Folkes, and I. R. Pashby, "Laser drilling of cooling holes in aeroengines: state of the art and future challenges," *Mater. Sci. Technol.*, 20, 805–813, (2004).
- [55] M. C. Gower, "Industrial applications of laser micromachining," *Opt. Express*, 7, 56, (2000).
- [56] M. R. Hossan and P. R. Konari, "Laser micromachining of glass substrates for microfluidics devices," *AIP Conf. Proc.*, 2324, 060002, (2021).
- [57] N. N. Rykalin, A. Uglov, and A. Kokora, "Laser machining and welding," Book, Pergamon press, (1978).
- [58] H. J. Booth, "Recent applications of pulsed lasers in advanced materials processing," *Thin Solid Films*, 453–454, 450–457, (2004).
- [59] K. Kolari, V. Saarela, and S. Franssila, "Deep plasma etching of glass for fluidic devices with different mask materials," *J. Micromech. Microeng.*, 18, 064010, (2008).
- [60] M. E. Rahaman and K. Uno, "Crown glass drilling by short-pulse CO₂ laser with tunable pulse tail," *Lasers Manuf. Mater. Process.*, 9, 72–80, (2022).
- [61] R. Kitamura, L. Pilon, and M. Jonasz, "Optical constants of silica glass from extreme ultraviolet to far infrared at near room temperature," *Appl. Opt.*, 46, 8118, (2007).
- [62] S. T. Yang, M. J. Matthews, S. Elhadj, D. Cooke, G. M. Guss, V. G. Draggoo, and P. J. Wegner, "Comparing the use of mid-infrared versus far-infrared lasers for mitigating damage growth on fused silica," *Appl. Opt.*, 49, 2606–2616, (2010).
- [63] L. J. Yang, Y. Wang, Z. G. Tian, and N. Cai, "YAG laser cutting soda-lime glass with controlled fracture and volumetric heat absorption," *Int. J. Mach. Tools Manuf.*, 50, 849–859, (2010).
- [64] C. Huaiyu, L. Lei, Z. Dongdi, A. Bo, B. Yunsong, F. Zhigang, and Z. Yongpeng, "Study of photo-ionization and thermal effects on the interaction of a

- nanosecond extreme ultraviolet laser with copper,” *Opt. Express*, 30, 5817, (2022).
- [65] K. Arai, H. Imai, H. Hosono, Y. Abe, and H. Imagawa, “Two-photon processes in defect formation by excimer lasers in synthetic silica glass,” *Appl. Phys. Lett.*, 53, 1891–1893, (1988).
- [66] J. Li, P. R. Herman, X. M. Wei, K. P. Chen, J. Ihlemann, G. Marowsky, P. Oesterlin, and B. Burghardt, “High-resolution F₂ -laser machining of micro-optic components,” *Phot. Process. Microelectron. Photonics*, 4637, 228, (2002).
- [67] S. H. Cho, W. S. Chang, J. G. Kim, K. R. Kim, and J. W. Hong, “Fabrication of internal diffraction gratings in planar fluoride glass using low-density plasma formation induced by a femtosecond laser,” *Appl. Surf. Sci.*, 255, 2069–2074, (2008).
- [68] S. Ahn, J. Choi, J. Noh, and S. H. Cho, “High aspect ratio nanoholes in glass generated by femtosecond laser pulses with picosecond intervals,” *Opt. Lasers Eng.*, 101, 85–88, (2018).
- [69] M. Kumar, A. K. Biswas, T. Biswas, J. Joshi, L. B. Rana, R. K. Yadav, and R. Kaul, “Maximizing the efficiency of a compact helium-free TEA CO₂ laser: Experimental results and theoretical simulation,” *Opt. Laser Technol.*, 120, 105764, (2019).
- [70] M. Kumar, T. Reghu, A. K. Biswas, P. Bhargav, J. S. Pakhare, S. Kumar, A. Verma, V. Mandloi, and L. M. Kukreja, “Development of a 1 J short pulse tunable TEA CO₂ laser with high energy stability,” *Opt. Laser Technol.*, 64, 64–71, (2014).
- [71] W. Witteman, “The CO₂ laser,” Book, Springer, (2013).
- [72] R. Delmdahl and R. Paetzel, “Laser drilling of high-density through glass vias (TGVs) for 2.5D and 3D packaging,” *J. Microelectron. Packag. Soc.*, 21, 53–57, (2014).
- [73] Y. Matsuoka, K. Wake, T. Nagashima, and N. Iehisa, “Glass processing using the fourth harmonic of nanosecond pulse Nd:YAG laser,” *Appl. Phys. A Mater. Sci. Process.*, 87, 81–85, (2007).

- [74] S. Sato, H. Hidai, S. Matsusaka, A. Chiba, and N. Morita, "Drilling, bonding, and forming conductive path in the hole by laser percussion drilling," *Precis. Eng.*, 61, 147–151, (2020).
- [75] S. Nikumb, Q. Chen, C. Li, H. Reshef, H. Y. Zheng, H. Qiu, and D. Low, "Precision glass machining, drilling and profile cutting by short pulse lasers," *Thin Solid Films*, 477, 216–221, (2005).
- [76] H. Niino, Y. Kawaguchi, T. Sato, A. Narazaki, X. Ding, and R. Kurosaki, "Surface microfabrication of fused silica glass by UV laser irradiation," *Proc. SPIE*, 5339, 112–117, (2004).
- [77] D. Ashkenasi, T. Kaszemeikat, N. Mueller, A. Lemke, and H. J. Eichler, "Machining of glass and quartz using nanosecond and picosecond laser pulses," *Proc. SPIE*, 8243, 82430M, (2012).
- [78] D. Tokunaga, S. Sato, H. Hidai, S. Matsusaka, A. Chiba, and N. Morita, "A novel method of triggering fiber fuse inside glass by optical breakdown and glass drilling as its application," *Appl. Phys. A Mater. Sci. Process.*, 125, 1–9, (2019).
- [79] Y. Wu, W. Jia, C. Y. Wang, M. Hu, X. Ni, and L. Chai, "Micro-hole fabricated inside FOTURAN glass using femtosecond laser writing and chemical etching," *Opt. Quantum Electron.*, 39, 1223–1229, (2007).
- [80] H. Huang, L.-M. Yang, and J. Liu, "Micro-hole drilling and cutting using femtosecond fiber laser," *Opt. Eng.*, 53, 051513, (2014).
- [81] H. M. Lee, J. H. Choi, and S. J. Moon, "Machining characteristics of glass substrates containing chemical components in femtosecond laser helical drilling," *Int. J. Precis. Eng. Manuf. - Green Technol.*, 8, 375–385, (2021).
- [82] K. Yoshiki, "High-aspect ratio laser drilling of glass assisted by supercritical carbon dioxide," *Proc. SPIE*, 10092, 100921K, (2017).
- [83] S. Heidrich, C. Weingarten, E. Uluz, and R. Poprawe, "Glass processing with high power Q-Switch CO₂ laser radiation," *Proc. LIM*, 1, 1–7, (2015).
- [84] K. L. Wlodarczyk, W. N. Macpherson, and D. P. Hand, "Laser processing of Borofloat® 33 glass," *Proc. LAMP*, 1, 1–5, (2015).

- [85] D. Teixidor, I. Ferrer, L. Criales, and T. Özel, “Laser machining,” Book chapt., in *Modern manufacturing processes*, John Wiley & So, (2019).
- [86] J. Dutta Majumdar and I. Manna, “Laser processing of materials,” *Sadhana*, 28, 495–562, (2003).
- [87] B. S. Yilbas, “Conduction-limited laser pulsed laser heating: Fourier heating model,” Book chapt., in *Laser heating applications*, Elsevier, (2012).
- [88] M. von Allmen and A. Blatter, “Laser-beam interaction with materials,” Book, Springer, (1995).
- [89] M. Bass, “Laser materials interactions,” Book chapt., in *Laser fabrication and machining of materials*, Springer, (2008).
- [90] Z. H. Shen, S. Y. Zhang, J. Lu, and X. W. Ni, “Mathematical modeling of laser induced heating and melting in solids,” *Opt. Laser Technol.*, 33, 533–537, (2001).
- [91] B. S. Yilbas, M. Sami, A. Z. Sahin, A. Z. Al-Garni, and A. Qoban, “Heat transfer mechanisms in relation to laser surface melting of nitrated steel,” *WIT Trans. Eng. Sci.*, 5, 589–598, (1998).
- [92] X. Luo, W. Yang, T. Tan, D. Zhu, J. Zhuo, M. Liu, Q. Zhang, and Y. Li, “Numerical simulation of micro-flow surface smoothing of fused silica by CO₂ Laser,” *J. Laser Micro Nanoeng.*, 16, 121–129, (2021).
- [93] M. Darif, N. Semmar, and F. O. Cedex, “Numerical simulation of Si nanosecond laser annealing by COMSOL multiphysics,” *Proc. COMSOL*, 2, 1–7, (2008).
- [94] L. Zhao, J. Cheng, M. Chen, X. Yuan, W. Liao, H. Wang, Q. Liu, and H. Yang, “Toward little heat-affected area of fused silica materials using short pulse and high power CO₂ laser,” *Results Phys.*, 12, 1363–1371, (2019).
- [95] M. M. Kashani, M. R. Movahhedy, M. T. Ahmadian, and R. S. Razavi, “Analytical prediction of the temperature field in laser assisted machining,” *Procedia CIRP*, 46, 575–578, (2016).
- [96] K. A. Elijah, “Principles of laser materials processing: developments and applications,” Book, Johan Wiley & Sons, (2009).

- [97] S. Williams M and J. Mazumder, "Laser material processing," Book, Springer, (2008).
- [98] A. E. Hussein, P. K. Diwakar, S. S. Harilal, and A. Hassanein, "The role of laser wavelength on plasma generation and expansion of ablation plumes in air," *J. Appl. Phys.*, 113, 143305, (2013).
- [99] A. K. Nath, "Laser drilling of metallic and nonmetallic substrates," Book chapt., in *Comprehensive materials processing*, Elsevier, (2014).
- [100] P. P. Pronko, S. K. Dutta, D. Du, and R. K. Singh, "Thermophysical effects in laser processing of materials with picosecond and femtosecond pulses," *J. Appl. Phys.*, 78, 6233–6240, (1995).
- [101] Y. Ma, C. Xin, W. Zhang, and G. Jin, "Experimental study of plasma plume analysis of long pulse laser irradiates CFRP and GFRP composite materials," *Crystals*, 11, 545, (2021).
- [102] L. F. Wu and M. J. Tsai, "Effect of laser plasma on Nd:YAG laser drilling of acrylic plate with high optical density," *Opt. Laser Technol.*, 149, 107827, (2022).
- [103] K. Uno, "Longitudinally excited CO₂ laser," Book Chapt., in *Laser pulses-theory, technology, and applications*, InTech, (2012).
- [104] N. Hurst and S. S. Harilal, "Pulse shaping of transversely excited atmospheric CO₂ laser using a simple plasma shutter," *Rev. Sci. Instrum.*, 80, 10–14, (2009).
- [105] H. Michel Kon Yew, "Injection-switched high-pressure sub-10-picosecond Carbon dioxide laser amplifier," Ph.D. Thesis, University of British Columbia (2002).
- [106] A. J. Alcock, P. B. Corkum, and D. J. James, "A fast scalable switching technique for high-power CO₂ laser radiation," *Appl. Phys. Lett.*, 27, 680–682, (1975).
- [107] A. I. Karapuzikov, A. N. Malov, and I. V. Sherstov, "Tunable TEA CO₂ laser for long-range DIAL lidar," *Infrared Phys. Technol.*, 41, 77–85, (2000).
- [108] F. Geist, M. Guyenot, W. Herbst, H. Pascher, R. Verkerk, and W. Prettl, "Q-

- switched CO₂ laser with pulsed longitudinal discharge for nonlinear optical applications,” *Rev. Sci. Instrum.*, 68, 3599–3600, (1997).
- [109] S. J. Park and W. Y. Kim, “AC-chopper application for CW CO₂ laser,” *Opt. Laser Technol.*, 42, 269–273, (2010).
- [110] J. Choi, “Frequency stabilization of a radio frequency excited CO₂ laser using the photoacoustic effect,” *Rev. Sci. Instrum.*, 81, 064901, (2010).
- [111] H.-J. Chung, D.-H. Lee, J.-H. Hong, J.-H. Joung, Y.-M. Sung, S.-J. Park, and H.-J. Kim, “A simple pulsed CO₂ laser with long milliseconds pulse duration,” *Rev. Sci. Instrum.*, 73, 484–485, (2002).
- [112] Y. S. Lee, H. J. Chung, J. H. Joung, E. J. Kim, and H. J. Kim, “Active long pulse shaping technique of pulsed CO₂ laser using multi-pulse discharge control,” *Opt. Laser Technol.*, 36, 57–61, (2004).
- [113] J. Wu, Z. Zhang, D. Wang, S. Liu, Y. Tang, R. Tan, K. Zhang, and C. Wan, “Novel long-pulse TE CO₂ laser excited by pulser–sustainer discharge,” *Opt. Laser Technol.*, 39, 701–704, (2007).
- [114] V. Nasrollahi, P. Penchev, A. Batal, H. Le, S. Dimov, and K. Kim, “Laser drilling with a top-hat beam of micro-scale high aspect ratio holes in silicon nitride,” *J. Mater. Process. Technol.*, 281, 116636, (2020).
- [115] K. Kanzler, “Transformation of a gaussian laser beam to an Airy pattern for use in focal plane intensity shaping using diffractive optics,” *Proc. SPIE*, 4443, 58–65, (2001).
- [116] S. Saghafi, C. J. R. Sheppard, and J. A. Piper, “Characterising elegant and standard Hermite-Gaussian beam modes,” *Opt. Commun.*, 191, 173–179, (2001).
- [117] M. Endo, N. Araya, Y. Kurokawa, and K. Uno, “Anomalous enhancement of drilling rate in carbon fiber reinforced plastic using azimuthally polarized CO₂ laser,” *Laser Phys.*, 26, 96001, (2016).
- [118] A. Laskin and V. Laskin, “Refractive field mapping beam shaping optics: Important features for a right choice,” *Proc. LIA*, 103, 1181–1189, (2010).
- [119] H. J. Eichler, E. Jürgen, and O. Lux, “Lasers. Basic, Advances and

Applications,” Book, Springer, (2018).

- [120] B. N. Masina, B. Mwakikunga, and A. Forbes, “Thermally induced damage studies with shaped light,” *Opt. Eng.*, 52, 044301, (2013).
- [121] D. W. Coutts, M. J. Withford, J. A. Piper, G. Rutterford, A. I. Bell, and M. R. H. Knowles, “Generation of flat-top focussed beams for percussion drilling of ceramic and metal,” *Proc. LIA*, 160514, 160514, (2002).
- [122] B. Mercier, J. P. Rousseau, A. Jullien, and L. Antonucci, “Nonlinear beam shaper for femtosecond laser pulses, from Gaussian to flat-top profile,” *Opt. Commun.*, 283, 2900–2907, (2010).
- [123] H. Norman and W. Horst, “Laser resonators and beam propagation,” Book, Springer, (2009).
- [124] R. Weber, A. Michalowski, M. Abdou-Ahmed, V. Onuseit, V. Rominger, M. Kraus, and T. Graf, “Effects of radial and tangential polarization in laser material processing,” *Phys. Procedia*, 12, 21–30, (2011).
- [125] M. A. Ahmed, J. Schulz, A. Voss, O. Parriaux, J.-C. Pommier, and T. Graf, “Radially polarized 3kW beam from a CO₂ laser with an intracavity resonant grating mirror,” *Opt. Lett.*, 32, 1824, (2007).
- [126] R. Torres, T. Kaempfe, M. Delaigue, O. Parriaux, C. Hönninger, J. Lopez, R. Kling, and E. Mottay, “Influence of laser beam polarization on laser micro-machining of molybdenum,” *J. Laser Micro Nanoeng.*, 8, 188–191, (2013).
- [127] V. G. Niziev and A. V. Nesterov, “Influence of beam polarization on laser cutting efficiency,” *J. Phys. D. Appl. Phys.*, 32, 1455–1461, (1999).
- [128] C. Tan, L. Zhao, M. Chen, J. Cheng, H. Yang, Q. Liu, Z. Yin, and W. Ding, “Morphology evolution mechanisms and localized structural modification of repaired sites on fused silica optics processed by CO₂ laser rapid ablation mitigation,” *Opt. Laser Technol.*, 147, 107648, (2022).
- [129] N. Bouras, M. A. Madjoubi, M. Kolli, S. Benterki, and M. Hamidouche, “Thermal and mechanical characterization of borosilicate glass,” *Phys. Procedia*, 2, 1135–1140, (2009).

- [130] C.-H. Tsai and C.-C. Li, “Investigation of underwater laser drilling for brittle substrates,” *J. Mater. Process. Technol.*, 209, 2838–2846, (2009).
- [131] Schott AG, “B 270 ® i Ultra-White Glass,” <https://www.schott.com/en-sg/products/b-270-p1000313>, (accessed Jun. 13, 2022).
- [132] C. K. Chung, H. C. Chang, T. R. Shih, S. L. Lin, E. J. Hsiao, Y. S. Chen, E. C. Chang, C. C. Chen, and C. C. Lin, “Water-assisted CO₂ laser ablated glass and modified thermal bonding for capillary-driven bio-fluidic application,” *Biomed. Microdevices*, 12, 107–114, (2010).
- [133] C. K. Chung, Y. C. Sung, G. R. Huang, E. J. Hsiao, W. H. Lin, and S. L. Lin, “Crackless linear through-wafer etching of Pyrex glass using liquid-assisted CO₂ laser processing,” *Appl. Phys. A Mater. Sci. Process.*, 94, 927–932, (2009).
- [134] L. Brusberg, M. Queisser, M. Neitz, H. Schröder, and K. Lang, “CO₂-laser drilling of TGVs for glass interposer applications,” *IEEE 64th Electron. Components Technol. Conf.*, 1759–1764, (2014).
- [135] A. A. Abramov and A. A. Becker, “Laser forming of holes in brittle materials assisted by stress reduction through heating,” *Procedia CIRP*, 94, 511–514, (2020).
- [136] G. A. J. Markillie, H. J. Baker, F. J. Villarreal, and D. R. Hall, “Effect of vaporization and melt ejection on laser machining of silica glass micro-optical components,” *Appl. Opt.*, 41, 5660, (2002).
- [137] B. K. Nayak, R. Akarapu, J. P. Carberry, and A. Liu, “Experimental and theoretical investigation of CO₂ laser drilling of fused silica,” *J. Laser Micro Nanoeng.*, 9, 79–82, (2014).
- [138] Y. Baba and K. Uno, “Borosilicate glass drilling by longitudinally excited CO₂ laser,” *Proc. SPIE*, 11546, 115460O, (2020).
- [139] J. Bliedtner, O. Faehnle, A.-M. Layher, R. Hassel, and A. Barz, “Pre-heating by defocusation of the CO₂-Laser polishing beam: an experimental report from the lab-floor,” *EPJ Web Conf.*, 255, 03001, (2021).
- [140] L. Matsunami Glass Ind., “Matsunami slide glass.” https://www.matsunami-glass.co.jp/product/glass/glass_slide/ (accessed Jun. 13, 2022).

- [141] K. Uno, S. Watarai, Y. Kodama, K. Yoneya, and T. Jitsuno, "Longitudinally excited short-pulse CO₂ laser with large discharge tube without preionization," *Opt. Laser Technol.*, 148, 107745, (2022).
- [142] Y. Baba, "Study of various glass processing by short-pulse CO₂ laser," Masters Thesis, University of Yamanashi, (2022).